

ANL-7640

RETURN TO ANL (IDAHO) LIBRARY.

# Argonne National Laboratory

## REACTOR DEVELOPMENT PROGRAM PROGRESS REPORT

November 1969

PROPERTY OF  
ARGONNE NATIONAL LAB  
IDAHO LIBRARY

The facilities of Argonne National Laboratory are owned by the United States Government. Under the terms of a contract (W-31-109-Eng-38) between the U. S. Atomic Energy Commission, Argonne Universities Association and The University of Chicago, the University employs the staff and operates the Laboratory in accordance with policies and programs formulated, approved and reviewed by the Association.

#### MEMBERS OF ARGONNE UNIVERSITIES ASSOCIATION

The University of Arizona	Kansas State University	The Ohio State University
Carnegie-Mellon University	The University of Kansas	Ohio University
Case Western Reserve University	Loyola University	The Pennsylvania State University
The University of Chicago	Marquette University	Purdue University
University of Cincinnati	Michigan State University	Saint Louis University
Illinois Institute of Technology	The University of Michigan	Southern Illinois University
University of Illinois	University of Minnesota	University of Texas
Indiana University	University of Missouri	Washington University
Iowa State University	Northwestern University	Wayne State University
The University of Iowa	University of Notre Dame	The University of Wisconsin

#### LEGAL NOTICE

This report was prepared as an account of Government sponsored work. Neither the United States, nor the Commission, nor any person acting on behalf of the Commission:

A. Makes any warranty or representation, expressed or implied, with respect to the accuracy, completeness, or usefulness of the information contained in this report, or that the use of any information, apparatus, method, or process disclosed in this report may not infringe privately owned rights; or

B. Assumes any liabilities with respect to the use of, or for damages resulting from the use of any information, apparatus, method, or process disclosed in this report.

As used in the above, "person acting on behalf of the Commission" includes any employee or contractor of the Commission, or employee of such contractor, to the extent that such employee or contractor of the Commission, or employee of such contractor prepares, disseminates, or provides access to, any information pursuant to his employment or contract with the Commission, or his employment with such contractor.

Printed in the United States of America

Available from

Clearinghouse for Federal Scientific and Technical Information  
National Bureau of Standards, U. S. Department of Commerce  
Springfield, Virginia 22151

Price: Printed Copy \$3.00; Microfiche \$0.65



ARGONNE NATIONAL LABORATORY  
9700 South Cass Avenue  
Argonne, Illinois 60439

REACTOR DEVELOPMENT PROGRAM  
PROGRESS REPORT

November 1969

Robert B. Duffield, Laboratory Director  
Stephen Lawroski, Associate Laboratory Director

Division

Director

Chemical Engineering  
EBR-II Project  
Metallurgy  
Reactor Engineering  
Reactor Physics

R. C. Vogel  
M. Levenson  
M. V. Nevitt  
L. J. Koch  
R. Avery

Report coordinated by  
A. Glassner and A. D. Rossin

Issued December 31, 1969

## FOREWORD

The Reactor Development Program Progress Report, issued monthly, is intended to be a means of reporting those items of significant technical progress which have occurred in both the specific reactor projects and the general engineering research and development programs. The report is organized in accordance with budget activities in a way which, it is hoped, gives the clearest, most logical overall view of progress. Since the intent is to report only items of significant progress, not all activities are reported each month. In order to issue this report as soon as possible after the end of the month editorial work must necessarily be limited. Also, since this is an informal progress report, the results and data presented should be understood to be preliminary and subject to change unless otherwise stated.

The issuance of these reports is not intended to constitute publication in any sense of the word. Final results either will be submitted for publication in regular professional journals or will be published in the form of ANL topical reports.

The last six reports issued  
in this series are:

April-May 1969	ANL-7577
June 1969	ANL-7581
July 1969	ANL-7595
August 1969	ANL-7606
September 1969	ANL-7618
October 1969	ANL-7632

## REACTOR DEVELOPMENT PROGRAM

### Highlights of Project Activities for November 1969

#### EBR-II

The test-1 instrumented subassembly was installed in the reactor, given a successful operational checkout, and then removed from the core. The instrument leads were cut cleanly by the lead-cutting tool; the subassembly separated smoothly from its extension tube. The test-2 (fueled) instrumented subassembly is in the primary tank being made ready for installation in the core.

Personnel entered the air cell of the Fuel Cycle Facility for the first time since the cell began closed operation in 1965. Direct maintenance is being performed on equipment that could not be serviced remotely during the more than four years of closed operation. Concurrently, electrical, instrument, and pneumatic services are being installed for new in-cell examination equipment.

The 18 unique xenon tags on hand are estimated to be sufficient for EBR-II xenon-tagging needs through mid-1970. Efforts are made to ensure a sufficient number of the tags for future needs. Two new series of xenon tags are being developed and techniques for injecting and measuring the tags are being refined.

#### ZPR-3

Assembly 58, a simple, benchmark, plutonium-carbon system, has a critical mass of 101.63 kg Pu-239 and 0.28 kg Pu-241. The depleted-uranium reflected core was assembled unsymmetrically about the reactor midplane to accommodate a subsequent lead-reflected core. Effective source strength, rod worth, and central neutron spectrum have been measured.

#### ZPR-6

The loading of Assembly 6A, the 4000-liter  $^{235}\text{U}$  core has been completed. The determination of the critical mass of the uniform core is under way. Rod worth, fuel worth, and central neutron spectra in voided and unvoided regions have been measured.

#### ZPR-9

In preparation for the FTR-3 plutonium-core loading, the matrix tubes and drawers were decontaminated and checked for horizontal and vertical alignment at experimental locations. Inner and outer core regions and the reflector have been preloaded with all materials except fuel plates.

## ZPPR

Computational methods were checked by comparison with worth data obtained during the stepwise removal of the boron control ring and the simultaneous depletion of the central zone in FTR-2; quite satisfactory agreement was obtained. The core was further characterized by radial reaction-rate traverses, activation profiles, and central fission ratios. Before the experiments on the FTR-2 assembly were concluded, measurements of fast-neutron spectra were made by a proton-recoil technique in the reflector and shield.

# TABLE OF CONTENTS

	<u>Page</u>
I. LIQUID METAL FAST BREEDER REACTORS--CIVILIAN	1
A. Physics Development--LMFBR	1
1. Theoretical Reactor Physics	1
2. Experimental Reactor Physics	10
3. ZPR-6 and -9 Operations and Analysis	20
4. ZPR-3 and ZPPR Operations and Analysis	21
B. Component Development--LMFBR	25
1. Instrumentation and Control	25
2. Fuel Handling, Vessels and Internals	32
C. Sodium Technology	33
1. Sodium Chemistry	33
2. Purification of Sodium	34
3. On-Line Monitors	35
4. Sampling	36
5. Fission Product Behavior and Control	36
6. Materials Compatibility	37
D. EBR-II--Research and Development	39
1. Equipment--Fuel Related	39
2. Instrumented Subassemblies	39
3. Coolant Chemistry	40
4. Experimental Irradiation and Testing	44
5. Materials-Coolant Compatibility	46
6. Systems Engineering	51
7. Leak Detection and Location--Xenon Method	53
8. Reactor Analysis, Testing and Methods Development	58
9. Driver Fuel Development	68
10. Operation with Failed Fuel	73
11. Physics Mock-up Studies	76
E. EBR-II--Operations	78
1. Reactor Plant	78
2. Fuel Cycle Facility	78
PUBLICATIONS	85

## TABLE OF CONTENTS

	<u>Page</u>
II. OTHER FAST REACTORS--OTHER FAST BREEDER REACTORS--FUEL DEVELOPMENT	87
A. Irradiation Effects, Mechanical Properties and Fabrication	87
1. Mechanical Properties of Type 316 Austenitic Stainless Steels	87
III. GENERAL REACTOR TECHNOLOGY	88
A. Applied and Reactor Physics Development	88
1. Theoretical Reactor Physics--Research and Development	88
2. Nuclear Data--Research and Development	91
B. Reactor Fuels and Materials Development	94
1. Fuels and Claddings--Research and Development	94
2. Techniques of Fabrication and Testing--Research and Development	111
3. Engineering Properties of Reactor Materials--Research and Development	112
C. Engineering Development--Research and Development	116
1. Instrumentation and Control	116
2. Heat Transfer and Fluid Flow	118
3. Engineering Mechanics	120
D. Chemistry and Chemical Separations	123
1. Fuel Cycle Technology--Research and Development	123
2. General Chemistry and Chemical Engineering--Research and Development	124
PUBLICATIONS	127
IV. NUCLEAR SAFETY RESEARCH AND DEVELOPMENT	128
A. LMFBR Safety--Research and Development	128
1. Reactor Control and Stability	128
2. Coolant Dynamics	129

## TABLE OF CONTENTS

	<u>Page</u>
3. Fuel Meltdown Studies with TREAT	130
4. Violent Boiling	136
5. Post-accident Heat Removal	137
B. Engineered Safety Features--Safety Features Technology-- Research and Development--Containment	138
1. Hydrodynamic Response to High-Energy Excursion	138
PUBLICATIONS	141



# TABLE OF CONTENTS

1. Introduction	1
2. Theoretical Framework	10
3. Methodology	25
4. Results	45
5. Discussion	65
6. Conclusion	85
7. References	95
8. Appendix	105
9. Index	115
10. Glossary	125
11. Bibliography	135
12. List of Figures	145
13. List of Tables	155
14. Acknowledgments	165
15. Author's Note	175
16. Contact Information	185
17. Declaration of Interest	195
18. Funding Sources	205
19. Data Availability	215
20. Ethics Statement	225
21. Conflicts of Interest	235
22. Contributions	245
23. Correspondence	255
24. Supplementary Materials	265
25. Additional Resources	275
26. Further Reading	285
27. Related Works	295
28. Future Research	305
29. Limitations	315
30. Strengths	325
31. Implications	335
32. Policy Recommendations	345
33. Practical Applications	355
34. Theoretical Contributions	365
35. Methodological Contributions	375
36. Empirical Contributions	385
37. Conceptual Contributions	395
38. Analytical Contributions	405
39. Interpretive Contributions	415
40. Critical Contributions	425
41. Constructive Contributions	435
42. Transformative Contributions	445
43. Generative Contributions	455
44. Regenerative Contributions	465
45. Restorative Contributions	475
46. Reintegrative Contributions	485
47. Reconstructive Contributions	495
48. Reconfigurative Contributions	505
49. Reorganizational Contributions	515
50. Reconceptual Contributions	525
51. Reinterpretive Contributions	535
52. Reevaluative Contributions	545
53. Reexaminative Contributions	555
54. Reinvestigative Contributions	565
55. Reiterative Contributions	575
56. Reconfirming Contributions	585
57. Reaffirming Contributions	595
58. Revalidating Contributions	605
59. Reestablishing Contributions	615
60. Reinstating Contributions	625
61. Reintegrating Contributions	635
62. Reconstructing Contributions	645
63. Reconfiguring Contributions	655
64. Reorganizing Contributions	665
65. Reconceptualizing Contributions	675
66. Reinterpreting Contributions	685
67. Reevaluating Contributions	695
68. Reexamining Contributions	705
69. Reinvestigating Contributions	715
70. Reiterating Contributions	725
71. Reconfirming Contributions	735
72. Reaffirming Contributions	745
73. Revalidating Contributions	755
74. Reestablishing Contributions	765
75. Reinstating Contributions	775
76. Reintegrating Contributions	785
77. Reconstructing Contributions	795
78. Reconfiguring Contributions	805
79. Reorganizing Contributions	815
80. Reconceptualizing Contributions	825
81. Reinterpreting Contributions	835
82. Reevaluating Contributions	845
83. Reexamining Contributions	855
84. Reinvestigating Contributions	865
85. Reiterating Contributions	875
86. Reconfirming Contributions	885
87. Reaffirming Contributions	895
88. Revalidating Contributions	905
89. Reestablishing Contributions	915
90. Reinstating Contributions	925
91. Reintegrating Contributions	935
92. Reconstructing Contributions	945
93. Reconfiguring Contributions	955
94. Reorganizing Contributions	965
95. Reconceptualizing Contributions	975
96. Reinterpreting Contributions	985
97. Reevaluating Contributions	995
98. Reexamining Contributions	1005
99. Reinvestigating Contributions	1015
100. Reiterating Contributions	1025

# I. LIQUID METAL FAST BREEDER REACTORS--CIVILIAN

## A. Physics Development--LMFBR

### 1. Theoretical Reactor Physics

#### a. General Reactor Physics

##### (i) Resonance and Doppler Theory (R. N. Hwang)

Last Reported: ANL-7553, pp. 6-7 (Feb 1969).

It is known that the fission widths deduced from values of  $\alpha$  in the keV region do not agree with those deduced from a single-level analysis of the resolved resonances. The mean fission widths ( $\bar{\Gamma}_f$ ) of the resolved resonances are compared in Table I.A.1 with the mean values, which were recently obtained from  $\alpha$ -values in the keV region with the assumption of channel theory.\* Disagreements are very prominent for U-233 and U-235. The following three causes are considered to explain these disagreements.

- 1)  $\bar{\Gamma}_f$  may have an intermediate fluctuation due to the existence of the second minimum point in the fission potential\*\* (double-humped potential).
- 2) As the mean value is deduced from relatively few resonances in the resolved region, the statistical deviation due to the small sampling may cause these disagreements.
- 3) The resolved resonances may not be real resonances but quasi-resonances,<sup>†</sup> as the ratio of  $\Gamma/D$  is large for the fissile nuclides. In this case two wide resonances are observed as a single narrow resonance.

First, the intermediate structure of  $\bar{\Gamma}_f$  is prominent for a subthreshold channel. Hence this effect must be very small for U-233, U-235, and Pu-241, as these nuclides have at least one fully open channel for each spin state from the assumption of channel theory.\* On the other hand, the  $1^+$  state of Pu-239 has only a slightly open channel and the intermediate structure of  $\bar{\Gamma}_f$  is very important. The giant resonance-like behavior of  $\alpha$  and  $\sigma_f$  can be explained with this intermediate structure of  $\bar{\Gamma}_f$ . This problem of  $\bar{\Gamma}_f$  for Pu-239 is very interesting and very complicated. Here U-233, U-235, and Pu-241 will be considered.

\* Kikuchi, Y., and An, S., submitted to J. Nucl. Sci. Tech.

\*\* Lynn, J. E., AERE-R-5891 (1968).

<sup>†</sup> Lynn, J. E., The Theory of Neutron Resonance Reactions, Clarendon Press, Oxford (1968).

TABLE I.A.1. Comparison of the Average Fission Widths  
Deduced from Average Values of  $\alpha$  and  
from the Resolved Resonances

Nuclide	$J^\pi$	$\Gamma_f$ from $\alpha^a$ (MeV)	$\Gamma_f$ from the Resolved Resonances
$^{233}\text{U}$	$2^+$	1140	314 ( $E_n < 60$ eV) <sup>b</sup>
	$3^+$	467	
$^{235}\text{U}$	$3^-$	380	65.1 <sup>c</sup> ( $E_n < 50$ ) or 122 <sup>d</sup> ( $E_n < 61$ )
	$4^-$	210	
$^{239}\text{Pu}$	$0^+$	2600	2800 <sup>c</sup>
	$1^+$	12	55
$^{241}\text{Pu}$	$2^+$	654	443 <sup>d</sup>
	$3^+$	280	280

<sup>a</sup>Kikuchi, Y., and An, S., submitted to J. Nucl. Sci. Tech.

<sup>b</sup>Stern, J. R., BNL-325, 2nd ed., Suppl. 2.

<sup>c</sup>Schmidt, J. J., KFK-120 (1966).

<sup>d</sup>Yiftah, S., et al., IA-1152 (1967).

Secondly, the statistical deviations due to the small sampling are investigated. The random-number method is used for this purpose. The process is as follows:

The mean values of fission width, reduced neutron width, and level spacing are given as the input data. The mean values deduced from the value of  $\alpha$  in the keV region are used for the input data for fission width. The energies and the resonance parameters of each resonance are determined from these input data and random numbers using the Wigner distribution and the  $\chi^2$  distribution, respectively, below several tens of eV. From this set of resonance levels, the averaged value of the fission width, the capture and fission cross sections, and  $\alpha$  are calculated. These average values are expressed with a bar ( $\bar{\Gamma}_f, \bar{\sigma}_f, \bar{\sigma}_c, \bar{\alpha}$ ). This  $\bar{\Gamma}_f$  is, of course, different from the input value because of the statistical deviation of the small sampling.

The calculations are repeated 400 times for each nuclide in order to study the statistical behavior of  $\bar{\Gamma}_f, \bar{\sigma}_f, \bar{\sigma}_c$ , and  $\bar{\alpha}$ . The mean values of each averaged value after 400 histories are expressed by a bracket ( $\langle \bar{\Gamma}_f \rangle \dots \langle \bar{\alpha} \rangle$ ).

The input data and the mean values of 400 histories are listed in Table I.A.2. The 90% confidence intervals are tabulated and compared with the resolved resonance parameters in Table I.A.3.

TABLE I.A.2. Input and Output Mean Values

Spin Energy Range:	<sup>233</sup> U		<sup>235</sup> U		<sup>241</sup> Pu	
	2 <sup>+</sup>	3 <sup>+</sup>	3 <sup>-</sup>	4 <sup>-</sup>	2 <sup>+</sup>	3 <sup>+</sup>
	<63 eV		<50 eV		<63 eV	
Input D, eV	1.88	1.62	1.06	1.06	2.04	1.76
$\Gamma_n^0$ , (MeV) <sup>1/2</sup>	0.207	0.178	0.097	0.097	0.265	0.229
$\Gamma_f$ , MeV	1139	467	380	212	655	280
$\nu_f$	4	2	3	2	2	1
$\Gamma_\gamma$ , MeV	45	45	47.9	47.9	44	44
Output $\langle \bar{\Gamma}_f \rangle$ , MeV	1133	458	377	210	661	276
$\langle \bar{\Gamma}_f^{(J-Mix)} \rangle^a$ , MeV	772		293		453	
$\langle \bar{\alpha} \rangle$	0.169		0.362		0.418	
$\langle \bar{\sigma}_f \rangle$ , b	84.7		67.4		83.1	
$\langle \bar{\sigma}_c \rangle$ , b	14.0		24.0		33.6	

<sup>a</sup>Mean value of both spin sequences.TABLE I.A.3. The Deviation of the Average Values  
(90% Confidence Intervals)

	<sup>233</sup> U		<sup>235</sup> U		<sup>241</sup> Pu	
$\bar{\sigma}_c / \langle \bar{\sigma}_c \rangle$	0.66	1.65	0.66	1.39	0.53	1.65
$\bar{\sigma}_f / \langle \bar{\sigma}_f \rangle$	0.70	1.36	0.69	1.31	0.66	1.41
$\bar{\alpha} / \langle \bar{\alpha} \rangle$	0.61	1.60	0.68	1.39	0.55	1.77
$\bar{\Gamma}_f^{(I-1/2)} / \langle \bar{\Gamma} \rangle$	0.79	1.20	0.80	1.20	0.71	1.34
$\bar{\Gamma}_f^{(I+1/2)} / \langle \bar{\Gamma} \rangle$	0.72	1.29	0.74	1.27	0.62	1.40
$\bar{\Gamma}_f^{(J-Mix)} / \langle \bar{\Gamma} \rangle$	0.82	1.19	0.81	1.18	0.76	1.26
$\bar{\Gamma}_f$ in resolved region	0.44 (BNL-325)		0.22 (BNL-325)		(2 <sup>+</sup> ) 0.68	(1A-1152)
$\bar{\Gamma}_f / \langle \bar{\Gamma} \rangle$			0.42 (ENDF/B)		(3 <sup>+</sup> ) 0.61	

Although 400 histories are not enough, the following rough conclusions are possible:

- 1) The statistical deviation of  $\bar{\Gamma}_f$  is small, although those for  $\bar{\sigma}_f$ ,  $\bar{\sigma}_c$ , and  $\bar{\alpha}$  are relatively large.
- 2) The disagreements between the fission widths deduced in the keV region and those in the resolved region cannot be explained on the basis of statistical behavior for U-233 and U-235.
- 3) The average fission widths in the resolved region are just on the minimum border line of 90% confidence intervals for Pu-241, and the decision is very difficult.

Finally, quasi-resonance interpretation will be discussed. When the ratio  $\Gamma/D$  is large, the observed resonances do not correspond to the eigenstates of the R matrix, but to quasi-resonances in which the mean fission widths of the levels are greatly underestimated and their spacing overestimated because of the interference between levels.

The probability of occurrence of the quasi-resonance was proposed by Lynn.\* He considered the relative magnitude of the sum of the total widths ( $x$ ) of two neighboring levels to their spacing ( $D$ ). According to his criteria, the probability that  $x$  is greater than a factor of  $k$  multiplied by  $D$  is given as

$$P\nu(x \geq kD) = \frac{1}{\Gamma(\nu)} \left( \frac{\nu}{2\bar{x}} \right)^\nu \frac{\pi}{2\bar{D}^2} \int_0^\infty dD e^{-\pi D^2/4\bar{D}^2} \int_{kD}^\infty dx x^{\nu-1} e^{\nu x/2x},$$

where  $\nu$  is the number of degrees of freedom of total width. A slight quasi-resonance effect will appear for  $k \geq 2$  and dramatic quasi-resonance effects can be expected for  $k \geq 4$ .

In our case where the fission widths predominate over the other partial widths, we can replace the total widths with the fission widths. The probabilities of occurrence for the quasi-resonance are calculated and shown in Table I.A.4 for each spin state.

TABLE I.A.4. The Probabilities of Quasi-resonance Effects

Nuclide	Spin	$\nu_f$	$P(\chi \geq \bar{D})$	$P(\chi \geq \bar{D})$
$^{233}\text{U}$	$2^+$	4	0.25	0.099
	$3^+$	2	0.10	0.056
$^{235}\text{U}$	$3^-$	3	0.19	0.056
	$4^-$	2	0.10	0.029
$^{241}\text{Pu}$	$2^+$	2	0.10	0.029
	$3^+$	1	0.036	0.0097

Suppose that the widths of the quasi-resonances are negligibly small and  $\langle \bar{\Gamma}_f \rangle$  values are corrected to be smaller. The corrected  $\langle \bar{\Gamma}_f \rangle$  are tabulated and compared with the resolved resonance parameters in Table I.A.5.

As a final conclusion, disagreements for U-233 and U-235 cannot be explained, even if the quasi-resonance effects are considered.

\*Lynn, J. E., The Theory of Neutron Resonance Reactions, Clarendon Press, Oxford (1968).

TABLE I.A.5. The Comparisons after Corrected with the Quasi-resonance Effect

Nuclide	Spin	$\bar{\Gamma}_f$ (MeV)		$\bar{\Gamma}_f$ in Resolved Region
		Mean Value	90% Confidence Interval	
$^{233}\text{U}$	$2^+$	855	675-1026	
	$3^+$	420	302-542	
	J-mix	611	501-727	314
$^{235}\text{U}$	$3^-$	304	243-365	
	$4^-$	191	141-243	
	J-mix	247	200-291	65.1 or 121
$^{241}\text{Pu}$	$2^+$	595	422-797	443
	$3^+$	266	165-372	280
	J-mix	418	318-526	

The fission widths from channel theory are not defined precisely for U-233 and Pu-241 because of lack of sufficient experimental data for  $\alpha$  from which they are deduced. The fission widths of U-235 are, however, deduced very precisely. Hence it is very disturbing that the disagreements for U-235 cannot be explained by means of the three possible causes considered above. This problem will be pursued.

(ii) Analysis of Neutronic Characteristics of Reactors and Fuel Cycles (D. A. Meneley)

Last Reported: ANL-7632, pp. 2-4 (Oct 1969).

An evaluation of neutron cross sections to be used in the core design study of a 1000-MWe LMFBR has been conducted. The study has centered around the cross sections produced from ENDF/B, and also around modifications of those cross sections for U-238 and Pu-239. The evaluation consisted of comparing neutronic quantities calculated with ENDF/B and modified cross sections to experimental results for appropriate critical assemblies.

The modifications are based on recent experiments and analytical comparisons. Recent measurements at Argonne of the U-238 cross sections have resulted in lower values of the inelastic-scattering cross section above 1.0 MeV. Small changes in  $\sigma(\eta, \gamma)$  of U-238 have been included between 4 and 100 keV. The Pu-239 capture and fission cross sections of Pitterle have been modified between 2 and 183 keV to take account of the evaluation of James and Patrick\* and the fission-ratio ( $^{239}\text{Pu}/^{235}\text{U}$ ) measurement of Poenitz,\*\* but the values of  $\alpha$  have been held constant.

\*James, G. A., and Patrick, B. H., AERE-M-2065 (Amended) (1965).

\*\*Poenitz, W., Trans. ANS 12(2), 742 (1969).

The neutronic parameters obtained with the new cross-section set, as well as a set generated from an earlier edition of ENDF/B, were compared with experimental results from ZPR-3 Assembly 48 and ZEBRA 3. Both critical assemblies were loaded with Pu-239 and U-238. Assembly 48 also contained sodium and carbon, which resulted in a softer spectrum than exhibited by ZEBRA 3. The atom densities for Assembly 48 and ZEBRA 3 are given in Table I.A.6. The values for the 1000-MWe core are provided for comparison.

TABLE I.A.6. Core Compositions of Assembly 48, ZEBRA 3, and 1000-MWe LMFBR ( $10^{24}$  atoms/cm<sup>3</sup>)

Nuclide	Assembly 48	ZEBRA 3	1000-MWe LMFBR <sup>a</sup>
Pu-239	$1.645 \times 10^{-3}$	$3.465 \times 10^{-3}$	$8.6976 \times 10^{-4}$
Pu-240	$1.07 \times 10^{-4}$	$1.83 \times 10^{-4}$	$3.683 \times 10^{-4}$
Pu-241	$1.1 \times 10^{-5}$	$1.6 \times 10^{-5}$	$4.9699 \times 10^{-5}$
Pu-242	$4 \times 10^{-7}$	-	$2.6105 \times 10^{-5}$
U-235	$1.6 \times 10^{-5}$	$2.28 \times 10^{-4}$	$1.0387 \times 10^{-5}$
U-238	$7.405 \times 10^{-3}$	$3.156 \times 10^{-3}$	$6.7042 \times 10^{-3}$
Fe	$1.018 \times 10^{-2}$	$4.559 \times 10^{-3}$	$1.325 \times 10^{-2}$
Ni	$1.119 \times 10^{-3}$	$3.21 \times 10^{-4}$	$2.32128 \times 10^{-3}$
Cr	$2.531 \times 10^{-3}$	$8.18 \times 10^{-4}$	$3.2884 \times 10^{-3}$
Na	$6.23 \times 10^{-3}$	-	$7.7833 \times 10^{-3}$
Mn	$1.06 \times 10^{-4}$	-	-
Mo	$2.06 \times 10^{-4}$	-	$4.836 \times 10^{-4}$
Al	$2.33 \times 10^{-4}$	-	-
C	$2.077 \times 10^{-2}$	-	-
Cu	-	$4.794 \times 10^{-3}$	-
Ta	-	-	$9.0688 \times 10^{-5}$
O	-	-	$1.6681 \times 10^{-2}$

<sup>a</sup>Fission products not included in table.

The neutron calculations were carried out in the same procedure as were used in benchmark studies of the Cross Section Evaluation Working Group (CSEWG).<sup>\*</sup> First, two 26 broad-group sets with 1/2 lethargy widths were generated by MC<sup>2</sup> using the current ENDF/B library tape and core compositions of Assembly 48 and ZEBRA 3. The Pitterle data for Pu-239 were used to generate the weighting spectra for the two sets. The other nuclide data employed in producing the weighting spectra were the same as for the earlier ENDF/B.

<sup>\*</sup>Davey, W. G., and Hess, A. L., CSEWG Newsletter, Feb. 21, 1969.



Then a series of spherical transport ( $S_n = 4$ ) calculations were performed to evaluate the effect of the various cross sections on the eigenvalue of Assembly 48 and ZEBRA 3. The results are presented in Table I.A.7. A previously developed cross section set,\* which was obtained from an earlier ENDF/B tape without Pitterle's data for Pu-239, served as the set for Case A. The new ENDF/B tape, with both old and new data, was used to produce the new cross-section set for Cases B through G. Cases C through G represent variations upon the base problem, Case B.

TABLE I.A.7. Eigenvalues Obtained for ZPR-3 Assembly 48 and ZEBRA 3 from Spherical Transport Calculations Using Various Cross Sections

Case:	"Old" Set	"New" Set with Present ENDF/B					
	A	B	C	D	E	F	G
Critical	Earlier ENDF/B	Pitterle's Pu-239	Mod. U-238	Mod. U-238, Pu-239	Case A's Pu-239	Pitterle's Mo	U-238 I
ZPR-3							
Assembly 48	0.9865	0.9882	1.0038	0.9957	0.9878	0.9895	0.9894
ZEBRA 3	0.9536	0.9752	1.0033	0.9990	0.9567	-	0.9911

Case B differs from Case A only in that Pitterle's data for Pu-239 were used in the generating of the weighting spectra and in calculating the eigenvalues. The broad-group cross sections for U-238 have been modified in Case C, and those for both U-238 and Pu-239 have been modified in Case D (as described above). Case E used the Pu-239 cross sections from Case A and the cross sections from Case B for all other nuclides; new molybdenum cross sections were substituted for the previous ones in Case F. Case G used U-238 cross sections in which previous total inelastic data obtained at ANL were substituted for the ENDF/B values.

The use of the new cross-section set with its various modifications brings the eigenvalues of Assembly 48 and ZEBRA 3 closer to unity. The eigenvalues obtained with the modified Pitterle's Pu-239 and U-238 (ENDF/B's) cross sections are 0.9957 for Assembly 48 and 0.9990 for ZEBRA 3. The modification for molybdenum (Case F) results in an additional 0.13% increase in  $k_{eff}$ . The use of Pitterle's Pu-239 data (unmodified) instead of the ENDF/B data yields an ~0.5% and ~2.3% increase in the eigenvalue of Assembly 48 and ZEBRA 3, respectively (Cases B and E). A larger increase of the eigenvalue with Pitterle's data was seen in ZEBRA 3 because its harder spectrum reduces the negative effect of a higher capture cross section in the low keV region, while the positive contribution of higher  $\nu$  values remained relatively unchanged. The modification of the U-238 inelastic scattering cross sections produced (Case C) an increase in the  $k_{eff}$ 's of both criticals; the larger increase in ZEBRA 3's eigenvalue is again due to its harder spectrum. The eigenvalues of both criticals were reduced by 0.5-0.7% upon the modification to Pitterle's Pu-239 cross sections (Case D).

\*Kallfelz, J. M., et al., ANL, private communication.

As was mentioned previously, the weighting spectra of the new and old cross-section sets were generated from different Pu-239 data; otherwise they were produced in an identical manner. The influence of the slightly different weighting spectra is seen in the slightly different results for Cases A and E. The change of U-238 inelastic cross section in (Case G) resulted in increasing the eigenvalue of both criticals, but not as large as was produced by the modification in Case C.

The modifications to the present ENDF/B improve agreement between the measured and calculated values presented here and are being incorporated into the cross section set for the core design study.

b. Fast Critical Experiments--Theoretical Support--Idaho

- (i) ZPR Heterogeneity Method Development (W. G. Davey and R. G. Palmer)

Last Reported: ANL-7606, pp. 8-11 (Aug 1969).

(a) Extended Equivalence between Homogeneous and Heterogeneous Resonance Integrals in Slabs. Currently nearly all codes for preparation of cross-section sets utilize the two-region cell equivalence principle in the resonance-energy range. This method gives good results for the usual arrangement of power-reactor pin fuel. In many of the zero-power fast criticals, however, a given resonance absorber can exist in plates at different concentrations and with different diluents. For example, U-238 in the ZPPR materials inventory exists in the forms  $U_3O_8$ , U, Pu-U-Mo, and  $UO_2$ . The object of this study has been to extend the equivalence relation from the A-M-A-M... lattice to an A-M1-B-M2-A... lattice and possibly beyond. Here M represents a diluent plate.

Based on Wigner's rational approximation, a typical equivalence relation is<sup>†</sup>

$$\sigma_p^* = \sigma_p + \frac{a}{N\bar{\ell}} \frac{1 - c}{1 + (b - 1)c} \quad (1)$$

The notation throughout is that of Dresner;<sup>††</sup> a and b are empirical constants, usually about 1.27 and 1.2, respectively. In applying this simple equivalence principle (SEP) to a lattice with four regions per unit cell, one is forced to ignore any difference between absorber plates and to average the Dancoff factors of the diluent plates. The derivation of the SEP has been modified to treat four-region cells.

<sup>†</sup>Levine, M. M., Resonance Integral Calculations for U-238 Lattices, Nucl. Sci. Eng. 16, 271 (1963).

<sup>††</sup>Dresner, L., Resonance Absorption in Nuclear Reactors, Pergamon Press (1960).

The resulting extended equivalence principle (EEP) for absorber atoms in Plate A is

$$I = I(\sigma_{pA}^*) + \frac{\alpha N_B \bar{\ell}_B c_{ave}}{N_A \bar{\ell}_A + N_B \bar{\ell}_B} [I(\sigma_{pB}) - I(\sigma_{pA})], \quad (2)$$

where

$$\sigma_{pA}^* = \sigma_{pA} + \frac{a\{1 - \bar{c}^2 + (1 - c_{ave}) \kappa N_B \bar{\ell}_B\}}{N_A \bar{\ell}_A \left[ 1 + \frac{N_B \bar{\ell}_B}{N_A \bar{\ell}_A} c_{ave} + \kappa N_B \bar{\ell}_B \right]} \frac{1}{1 + (b-1) c_{ave}}.$$

Here  $I(\sigma_p)$  is the homogeneous resonance integral corresponding to a non-resonant cross section  $\sigma_p$ . If  $c_1$  and  $c_2$  are the Dancoff factors for the two-moderator regions,  $c_{ave} = (c_1 + c_2)/2$  and  $\bar{c}^2 = c_1 c_2$ . Best values of  $\alpha$  and  $\kappa$  appear to be 0.5 and 100, respectively. Note that the EEP reduces to the SEP for the case in which the A and B plates are identical and  $c_1 = c_2$ .

Extensive numerical comparisons were made of the accuracy of the two equivalence principles, as applied to four-region unit cells. The transport theory code RABID<sup>†</sup> was used to compute exact resonance integrals for a wide range of parameters. The absorber plates were taken to be 0.5 cm thick, and their absorber atom densities allowed to vary from 0.0001 to 0.05 cm<sup>-3</sup> with the restriction that  $N_A$  and  $N_B$  never differ by more than a factor of 10 for any given lattice. The moderator region thicknesses varied from 0.1 to ~5 mean free paths. Admixed diluent in the absorber plates was permitted in widely varying amounts. Typical U-238 resonances were examined singly and in groups, and the EEP was never found to be in error by more than 6%. However, the SEP varied considerably in its accuracy. The results are given in Table I.A.8.

TABLE I.A.8. Comparison of Calculations of the Effective Resonance Integral (I) by the Simple Equivalence Principle and the Extended Equivalence Principle

Plate A		Plate B		Moderator Plate Thickness (mfp)	% Error in I			
Absorber (atoms/cm <sup>3</sup> )	Diluent to Absorber Ratio	Absorber (atoms/cm <sup>3</sup> )	Diluent to Absorber Ratio		SEP		EEP	
					A-Plate	B-Plate	A-Plate	B-Plate
0.05	4	0.01	0	0.098	1.2	-6.8	0.3	-4.2
				0.393	-0.8	4.1	0.4	0.6
				3.14	1.6	0.7	1.6	0.5
0.001	4	0.01	0	0.098	51	-18	0.5	-0.8
				0.393	20	-13	-2.2	-1.7
				3.14	2.2	0.1	1.8	0.4
0.001	5	0.005	1	0.098	28	-14	-2.5	-0.3
				0.393	10.5	-8.6	-2.8	-0.4
				3.14	2.0	1.1	1.7	1.3
0.01	0	0.01	5	0.098	-12.5	9.8	-3.5	1.5
				0.393	-4.0	1.6	0.1	-2.3
				3.14	0.3	-0.1	0.4	-0.2

Resonance Parameters:  $E_0 = 3783.7$  eV;  $\Gamma_n = 0.2768$  eV;  $\Gamma_v = 0.0246$  eV;  $g = 1.0$ .

<sup>†</sup>Olson, Arne, P., Resonance Absorption in Multiplate Reactor Cells by Integral Transport Theory, Trans. Am. Nucl. Soc. 11, 301 (1968).

## 2. Experimental Reactor Physics

### a. Fast Critical Experiments--Experimental Support--Idaho

#### (i) Neutron-spectrum Measurements--System Development (S. G. Carpenter and G. G. Simons)

Last Reported: ANL-7561, pp. 3-4 (March 1969).

A small pulse-shape-identification (PSI) circuit designed to distinguish between neutron- and gamma-ray-induced pulses in the NE-213 scintillation solution has been constructed. This circuit, shown in Fig. I.A.1, is an integral part of an operating high-efficiency fast-neutron-spectrometer detector assembly consisting of the liquid organic scintillation solution, light pipe, photomultiplier tube, tube voltage divider, preamplifier, and static shield.

Identification of  $\gamma$  radiation and neutrons is obtained by comparing the shape of the pulse generated at the 14th dynode of an RCA 6810A photomultiplier tube with a fixed pulse shape obtained by differentiating and stretching the pulse generated by the current from the anode.

Following such identification in the above PSI circuit, the PSI pulses are amplified and shaped in a pulse-shaping linear amplifier in order to facilitate leading edge timing. The resulting separated logic signals are unique in time for gamma rays and neutrons.

(ii) Neutron Spectra Measurements in FTR-2. Measurements of fast-neutron spectra were made over the energy range from 329 eV to 2.37 MeV with the proportional proton-recoil spectrometer in the reflector and shield of the ZPPR/FTR-2. Neutron spectra were measured close to the axial midplane at matrix positions 137-23 and 137-15, which correspond to locations near the center of the reflector and shield annuli, respectively (see Progress Report for October 1969, ANL-7632, Fig. I.A.5, p. 17).

The neutron spectrum measured in the reflector is shown in Fig. I.A.2. For this measurement, the fueled safety, control, and poison safety rods were completely withdrawn. Under these conditions, the reactor was 1.67%  $\Delta k/k$  subcritical.

During the shield-spectrum measurement (see Fig. I.A.3) the reactor was 0.0896%  $\Delta k/k$  subcritical. All the poison rods were completely withdrawn. Also, Control Rods No. 1 at (135-39), No. 3 at (139-43), and No. 4 at (239-43) were completely withdrawn. Control Rods No. 2 at (239-35) and No. 5 at (139-35) and all fueled safety rods were completely inserted, while Control Rod No. 6 at (235-39) was withdrawn 1.704 in.

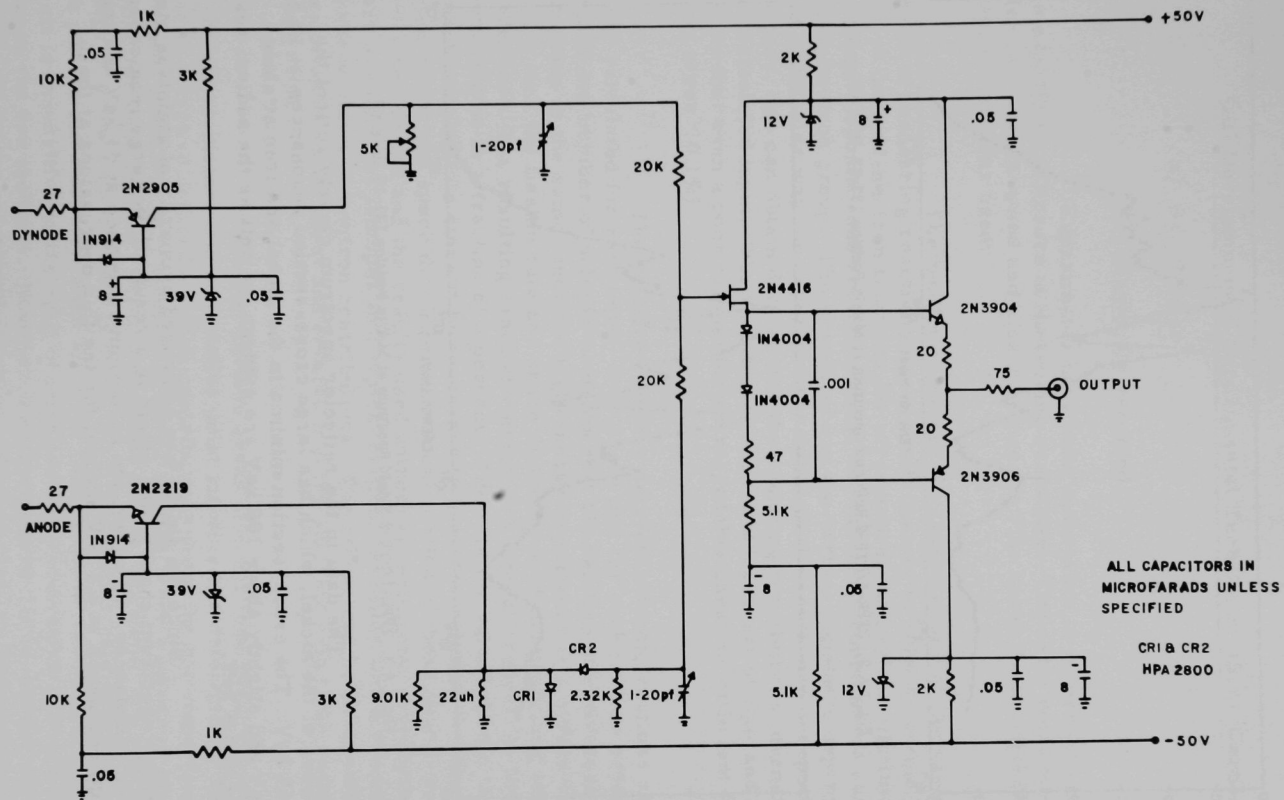


Fig. I.A.1. Circuit for Pulse-shape Identification

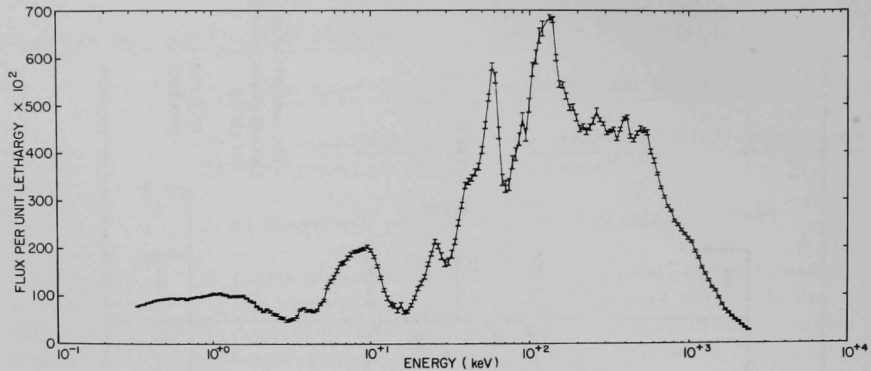


Fig. I.A.2. ZPPR-1/FTR-2 Reflector Spectrum at Matrix Position 137-23 9/18/69

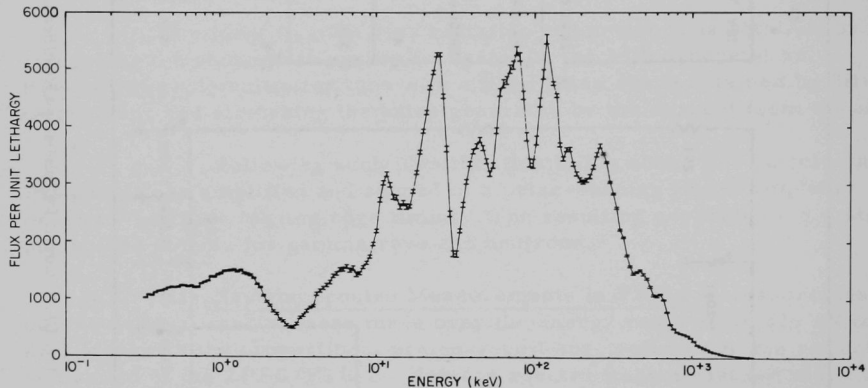


Fig. I.A.3. ZPPR-1/FTR-2 Shield Spectrum at Matrix Position 137-15 9/18/69

The data in the reflector spectrum clearly reflect the presence of the nickel, which has large cross-section resonances at 15.5 and 65 keV. The cross-section minima in the nickel and iron at about 30 keV and slightly above 100 keV are evident, as well as the sodium resonance at 2.8 keV.

Since the shield was composed primarily of stainless steel, the major spectrum shape in the shield is a result of the large iron cross-section resonances. However, the chromium resonance at 53 keV and the sodium resonance at 2.8 keV account for the flux depressions at these energies.

(iii) Development of Experimental Techniques (S. G. Carpenter)(a)  $\beta_{\text{eff}}$  Studies

Not previously reported.

Experiments have been undertaken to investigate possible experimental errors in measuring reactivity. The usual point kinetics model has been assumed and a search made for the areas most sensitive to the approximations used.

The input parameters necessary in any of the various methods of measuring reactivity are a power history in relative terms, the effective delayed-neutron fractions for all isotopes, the neutron lifetime, the effective spontaneous neutron source, and the decay constant for each delayed-neutron group. The importance of the various constants depends on the particular way the experiment is done. If the reactivity is reported in dollars, one can obtain data so that the resulting reactivity is insensitive to all calculated input. The results are almost independent of  $\beta_{\text{eff}}$  and lifetime, so that even a poor calculation or reasonable guess is sufficient (resulting error  $< 0.1\%$ ).

The relative effective delayed-neutron fractions are usually calculated for each core. It is likely that for each isotope producing a significant number of delayed neutrons that the relative effectiveness of each group is the same since the high-energy importance is a slowly varying function, and the fission rate and space distribution of the producing isotope are identical. The resulting reactivity error in a typical critical for this approximation is a fraction of a percent. The relative value between isotopes is much less certain since it is necessary to know the relative  $\beta$  values, fission rates, and space distributions. A calculation of these quantities is usually performed and the results used without experimental verification. There are only two isotopes in a typical critical assembly which produce significant delayed-neutron contributions. The others can be estimated from calculation or experiment and entered into the analysis with little resulting error ( $< 1\%$ ).

The most obvious areas of error then reduce to obtaining the power history which satisfies point kinetics and determining the relative effective delayed-neutron contributions from the two important isotopes. Additionally, counter placement and electronics linearity must be studied for each reactor, but this presents no real problem. If a reactivity change of a few tens of cents is made in a critical assembly operating at a high power, the reactivity soon after the change can be calculated, and the result is insensitive to the split of effective delayed-neutron production between the two isotopes. However, as time goes on, an incorrect assumption will cause the calculated reactivity after the drop to deviate from the



initial correct value. At even longer times (lower powers), the assumed spontaneous source in the critical will become important, and this may therefore also be found. In principle, this power history could be used to determine all the delayed-neutron parameters, but in practice it is not necessary or reasonable. The data of Keepin together with only the one ratio of effective betas is sufficient to correlate all the data.

Four cores have been studied in this manner. All the results show that the ratio of the effective delayed-neutron production rate in U-238 to that in the fissile material is a few percent less than given by calculations using MACH-1 diffusion theory (see Table I.A.9). An error of this magnitude could easily arise from errors in beta, fission rate, or adjoint flux, and there is thus no significant evidence of a real error in the effective value of beta for U-238. In any case, an error of this magnitude is of little practical importance, since it would cause only a 1 or 2% error in the reactivity calibrations. The uncertainty in this experimental result leaves only a small contribution to reactivity error.

TABLE I.A.9. Comparison of Measured and Calculated  $\beta_{\text{eff}}$  Ratios in Four Cores

Core	Fuel	$\left[ \frac{\beta_{\text{eff}} (\text{U-238})}{\beta_{\text{eff}} (\text{Pu-239 or U-235})} \right]_{\text{Meas}}$	$\left( \frac{\text{Fissions U-238}}{\text{Fissions Total}} \right)_{\text{Calc}}$
		$\left[ \frac{\beta_{\text{eff}} (\text{U-238})}{\beta_{\text{eff}} (\text{Pu-239 or U-235})} \right]_{\text{Calc}}$	
ZPR-3 Assembly 56	Pu	$0.92 \pm 0.02$	0.106
ZPPR FTR I	Pu	$0.96 \pm 0.02$	0.107
ZPR-3 Assembly 57	U-235	$0.88 \pm 0.06$	0.053
ZPPR FTR II	Pu	$0.93 \pm 0.03$	0.110

In comparison with theory, a calculated value for beta effective is used to convert the measured result to the calculated units. It is possible that any difference between experiment and calculation occurs in this conversion. This aspect is being studied by measuring the apparent reactivity of a spontaneous neutron source of known strength. The method for apparent reactivity measurements is similar to that described above for "real" reactivity determinations. The result, which should be accurate to 2% or better, including any errors arising from input data, is equal to  $S_0/\nu F \beta_{\text{eff}}$ . The neutron-production rate from fission in the assembly is  $\gamma F$ . Using absolute fission rates and fission-neutron importance traverses, one can then find  $\beta_{\text{eff}}$ . This measurement is also being made for several cores. The results taken together should reduce any reactivity disagreement between calculation and experiment, to either the calculation or an incomplete calculational description of the true environment of the perturbation experiment.

(b) Development of a Computer Code for Reduction of Differential Gamma-ray Data. A preliminary version of the computer code RAID (Reduction of Activation Integral Data) has been made operational on the SEL-840 MP. The code provides complete processing of large amounts of differential gamma-ray data.

The code takes magnetic data tapes prepared by an SEL-810A (operating as up to three independent multichannel analyzers) and provides calibration, peak location and analysis, identification of parent isotope, all necessary corrections, and a thorough statistical analysis of the results. The present version is used for analysis of activation and fission data from Ge(Li) detectors only, but the capability is present for use on scintillation or solid-state charged-particle detectors.

The code consists of three major sections, which operate in a chained mode.

The first section decodes the output of the analyzer-computer, does certain preliminary calculations, and sorts data from each foil into time-sequential order for each of the counters being used. Data at this point are in the form of 959-channel differential spectra for each time each foil was counted. Sense-switch options in this section allow several forms for output of raw data.

The second section of the code determines the location of all statistically significant photopeaks present in each spectrum, and finds the appropriate peak integral, background, and statistical uncertainty for each peak.

The third section finds the appropriate energy calibration for each spectrum as observed, and provides an identification (by isotope, half-life, energy, and transition intensity) through reference to a library of gamma-ray data. It then summarizes and statistically analyzes up to 40 repeated counts of each gamma ray in each foil, and makes corrections for decay, saturation, counter efficiency (as a function of energy if this is available), and branching of the decay. The final printout for each gamma ray is proportional to the absolute concentration of the parent isotope.

The only human intervention in the counting and processing of the data are 1) to mount the foils in automatic sample changers, 2) to provide the analyzer-computer with initial conditions, and 3) to change the output magnetic tape of raw data from the analyzer-computer to the SEL-840 MP.

The system has been used to obtain and process large activation traverses made in the FTR-2 core in ZPPR. The capability was

demonstrated for handling the measurement of the equivalent of 130 separate foils in less than 24 hr, and obtaining precisions of the order of 1 or 2% from each of them. (These numbers depend on both the half-life and activation levels.)

Modifications to provide more precise decompositions of the activity of very complicated spectra (such as raw fission-product data), a more extensive library of gamma rays, and to provide additional flexibility in counting and calibration methods have been written and will be incorporated in the operating system in the near future.

(c) Development of Back-to-back Proportional Counter for Fission and  $(n,\alpha)$  Events. A small back-to-back proportional counter for the measurement of fission and exothermic  $(n,\alpha)$  events in any combination has been developed. The counter is cylindrical with an outside diameter of 0.455 in. and an active length of 2.173 in., which matches the drawer width in ZPPR.

The counter is expected to have application in the precise measurement of fission ratios and the comparison of fission in several isotopes to capture in B-10 or Li-6.

The active material is deposited in plane, back-to-back geometry on a stainless steel plate occupying a diameter of the counter. The collecting electrode in each half is a grid of three wires located so as to optimize the resolution of the counter. When operated in the fission-counter mode, the polarizing potential is chosen to provide a gas multiplication of about unity. In the alpha-counting mode, the potential is chosen so that the gas multiplication is several thousand. Each half can be operated independently and simultaneously, and both halves are operated as flow counters using the standard argon-10% methane mixture.

Normal calibration of the counter in terms of mass of the active material is intended to be done by comparison to present absolute fission counters in a thermal-neutron spectrum. The counter, however, is potentially self-calibrating because of the dual operating modes. A fission foil can be alpha-assayed internally in the exact geometry that will thereafter be used for the fission-counter mode, to give the absolute fissile mass. A simple counting-rate ratio in a thermal spectrum then gives the mass of the B-10 in the other half of the counter.

The development model of the counter consists of a U-235 plate of approximately  $100 \mu\text{g}/\text{cm}^2$  and a B-10 plate of about  $10 \mu\text{g}/\text{cm}^2$ . Additional plates containing Li-6 (as LiF) and natural uranium have been prepared by vacuum-deposition techniques. Plates containing the plutonium isotopes are being prepared. It has been possible to determine

that the thickness variations of the deposits are less than 10% in the worst case for the optically transparent LiF. The others are presumably similar, since the deposition technique was identical.

The low-energy end of the spectrum observed in either the fission or alpha-counting modes is determined by the geometry of the counter, and is independent of the energy of the charged particle, provided that certain restrictions are fulfilled by the range of the particle.

The shape of the spectrum is such that extrapolations from reasonable discriminator settings can be made with relative confidence. As a fission counter, for example, it is possible to select a set of operating conditions that produce a discriminator curve having a slope of less than 0.02% change in observed count rate per percent change in discriminator level, over at least 20% of the discriminator range. For nominal settings of the discriminator and a linear extrapolation to zero energy, these operating conditions yield a spectrum where about 1/2% of the fission events are below the threshold.

The performance of the counter on natural alphas of U-235 is relatively somewhat better.

A rough estimate of the gamma sensitivity of the counter was obtained by using the counter in the alpha-counting mode and subjecting it to gamma rays from a large Co-60 source. Under these conditions, a gamma-ray sensitivity of the order of one count per second per R/hr was measured. No gamma sensitivity in the fission-counter mode was detected by this method.

The geometry and operating properties of the counter have been determined to be satisfactory in tests to date. Further investigations of the gamma sensitivity under realistic operating conditions and of the response of the counter to alphas from B-10 and Li-6 are desirable. Some work still remains to be done on the mechanical design and electrical connectors for routine use.

b. Fast Critical Experiments--Experimental Support--Illinois

(i) Development of Experimental Techniques (R. Gold)

Last Reported: ANL-7606, p. 14 (Aug 1969).

(a) Status of ZPR-6 and -9 Processor. The SEL-840 computer associated with the ZPR-6 and -9 assemblies has not yet been formally accepted. Nevertheless, considerable progress has been made in preparing it for use with the reactors. Specifically, the following things have been done:

(1) Two sets of binary scalers for the collection of experimental data have been designed, built, and installed. The first set is a bank of four binary scalers similar in principle to those used for several years on the DDP-24 computer. The second set is a bank of four reversible binary scalers which can count in either direction. These are primarily intended for keeping track of the position of control rods and other movable elements. They incorporate circuitry allowing the use of "Trav-A-Dial" position encoder heads without need for the indicator boxes normally used with such heads.

(2) A complete set of subroutines has been written for preparation of graphs on the CalComp plotter. This was adapted from similar software used for several years on the DDP-24, and is compatible with the latter except for some minor deviations necessitated by the SEL-840 environment.

(3) An "Encode/Decode" routine has been adapted from a similar routine previously developed\* for the DDP-24. This routine is expected to be of great usefulness in fuel-management operations.

(4) Some of the DDP-24 codes for reactor experiments have been converted for the SEL-840, and rod calibrations for ZPR-9 have been successfully performed.

c. FFTF Critical Assembly Experiments--Planning and Evaluation (A. Travelli)

Last Reported: ANL-7632, pp. 5-7 (Oct 1969).

(i) FTR Critical Program with ZPPR. The experiments with ZPPR Assembly 1 were concluded. This ZPPR assembly is the Assembly II of the FTR Resumed Phase-B Critical Experiments Program (FTR-2). The program will now continue with the FTR-3 experiments to be performed with ZPR-9.

(a) Calculation of the Worth of Depleting Central Cylindrical Zones of Various Sizes in FTR-2. The experiments in which the control ring of FTR-2 was gradually removed in preparation for the shielding experiments involved also the progressive depletion of a cylindrical zone of the core, having the same axis and height as the core itself. As described in Progress Report for October 1969, ANL-7632, p. 14, the removal of the boron ring and the depletion of the central zone were accomplished in alternating steps so that the assembly could be kept close to criticality at all times. This procedure made it possible to assess accurately the reactivity change associated with every step and provided an effective tool for testing the computational methods.

\*Cohn, C. E., Encode-Decode Facility for FORTRAN-IV, Software Age 2(8), 16 (Sept 1968).

If the assumption is made that the changes in the controlling configuration do not affect to any considerable extent the reactivity changes associated with a depletion of the central zone, and that the configuration of the central depleted zone does not affect to any considerable extent the reactivity changes associated with the removal of some of the peripheral control drawers, then, as a first approximation, the two problems can be considered separately. The comparison between calculated and measured worths of the peripheral control zones was reported in ANL-7632, p. 7. Here we describe a similar comparison for the worths associated with the steps during which the central zone of FTR-2 was progressively depleted of plutonium.

The calculations were based on the use of the one-dimensional code DIFF-1D\* and of the 29-group cross-section set 29004 (see Progress Report for March 1969, ANL-7561, p. 7). The code was used in cylindrical geometry for a configuration that approximated very closely the FTR-2 configuration after removal of the peripheral control zones.

The axial buckling used in the calculations was obtained by comparing the reactivity of a two-dimensional R-Z calculation for ZPPR Loading 1-120 with the reactivity of a corresponding one-dimensional cylindrical calculation, and by modifying the axial buckling in the latter calculation until the same reactivity was obtained in the two problems. The codes DIFF-1D and DIFF-2D, and set 29004 were used in these calculations, which yielded the value of  $5.905 \times 10^{-4} \text{ cm}^{-2}$  for the axial buckling.

Figure I.A.4 shows the comparison of the computations with the experimental results. The difference in the effective multiplication

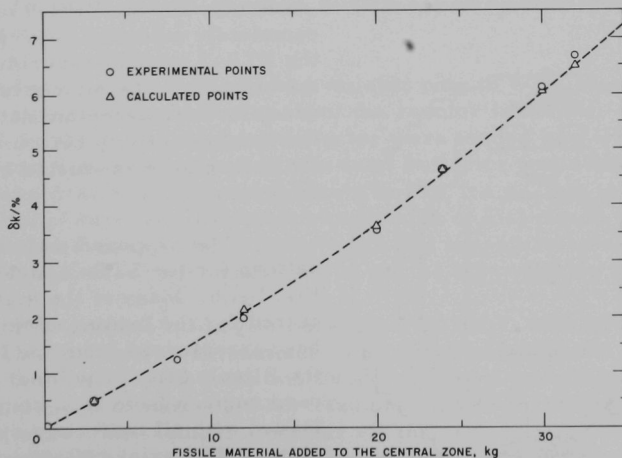


Fig. I.A.4. The Reactivity Effect of Modifying the Size of the Central Depleted Zone in FTR-2

\*Toppel, B. J., ANL-7332 (1967).



constant between any depleted state and the most depleted state considered in the experiments (which corresponds to 495.077 kg of fissile mass in the core) is plotted versus the corresponding difference in fissile mass. Thus, physically, the figure depicts the increase in reactivity that corresponds to replenishment of the central zone from the outside; the largest considered abscissa (31.964 kg) corresponds to a core without any central depleted zone. The experimental difference in reactivity is obtained by adding up the reactivity changes observed in all the steps used to deplete the core from one state to the other while keeping the peripheral control constant. The calculations were run by modifying not only the radius of the depleted zone, but also its composition in agreement with the experimental procedures. This explains the slight differences found in Fig. I.A.4 between the calculated points and the smooth dashed curve that best fits them. The calculations, however, do not take into account accurately the axial distribution of the flux, nor the jagged outlines that made the shapes of the experimentally depleted zones different from cylinders, nor the interference that may have been caused by the presence of the control zones. Especially in consideration of these limitations, the agreement between experiments and calculations as shown in Fig. I.A.4 must be considered quite satisfactory.

### 3. ZPR-6 and -9 Operations and Analysis

#### a. Mockup Experiments (J. W. Daughtry)

Not previously reported.

(i) Preparation for FTR-3 Experiments. Upon completion of the experimental program for ZPR-9 Assembly 25, the ZPR-9 matrix was

completely unloaded in preparation for the FTR-3 critical experiments. After the unloading, the matrix tubes and drawers were decontaminated to reduce the level of activity before assembling the first plutonium-fueled core in the facility.

10<sup>8</sup> SAFETY RODS

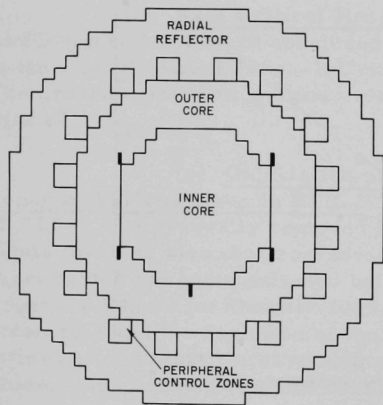


Fig. I.A.5. Matrix Loading Pattern for FTR-3 in ZPR-9

The proposed matrix loading pattern for the FTR-3 core is shown in Fig. I.A.5. Many of the materials required for the loading of this core have been transferred from the Idaho Site to the Illinois Site. The inner and outer core regions have been completely preloaded with all materials except the fuel plates. The axial reflector has been partially loaded. The completion of the axial reflector loading and the loading of the peripheral control zones and the



radial reflector must await the completion of the FTR-2 experiments with ZPPR and the transfer of nickel and  $B_4C$  from ZPPR to ZPR-9.

The drive units for ten boron rods and ten fuel-bearing rods were mounted. The matrix bundles were checked for horizontal and vertical alignment at the locations of the radial sample changer, Doppler oscillator, fine autorod, and coarse autorod.

Facility maintenance is continuing, and final preparations are being made to operate with plutonium fuel.

#### 4. ZPR-3 and ZPPR Operations and Analysis

##### a. Clean Critical Experiments (P. I. Amundson)

Last Reported: ANL-7632, pp. 12-13 (Oct 1969).

Assembly 58 has reached criticality, and measurements to determine the central neutron spectrum and to calibrate the safety and control rods have been made.

Assembly 58 and the subsequent Assembly 59 are to be used to study the persistent discrepancy between calculated and measured central reactivity worths. The basic cell consists of two Pu-Al columns and fourteen graphite columns, and thus naturally follows in the series of benchmark physics assemblies (48, 49, 50, 53, and 54) which have been built on ZPR-3. Assembly 58 has a depleted-uranium reflector, and Assembly 59 will have a lead reflector.

Because the lead will be available only in 4-in. blocks, the core was not assembled symmetrically about the reactor interface. Eleven inches of core and the first 4 in. of axial reflector were loaded into a 15-in. drawer for Half 1, and 9 in. of core and all the axial reflector in a 21-in. drawer for Half 2. These drawer loadings are shown in Fig. I.A.6. Due to Pu-Al inventory limitations, several different arrangements of fuel plates within the columns were necessary. Both nickel-clad and non-nickel-clad plates, as well as different sizes, were combined to utilize the available inventory.

The critical loading is shown in Fig. I.A.7, with 78 drawers in each half. Criticality was determined to be with Control Rod 6 withdrawn 0.66 in. In both halves, the rods and Type-1 drawers contained non-nickel-clad plates, Type-2 contained nickel-clad plates, and the remainder contained both types. The compositions for all the very similar core types, a volume-weighted core average, and for the reflector regions are given in Table I.A.10. In order to obtain uniform composition, including the spring-gap spaces, it was necessary to load the same number of fuel plates in each fuel column. The small quantity of Pu-242 has been included in the Pu-240.

The Pu-241 content has been corrected for decay (half-life of 13.2 yr) since the analysis in 1961, and the low-worth daughter (Am-241) ignored. The uranium blocks in the radial reflector were loaded directly into the matrix tubes. The reflector compositions differ somewhat from those in previous ZPR-3 assemblies as ZPPR pieces were used rather than the ZPR-3 pieces, which were still somewhat active after the high-power run in Assembly 57.

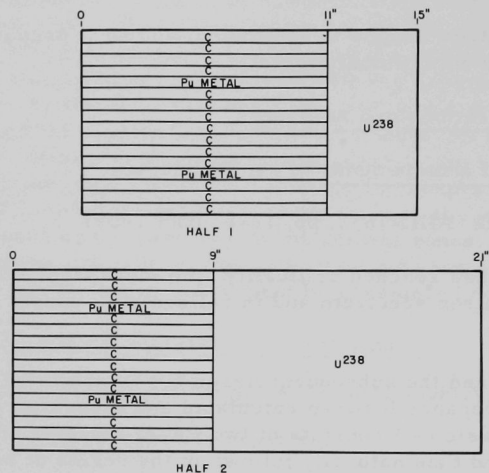


Fig. I.A.6

Core-drawer Loading for  
ZPR-3 Assembly 58

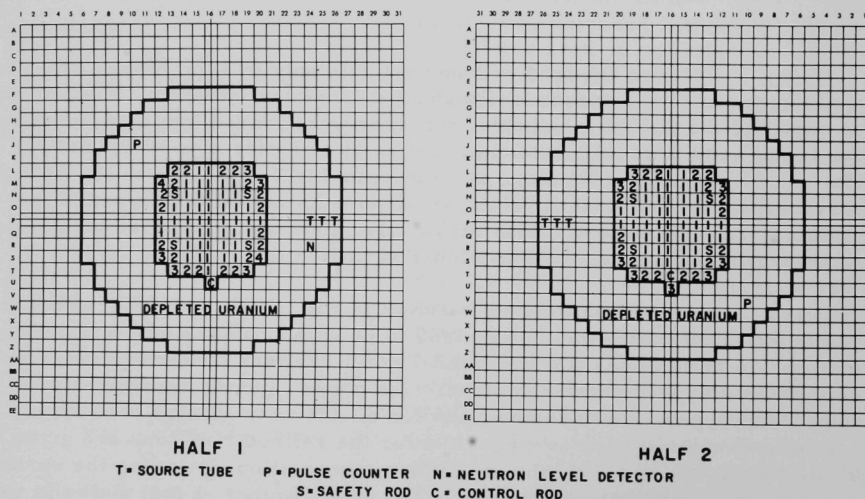


Fig. I.A.7. Reference Core Loading for ZPR-3 Assembly 58 (Loading 12)

TABLE I.A.10. Composition of ZPR-3 Assembly 58 ( $\times 10^{21}$  atoms/cc)

Region	Pu-239	Pu-240	Pu-241	Al	C	Fe	Cr	Ni	Mn	Si	U-238	U-235
Half 1 Rods	2.1054	0.1005	0.0055	0.219	55.09	11.451	2.848	1.247	0.1189	0.1396	-	-
Type 1	2.1054	0.1005	0.0055	0.219	59.33	7.383	1.836	0.804	0.0767	0.0900	-	-
Type 2	2.1012	0.0994	0.0063	0.199	59.33	7.500	1.865	1.115	0.0779	0.0914	-	-
Type 3	2.0906	0.0994	0.0059	0.209	59.33	7.442	1.851	0.947	0.0773	0.0907	-	-
Type 4	2.1097	0.1000	0.0062	0.204	59.33	7.482	1.861	1.060	0.0777	0.0912	-	-
Type 5	2.1232	0.1006	0.0062	0.204	59.33	7.467	1.857	1.054	0.0775	0.0910	-	-
Half 2 Rods	2.1012	0.1003	0.0055	0.219	55.11	11.512	2.863	1.253	0.1195	0.1403	-	-
Type 1	2.1012	0.1003	0.0055	0.219	59.35	7.401	1.841	0.806	0.0768	0.0902	-	-
Type 2	2.0972	0.0992	0.0063	0.198	59.35	7.516	1.869	1.115	0.0780	0.0916	-	-
Type 3	2.1072	0.0998	0.0063	0.203	59.35	7.500	1.865	1.067	0.0779	0.0914	-	-
Core Average	2.1024	0.1001	0.0058	0.213	59.07	7.689	1.912	0.928	0.0798	0.0937	-	-
Radial Reflector	-	-	-	-	-	4.540	1.129	0.494	0.0471	0.0553	38.71	0.086
Axial Reflector	-	-	-	-	-	5.593	1.391	0.609	0.0581	0.0682	39.05	0.086
Spring Gap	-	-	-	-	-	16.85	4.19	1.83	0.175	0.205	-	-

The mass of the critical loading was 101.63 kg Pu-239 and 0.28 kg Pu-241. A cylindrical picture equivalent to Loading 12 is seen in Fig. I.A.8. The axial core dimensions include the front faces of the drawers, which for composition purposes were smeared along the half-core length.

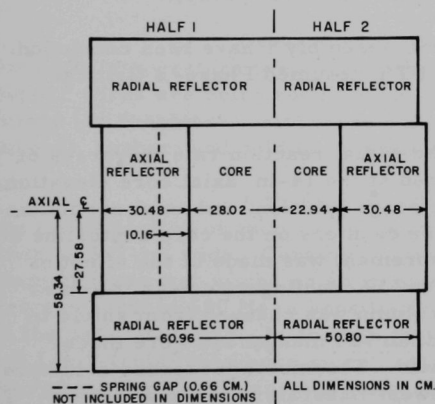


Fig. I.A.8. Equivalent Cylindrical Dimensions for ZPR-3 Assembly 58

The results are shown in Table I.A.11. The total worth of the eight safety rods (2.86%  $\Delta k/k$ ) was well above the required amount of 1.5%  $\Delta k/k$ . The worth curve for Rod 6 showed that fully inserting that rod in the reference loading 12 would have given an excess reactivity of 0.020%  $\Delta k/k$  or 20.8 Ih. Examination of the approach-to-critical curve showed Rod 6 to be equivalent to 0.99 kg edge fuel and, assuming a linear worth curve, the excess reactivity of Loading 12 corresponded to 0.07 kg of edge fuel.

TABLE I.A.11. Worths (%  $\Delta k/k$ ) of Control and Safety Rods

Safety Rod 3 (Half 2)	0.337
Safety Rod 7 (Half 1)	0.378
Control Rod 5 (Half 2)	0.314
Control Rod 6 (Half 1)	0.248
Total 8 Safety Rods	2.860

b. Measurements of Shielding and Neutron Streaming  
(G. G. Simons)

Not previously reported.

The capabilities of measuring fast-neutron spectra pertaining to experimental shielding studies have been advanced by the completion of a liquid organic proton-recoil-type fast-neutron spectrometer system (see Sect. I.A.2.a for a description of the pulse-shape-identification circuit). This spectrometer system will be used to map neutron spectra as well as attenuation of fast neutrons in blankets, reflectors, and shields in the ZPPR and ZPR-3 criticals. Also important shielding data for fast-neutron spectra can be obtained using the Argonne Fast Source Reactor.

c. Mockup Critical Experiments (W. P. Keeney)

Last Reported: ANL-7632, pp. 14-22 (Oct 1969).

The experiments with ZPPR Assembly 1 have been concluded. This assembly was Assembly 2 of the FTR Resumed Phase-B Critical Experiments Program.

In this reporting period, the radial reaction rate traverses of Pu-239, U-238, and B-10 were measured at the 14-in. axial core elevation, both with and without fuel in the fuel-storage position, and axial normalization measurements were made for these counters on the core centerline at elevations of 3, 14, and 22 in. A measurement was made of the effect of B<sub>4</sub>C and shield composition upon the Pu-239 counting rate near the outer edge of the shield as the outer shield column was changed from shield to void to B<sub>4</sub>C. Activation profiles of sodium and manganese were made throughout the core, reflector, and shield. Thermoluminescence detectors were also irradiated for Pacific Northwest Laboratory in the assembly. The loading was then changed to the Reference Core (Loading 1-70), leaving the shield in place. The central fission ratios and ratio of capture in U-238 to fission in U-235 were then measured. Data to aid in the evaluation of a method of measuring B-10 (n, $\alpha$ )/U-235 (n,F) with a thin-film detector was also taken.

## B. Component Development--LMFBR

### 1. Instrumentation and Control

#### a. FFTF Instrumentation (R. A. Jaross)

##### (i) In-Core Flowmeter (T. P. Mulcahey)

##### (a) Tests of Model Probe-type Eddy-current Flowsensors (J. Brewer)

Last Reported: ANL-7632, pp. 31-32 (Oct 1969).

Stability and sensitivity tests are being performed to aid in the determination of a good coil configuration and wire size. Coil-winding procedures and specifications for procurement of gold wire are being prepared.

Ceramic-coated nickel-clad silver wire is being used for high-temperature oven tests; fiberglass-insulated and Formvar-insulated copper wires are being used for low-temperature oven tests. Inconel coil forms (or "bobbins"), with three coil sections per bobbin, are being used. Inconel, copper, and gold have similar thermal-expansion coefficients.

A three-coil-section (Probe No. 7) was constructed; the cross section of each 15/16-in.-OD coil was approximately 1/8 in. deep by 1/2-in. wide. Ceramic-coated nickel-clad silver wire of 15-mil diameter was wet-wound on an Inconel-600 bobbin. With 600-mA (rms) drive current at 500 Hz, a sensitivity of 0.77 mV (rms)/ft/sec was obtained in the oscillatory rig. In an oven test from 700 to 1100°F, there was only a 0.1-mV (rms) unbalance signal. At 1200°F and above, the unbalance signal increased sharply because of faulty insulation; it recovered to normal during the cooling cycle from 950 to 700°F. This configuration showed considerably better results than did probe coils of 1/4-in.-deep cross section.

A three-coil-section (Probe No. 6-3) was constructed; the cross section of each 15/16-in.-OD coil was approximately 1/4-in. deep by 1/2-in. wide. The wire and winding process were the same as for Probe No. 7. With 300-mA (rms) drive current at 500 Hz, a sensitivity of 1.6 mV (rms)/ft/sec was obtained in the oscillating rig. In an oven test from 700 to 1200°F, the unbalance-signal deviation was 1.1 mV (rms). In the cooling cycle, it followed the same path in return. A similar test exhibited 0.8 mV (rms) deviation. Another significant observation was that no change in phase relation occurred between drive current and unbalance signal from 700 to 1200°F.

Probe No. 8, similar to Probe No. 6-3, except dry-wound with fiberglass-insulated, 10-mil-dia copper wire, was oven-tested in the following sequence: 400, 610, 400, 720, 400, 900, 400, and 1000°F, with 300 mA at 500 Hz. The unbalance-signal deviation was never more than 0.1 mV (rms) except at greater than 900°F, where it changed by 1.8 mV up to 1000°F. When cooled to 400°F, it returned to the original level. An RC-balancing arrangement was also tried with this probe and, as expected, it was very sensitive to thermal gradients; therefore, it is advisable to continue with the voltage-balancing arrangement.

A Probe No. 9, similar to Probe No. 7 except dry-wound and with eight wire layers per coil instead of six, was fabricated for tests to be run piggyback with a permanent-magnet probe in the CAMEL loop. With 300-mA (rms) drive current at 500 Hz, it exhibited a sensitivity of 0.746 mV (rms)/ft/sec. With one oven-test from 700 to 1200°F, the unbalance signal rose from 0.2 to 0.3 mV (rms); when the probe was cooled to 700°F, the unbalance signal returned to 0.25 mV (rms). This is a total deviation of only 0.1 mV (rms) for a first-run oven test. This probe is being tested in CAMEL.

Three individual coil bobbins to make the equivalent of Probe No. 9 have been made and wound with fiberglass-insulated, 10-mil-dia copper wire to show the magnitude of physical effects on balance. These tests were made with 300-mA drive current at 500 Hz. Removal of one turn of wire from one secondary coil caused a balance shift of 2.82 mV (rms). Increasing the space between one secondary coil and primary coil by 0.001 in. caused a balance shift of 0.636 mV (rms). This information is useful for determining tolerances for construction.

Insulating and winding techniques have been improved. Plasma-sprayed alumina is being considered for insulation on the Inconel bobbins.

(b) Tests of Model Probe-type Permanent-magnet  
Flowsensors (F. Verber)

Last Reported: ANL-7632, pp. 32-33 (Oct 1969).

The variation of sensitivity with magnet width for the Type-A flowsensors discussed in ANL-7632 is shown in Fig. I.B.1. It is clear that further increase of sensitivity beyond that shown for Flow-sensor A-4 could be achieved by increasing the width of the magnet. Also, indications are that a magnet thickness greater than that shown would increase sensitivity.

The variation of sensitivity with flux density for the same Type-A flowsensors is shown in Fig. I.B.2. As indicated, the flux density was measured above the neutral of the magnet at the surface of the 1-in.-dia tube at an electrode.

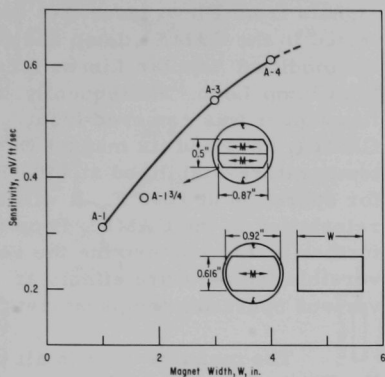


Fig. I.B.1. Variation of Sensitivity with Width of the Alnico-8 Magnets in the Type-A Flowsensors

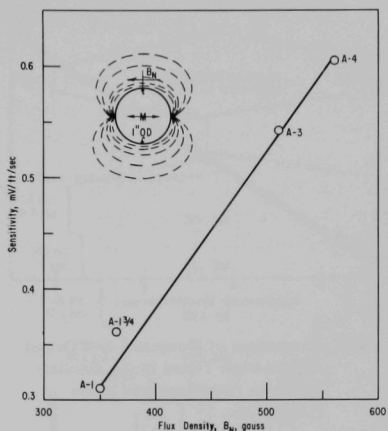


Fig. I.B.2. Variation of Sensitivity with Flux Density for the Type-A Flowsensors

Figure I.B.3 shows test data for Flowsensor A-4 operating in the CAMEL Loop at 320 and 885°F. For the maximum flow velocities in the tests, the sensitivities of Flowsensor A-4 were 0.602 mV/ft/sec at 320°F

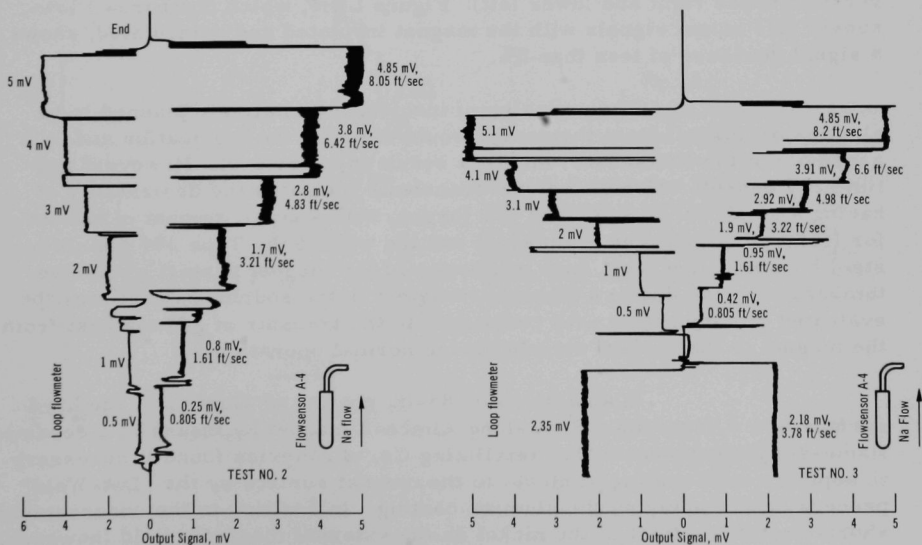


Fig. I.B.3. Tests of Permanent-magnet Flowsensor A-4 at ~320°F (left; temperature rose to ~335°F by end of test) and ~885°F (right) in 4-in. Schedule-10 Pipe Test Section of CAMEL Loop. The calculated sensitivity of the loop permanent-magnet flowmeter was 0.01485 mV/gpm, so 1.61 mV = 1 ft/sec of sodium flow through the annulus between the flowsensor and the 4-in. pipe test section.



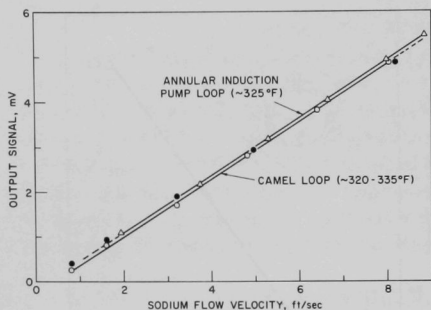


Fig. I.B.4. Comparison of Flow-sensor A-4 Output Signals when Tested in the Annular Induction Pump Loop and in the CAMEL Loop

and 0.591 mV/ft/sec at 885°F. Figure I.B.4 compares the output signals from Flow-sensor A-4 when tested in the CAMEL Loop and in the modified Annular Linear Induction Pump Loop. Subsequently, the flowsensor was removed from CAMEL Loop and its magnet was temperature-stabilized at 1300°F for operation at 1200°F. It will be reinstalled in the CAMEL Loop for further tests to determine the reversible temperature effects at various operating temperatures.

The magnets used in all the the Type-A flowsensors built and

tested to date were electrically insulated from their Type 304 stainless steel enclosures by thin sheets of mica. To determine how the output signal of a flowsensor would be affected without such insulation, Flow-sensor A-3 was cut open and its mica insulation was replaced with thin sheets of Type 304 stainless steel in a metal-to-metal push fit. Then it was retested in the modified Annular Induction Pump Loop. Figure I.B.5 shows the results for the insulated version (upper left) and for the uninsulated version (upper right and lower left). Figure I.B.6, which compares Flow-sensor A-3 output signals with the magnet insulated and uninsulated, shows a signal decrease of less than 5%.

The omission of insulation (tentatively planned to be alumina or quartz) from the design would simplify the fabrication and assembly of the flowsensor, and thus result in lower cost. However, preliminary consideration of thermal transients indicates the desirability of having a small annulus of inert gas (argon, with a small amount of helium for leaktesting) between the magnet and the wall of the Type 304 stainless steel housing. However, such protection of the magnet against excessive temperature rise due to a thermal transient in the sodium coolant must be evaluated in conjunction with resistance to the transfer of gamma heat from the magnet to the coolant stream during normal operation.

In applying a 0.085-in. coating of alumina to the hard surface of a 0.9-in.-dia x 2-in.-long Alnico-8 magnet by means of a ceramic flame-spraying process, the Metallizing Co. of America found it necessary to apply a rough coating of nickel to the magnet surface by the "Dot-Weld" process before applying the alumina coating. In addition to the unacceptable short-circuiting effect of the nickel on the external magnetic field (however, a nonmagnetic metal could be used), pieces of alumina broke away from the magnet when it was tapped with a steel bar. Thus, to obtain an alumina coating that will not disintegrate under flowsensor operating conditions, further development and testing would be required.

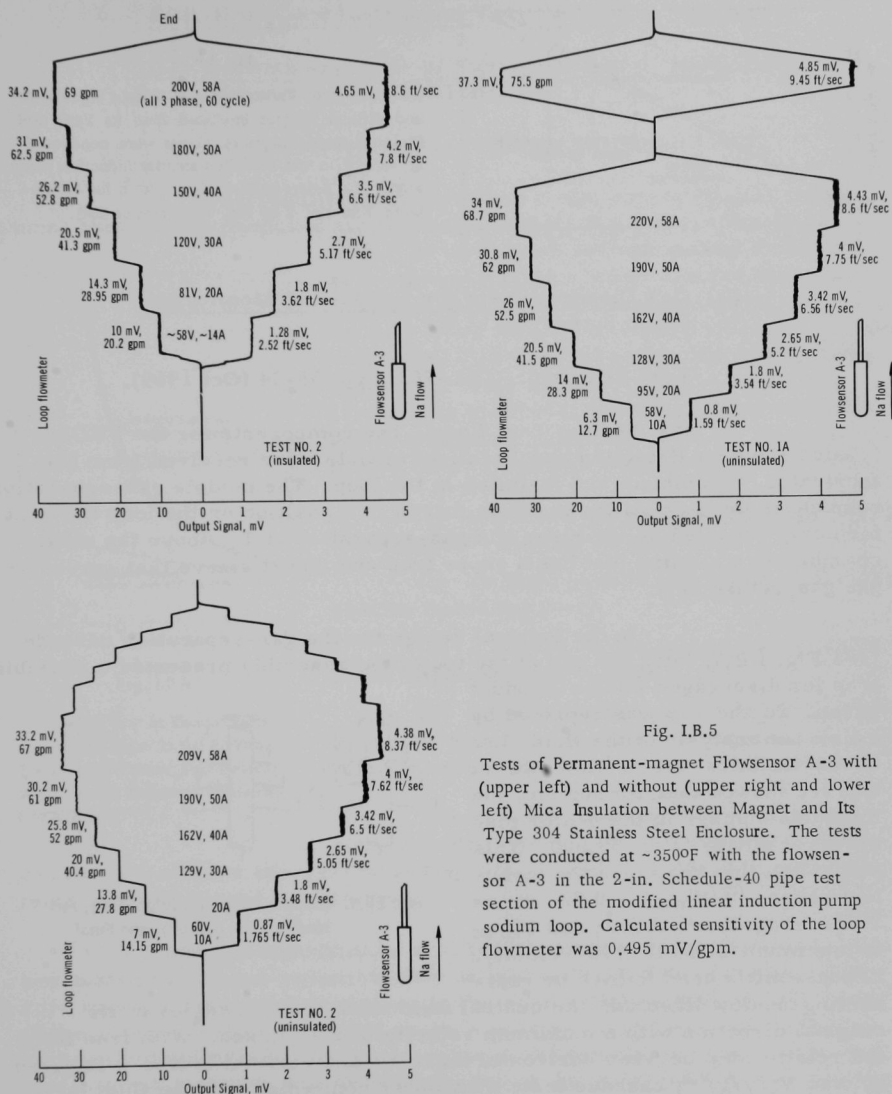


Fig. I.B.5

Tests of Permanent-magnet Flowsensor A-3 with (upper left) and without (upper right and lower left) Mica Insulation between Magnet and Its Type 304 Stainless Steel Enclosure. The tests were conducted at  $\sim 350^{\circ}\text{F}$  with the flowsensor A-3 in the 2-in. Schedule-40 pipe test section of the modified linear induction pump sodium loop. Calculated sensitivity of the loop flowmeter was 0.495 mV/gpm.

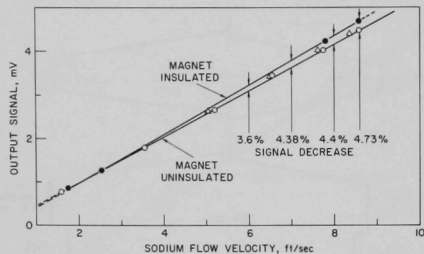


Fig. I.B.6

Comparison of Flowsensor A-3 Output Signals with and without Magnet Insulated from Its Type 304 Stainless Steel Enclosure. Tests were conducted at ~350°F in the modified annular induction pump loop. The points marked  $\Delta$  are from the uninsulated Test No. 2 of Fig. I.B.5 (lower left).

(ii) Gas Disengagement for Failed-fuel Monitoring  
(E. S. Sowa)

Last Reported: ANL-7632, pp. 33-34 (Oct 1969).

(a) Sodium Test Loop. The components for the FEDAL (Failed Element Detection and Location) module were received from the fabricator, assembled, and installed in the loop. The module gas-separation cascade is inside a utility chamber that is in a position on the loop that was formerly occupied by the riser and gas-separation unit. Above the utility chamber is a housing that has a vapor trap and insert sleeve that serves as the gas-return duct.

In the original design for the gas-separation cascade (see Fig. I.B.7, left), the cap at the top of the assembly presented a possible trap for disengaged fission-product gases. So the cap was replaced by a disk. An analysis of the fluid-flow characteristics for a flowrate of 2 ft/sec showed that, for sodium, the Reynolds number in the center pipe of the cascade was 59,500. This places the flow regime in the turbulent range:  $\bar{V}/V_{\max} = 0.82$ , where  $\bar{V}$  is average flow velocity and  $V_{\max}$  is maximum central flow velocity. Because little head is lost by re-directing the flow direction, the central fluid exits at right angles to its original direction with a maximum velocity of 2.43 ft/sec. With free fall, the relationship between horizontal travel  $x$  and vertical travel  $y$  is given by  $x = V(2y/g)^{0.5}$ ; cascade tests with water confirmed that the fluid is confined within a sheet by surface tension and travels outward in a trajectory (see Fig. I.B.7, center) such that the fluid missed the trays in the cascade. Thus the cascade was modified to the final configuration, which tests confirmed has the flow trajectory shown (see Fig. I.B.7, right).

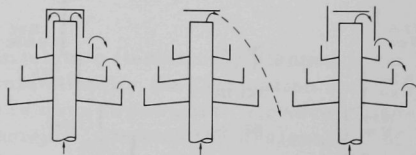


Fig. I.B.7. Cascade Original Design (left), First Modification (center), and Final Configuration (right)

b. EBR-II In-Core Instrument Test Facility (E. Hutter)

(i) Preliminary Study of Various Schemes (O. S. Seim, T. E. Sullivan, and R. C. Brubaker)

Last Reported: ANL-7606, pp. 39-40 (Aug 1969).

The results of a calculation of the rise in coolant temperatures through the proposed facility are shown in Fig. I.B.8. The figure shows the calculated rise at coolant flowrates up to approximately 1.5 gpm and for three insulating conditions. (The bottom curve, showing the rise when the gas insulating sleeve is replaced with static sodium, represents the noninsulated condition.) Only the heat transfer within the 14-in.-long portion of the facility that would be in the reactor core was considered. The calculation, which is approximate, assumed:

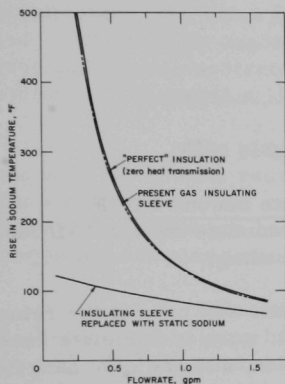


Fig. I.B.8

Calculated Rise in Temperature of Sodium Coolant in the Proposed In-core Instrument Test Facility Using Three Different Insulating Conditions

- (1) a thimble assembly of the type which will accept 19 thermocouples,
- (2) uniform gamma heating at a 62.5-MWt reactor operating level,
- (3) a sodium-temperature rise of 200°F in the adjacent subassemblies, and
- (4) an upward flowrate of 5 gpm past the labyrinth-type seal between the guide tube and the thimble assembly.

The results indicate that control of sodium temperature by flow variation is severely diminished without the gas-insulating sleeve and that the desired higher temperatures cannot be reached.

The calculations also indicate that because the test sensors are heated by gamma radiation, they should be located near the top of the core to avoid higher temperatures in the cables than in the sensors. Most of the gamma heat is generated in the structural stainless steel, which is uniformly distributed in the core region in the present concept. Since the test sensors probably will be near the top of the core, the effect of adding more structural mass in the lower portion of the core will be evaluated. Additional mass would increase heat generation and flow, thereby decreasing the degree of sensitivity required in the control valve.

Following an evaluation of several coolant-flow control valves, a flat-plate type of valve appears to be the most promising. This

valve consists of an upper and a lower circular plate with flow-control holes. The lower plate is stationary, acts as a shutter, and would be attached to the inner tube of the insulating-gas-tube assembly. The upper plate would be attached to the sensor tube. Flow control would be achieved by rotating the sensor tube, which, in turn, would rotate the upper plate with respect to the lower plate. To attain a uniform rise in coolant temperature per degree of rotation, the flow holes in the upper plate must be contoured. Flow calculations are now being developed to determine the size and shape of hole which will best provide ideal flow control.

## 2. Fuel Handling, Vessels and Internals

### a. Core Component Test Loop (CCTL) (R. A. Jaross)

Last Reported: ANL-7632, pp. 34-35 (Oct 1969).

(i) Loop Modifications to Accommodate Second FFTF Subassembly. Modifications to the CCTL to accommodate the Mark-II fuel assembly and to improve loop reliability are proceeding.

On the 2-in. pump-bypass piping that will permit the return of pump-bearing overflow sodium to the pump inlet, work is complete except for installation of 10% of the outer layer of insulation, and one pipe hanger.

For the 4-in. flowtube, the Taylor pressure-sensing elements have been delivered, along with manufacturer certification reports on calibration, dye-penetrant testing, radiographic inspection, and materials. ANL calibration is in progress.

The spool piece has been reinstalled in the CCTL test vessel with the appropriate ceramic Flexitallic gasket and a bolt-tightening schedule to ensure gasket seating to the manufacturer's recommendations. Three of the four sodium-inversion tubular heaters are installed. Four of six in-vessel thermocouples have been installed.

Quality-assurance tests continue on the dual-gate-valve assembly, bellows-seal valves, and the plugging-meter and sodium-sampling station.

A temperature test, separate from the CCTL test vessel, is underway on the dual-gate-valve assembly. At 625°F the gate valve stems indicated galling, so the gate valve stems were reduced in diameter by 0.015 in., a 0.001-in. hard-chrome plating was applied, and the original Type 304 stainless steel valve-stem bushings were replaced with soft nickel. Further tests of this assembly will be at temperatures up to 800°F.

A 2-in. Powell valve of the bellows-seal type to be used for the mechanical-pump bearing-bypass line is being prooftested. This valve has completed 100 cycles at 10 psi and 1000°F (maximum temperature recommended by manufacturer). In addition, a more severe test of 75 cycles at 125 psi has been completed in argon without bellows failure. Tests in sodium are scheduled to start soon.

A 1/2-in. NUPRO bellows-seal valve of the type to be used for the modified CCTL plugging-meter and sodium-sampling station is being prooftested. The valve has completed 100 cycles of operation at 150 psig and 1100°F with an argon atmosphere inside the valve. Sodium tests are scheduled to demonstrate that the valve can successfully contain 1100°F sodium at 150 psig for 100 cycles.

The plugging-meter and sodium-sample-station complex has been fabricated, radiographed, leaktested, and moved to the CCTL. The enclosure for this complex has been completed, and heaters and insulation for the enclosure have been installed. Electrical prooftest of the completed complex is scheduled soon.

Ultrasonic inspection of one weld of the 4-in. pump-outlet (high-pressure) piping has been completed. The area evaluated is at the weld of a 90° elbow at the inlet to a long horizontal pipe run that includes both the electromagnetic flowmeter and the flowtube in series. Defects detected ultrasonically were smaller than defects attainable for 4-in. Schedule-40 pipe as described in ASME Code, Nuclear Vessels, 1968, Section 3, Appendix 9, p. 2.18.

### C. Sodium Technology

#### 1. Sodium Chemistry

The work on sodium chemistry is directed toward the development of a sound scientific foundation for understanding the behavior of common non-metallic contaminants in sodium, for interpreting and evaluating existing corrosion data, and for predicting potential corrosion problems in sodium systems.

- a. Characterization of Oxygen- and Hydrogen-bearing Compounds in Sodium (F. A. Cafasso and M. Adams)

Last Reported: ANL-7606, p. 118 (Aug 1969).

Evidence has accumulated that suggests the involvement of transition metal-oxygen-sodium complexes in the mass transport of structural materials in sodium systems. Accordingly, the behavior of complex oxides such as sodium chromite and sodium ferrite in sodium is



of interest, and a study of their stability in sodium is being undertaken. Sodium chromite has been chosen for the initial study, and efforts to prepare this compound have started.

Preparations are also being made to find out what are the species and concentrations of oxygen- and hydrogen-bearing compounds in cold-trapped sodium. This information will be helpful in determining whether such impurities are adequately controlled by cold trapping and whether the current methods of monitoring are effective. The sodium to be analyzed will be taken from the existing Sodium Analytical Loop (SAL). At present, effort is being directed toward equipping SAL with a cold trap and a sodium-sampling device appropriate for this study. A hydrogen meter is also being installed.

## 2. Purification of Sodium

### a. Identification and Removal of Particulate Matter in Sodium (J. E. Draley)

Not previously reported.

In a newly activated program on the identification and removal of particulate matter in sodium, plans are being made to accumulate and analyze particles from EBR-II primary and secondary sodium. Preliminary to actual collection of such particles, collection methods will be developed and data will be obtained from the existing Mechanical Properties and Corrosion Loop. It is anticipated that filters will be evaluated; decisions on other collection devices have not been made.

To gain some insight as to the amount of stainless steel constituents expected to precipitate in sodium-coolant circuits by virtue of temperature differences, quasi-equilibrium calculations were made. It was assumed that equilibrium obtains between the surface of the stainless steel system and the sodium circulating in a nonisothermal loop, and that all the alloy constituents in excess of saturation at any temperature are precipitated. By using estimated solubilities for the constituents of stainless steel, a maximum of about 7 ppm precipitated solids or their metallic content was obtained for the coolest portion of an LMFBR operating between 700 and 400°C. More than 60% of the metal content of this precipitate was calculated to be iron, with the remainder about equally divided between nickel and chromium. The amount of precipitate calculated for EBR-II coolant (524 to 371°C) was about one-fourteenth that for the LMFBR, with the same compositional mix.



### 3. On-Line Monitors

#### a. Evaluation and Improvement of the Carbon-activity Meter (J. T. Holmes, C. Luner, and N. Chellew)

Last Reported: ANL-7606, p. 31 (Aug 1969).

Testing and evaluation of the United Nuclear Corporation (UNC) diffusion meter for measuring carbon activity in sodium are progressing. Experiments with an iron-membrane probe (fabricated at ANL) were conducted in a heated crucible containing 650 g of stirred sodium. To preclude changes in the carbon concentration caused by interaction of sodium with container materials, all components in contact with liquid sodium were made of copper except the probe.

As a first step, base-line carbon fluxes were measured at different temperatures. Measurable carbon fluxes were obtained at 488°C (910°F) and above. These fluxes were quite stable for 2 or 3 days, decreasing only slowly with time, probably owing to the removal of carbon from the sodium by diffusion through the probe.

The response of the probe to the introduction of a ferritic steel rod (1020 steel, 1/4-in. OD by 5 in.) into the sodium was briefly investigated. Little or no response to the ferritic steel was obtained after 1 hr at 488°C or 1 hr at 585°C (1085°F). At 630°C (1166°F), the carbon flux increased soon after immersion of the rod. The rod was removed after 30 min, and the flux levelled off and then remained constant for at least 4 hr.

The effect of adding 2 ppm carbon as  $\text{Na}_2\text{C}_2$  to the stirred sodium at 630°C was to increase the meter reading at least eightfold. The insertion of a Type 304 stainless steel rod (1/4-in. OD by 5 in.) into the melt at this point caused the carbon flux to decrease.

These experiments indicate that measurable carbon fluxes can be obtained at a considerably lower temperature than that recommended by UNC, 760°C (1400°F).<sup>\*</sup> The experiments also indicate that if a high-temperature side loop is required to obtain a measurable flux, a material other than stainless steel might be preferable. Additional experiments to evaluate construction materials for this purpose are being planned.

The Test and Evaluation Apparatus (TEA), a small, pumped, sodium loop at ANL-Illinois, will be used to test the UNC carbon meter prior to the field tests planned at EBR-II. TEA construction is complete except for fabrication of a device by which metallurgical tabs can be exposed

---

<sup>\*</sup>Caplinger, W. H., Carbon Meter for Sodium, Final Report, United Nuclear Corp. report UNC-5226 (March 1969).

to the same sodium as the probe of the carbon meter. TEA will start up after a safety review; the tab-exposure device will be incorporated after startup.

#### 4. Sampling

##### a. Sampling of Radioactive Sodium (W. Miller and P. Vilinskas)

Not previously reported.

A useful tool in the analysis of LMFBR sodium is a distillation sampler. Vacuum-evaporation of the neutron-activated sodium facilitates assay of trace elements and radioactive isotopes. Some form of the device may also prove useful as a continuous on-line monitor for detection and characterization of fission products.

Automation of the sampler is desirable for application of the device to primary sodium systems. This would require automatic means of removing the distillation cup, and of collecting and disposing of the condensate. It appears that the use of a liquid-sodium jet eductor for creating a vacuum and removing the distillate would result in a simplification of the sampler design. Preliminary discussions with the Schutte and Koerting Co. revealed the following estimates for performance of a liquid-sodium eductor: motive fluid (sodium) flowrate, 2-5 gpm; jet pressure drop, 50-100 psi; attainable vacuum with motive fluid at 300°C, less than 0.1 Torr absolute pressure. The necessary hardware for testing the application of the jet principle in distillation samplers is being procured.

#### 5. Fission Product Behavior and Control

##### a. Data-analysis Methods for Determining Fuel Failures (W. E. Miller and P. Vilinskas)

Not previously reported.

Fission gas monitors are currently in use to detect the presence of leaking fuel elements in fast reactors. A calculational study was made of the potential usefulness of this method for detecting leaks in future LMFBR power reactors. It is anticipated that such power reactors will not be shut down despite the existence of numerous fuel elements that are leaking only gaseous fission products. With vented fuels, the fuel element by definition will operate with gas leakage. What will be required in future LMFBRs is a detection system that not only takes note of a leaking fuel element, but also estimates the extent of the damage to the cladding and the likelihood of propagation of the damage to other fuel elements.

Methods of relating the cover-gas evidence of fuel failure to the severity of failure were considered. One such method relates activity ratios of short-lived gaseous fission products to the size of the leak. It was found that for fixed rates of release of the fission gases to the gas plenum in the fuel and for fixed exterior pressures, the size of a hole in the cladding might be estimated from the activity ratio of short-lived isotopes in the cover gas. However, the application of this method does not appear practical because of the variability of parameters affecting the rate of release of gas, such as location of the leak, fuel burnup, and power level.

Because of the difficulty in ascertaining the severity of a leak from analysis of the cover gas, it may be more fruitful to monitor the sodium for evidence of fuel-element failure. This will be the direction of future work.

## 6. Materials Compatibility

### a. Candidacy of Vanadium-base Alloys for Cladding LMFBR Fuels (T. F. Kassner and D. L. Smith)

Last Reported: ANL-7632, pp. 42-44 (Oct 1969).

The objective of this work is to develop enough understanding and information so that a first assessment of the adequacy of vanadium alloys as fuel cladding for LMFBR can be made.

(i) Distribution Coefficients of Impurities in Sodium-Metal Systems. Two techniques have been used to determine the solubility of oxygen in vanadium as a function of temperature. The method employed in the temperature range from 600 to 700°C was the same as that previously used for distribution coefficient measurements (see Progress Report for September 1967, ANL-7382, pp. 100-101). Vanadium wires were exposed to sodium at 600, 650, or 700°C for a sufficient time to allow oxygen to redistribute between vanadium and sodium. The oxygen concentration in vanadium increases with an increase in the oxygen concentration in sodium until an oxide film forms on the vanadium. The oxygen concentration in the core of each wire was determined after all of the oxide film was removed. The constant oxygen concentration in the core, as the oxygen concentration in the sodium was increased, was taken as the oxygen solubility in vanadium at each temperature.

Solubility measurements at temperatures below 400°C were made by the internal-friction technique. Since the height of an internal-friction peak can be related to the concentration of an interstitial element in solution in bcc metals, the technique provides a convenient method to determine the solubility of oxygen in vanadium. Oxygen was diffused into vanadium wires in a Sievert's apparatus, and the internal-friction peak was

measured. The sample was then annealed at a temperature at which a small amount of the oxygen would precipitate. After quenching the sample, the internal-friction peak was redetermined to give a measure of the concentration of oxygen remaining in solution. This value is the saturation concentration at the annealing temperature. It was possible to precipitate oxygen further or put it back into solution by annealing at lower or higher temperatures, respectively. The internal-friction technique gave similar results when oxygen was added to vanadium either by exposure to sodium or by using the Sievert's apparatus. The temperature dependence of the solubility of oxygen in vanadium is shown in Fig. I.C.1.

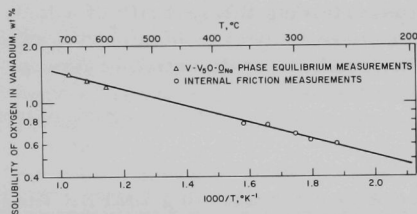


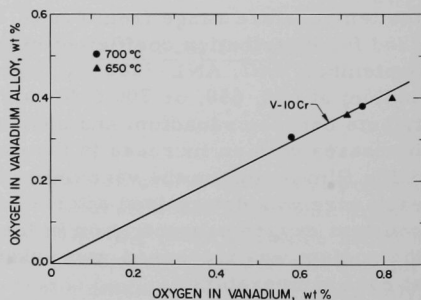
Fig. I.C.1. Temperature Dependence of Solubility of Oxygen in Vanadium

0.4, 0.6, and 0.8 ppm oxygen at 600°C. Figure I.C.2 shows some results obtained for the vanadium-10 wt % chromium alloy compared with pure vanadium. This alloy picks up only half as much oxygen as pure vanadium when exposed to the same oxygen concentration in sodium. No effect of temperature on the ratio of oxygen in vanadium to oxygen in alloy can be detected from these results. The other alloys have not yet been analyzed.

An investigation of the effect of chromium additions to vanadium on the activity and solubility of oxygen in vanadium is continuing. Alloy wires containing 10, 15, and 20 wt % chromium and pure vanadium wires have been exposed to cold-trapped sodium. Tests were conducted in sodium containing 0.4 ppm oxygen at temperatures of 550, 600, 650, and 700°C. Tests have also been completed in sodium containing

Fig. I.C.2

Oxygen Concentration in Vanadium-10 wt % Chromium vs Oxygen Concentration in Vanadium, after Simultaneous Exposure to Sodium



## D. EBR-II--Research and Development

### 1. Equipment--Fuel Related (E. Hutter)

#### a. Higher-worth Control Rod (O. S. Seim and T. Sullivan)

Last Reported: ANL-7618, pp. 23-24 (Sept 1969).

The quality-control plan for fabrication of two prototype higher-worth control rods was completed. The rods are being fabricated. The B<sub>4</sub>C pellets for these rods were received from the supplier.

Pressure-drop calculations indicated that two different arrays of B<sub>4</sub>C tubes for the absorber section of the higher-worth safety rod were acceptable: a cluster of six 5/8-in.-OD tubes and a cluster of seven 9/16-in.-OD tubes, each within the standard safety-rod hexagonal tube. The latter arrangement was chosen because it would allow a more uniform coolant-flow distribution.

A mockup of the cluster of seven 9/16-in.-OD tubes was fabricated and installed in place of the upper shield section within a standard safety-rod subassembly. Flowtests with this modified safety-rod subassembly indicated that flows were very close to the desired calculated flow. The desired calculated flow is 84 gpm at a 39-psi pressure drop; the measured flow was 83 gpm at the same pressure drop. The ends of the mockup tubes will be modified slightly to make the measured flow equal to that of the calculated flow.

### 2. Instrumented Subassemblies (E. Hutter and A. Smaardyk)

#### a. Test One and Two

##### (i) Installation (A. Smaardyk, C. Divona, W. M. Thompson, and J. Poloncsik)

Not previously reported.

The drive mechanism for raising and lowering the instrumented subassembly during fuel handling was installed during the week of Nov. 3, 1969. Installation and checkout of test 1 were completed during the week of Nov. 10. This work included flowtesting of the permanent-magnet flowmeter and subsequent severing of the extension tube from the subassembly. Installation of test 2 in the EBR-II primary tank was started the week of Nov. 17.

(ii) Assembly of Test-2 Subassembly (C. Divona)

Last Reported: ANL-7632, pp. 46-48 (Oct 1969).

During the last steps of assembling the test-2 instrumented subassembly and extension tube, the flux monitor for registering the flux during reactor operation was installed. Figure I.D.1 shows the installation of the flux monitor in relation to the reactor core. The monitor assembly consists of a 1/16-in.-dia x 5½-in.-long Reuter Stokes Model RSN-202-MI flux monitor attached to a sheathed, 0.040-in.-dia extension lead. A packing gland was used to provide a seal on the outside of the terminal box, with the extension lead protruding through the seal. The gland contains a closely fitted split seal washer and a neoprene sealant washer to provide a secondary seal should leakage of the flux-monitor tube occur; the flux-monitor tube serves as the primary seal. An expansion bellows was incorporated in the portion of the flux-monitor tube within the terminal box. This bellows allows differential expansion between the flux-monitor and extension tubes during the nonisothermal conditions existing when the extension tube is being installed in the reactor. The flux-monitor tube was installed before the subassembly was shipped to EBR-II on Nov. 7.

3. Coolant Chemistry (D. W. Cissel)

- a. Sodium Coolant Quality Monitoring and Control (W. H. Olson, C. C. Miles, T. P. Ramachandran, E. R. Ebersole, and G. O. Haroldsen)

Last Reported: ANL-7632, pp. 48-49 (Oct 1969).

(i) Radionuclides in Sodium. Table I.D.1 lists the results of analyses for  $^{137}\text{Cs}$  and  $^{131}\text{I}$  in primary sodium. The  $^{22}\text{Na}$  activity on Oct. 17, 1969, was  $4.0 \times 10^{-2} \mu\text{Ci/g}$ .

TABLE I.D.1.  $^{137}\text{Cs}$  and  $^{131}\text{I}$  in Primary Sodium<sup>a</sup>

Sample Date	Sample Size, g	Sample Flow, gpm	Flush Time, min	Sample Temperature, °F	$^{137}\text{Cs}$ $\mu\text{Ci/g} \times 10^2$	$^{131}\text{I}$ , $\mu\text{Ci/g} \times 10^4$
9/16/69	13.3	0.4	15	500	1.2	1.2
9/18/69	10.9	0.4	18	640	1.2	1.1
9/24/69	13.2	0.3	15	600	1.2	0.85
9/29/69	13.5	0.3	15	600	1.1	2.0
10/13/69	12.8	0.5	15	610	1.1	2.0
10/17/69	13.6	0.3	15	600	1.3	3.3

<sup>a</sup>All samples taken in Pyrex beaker.

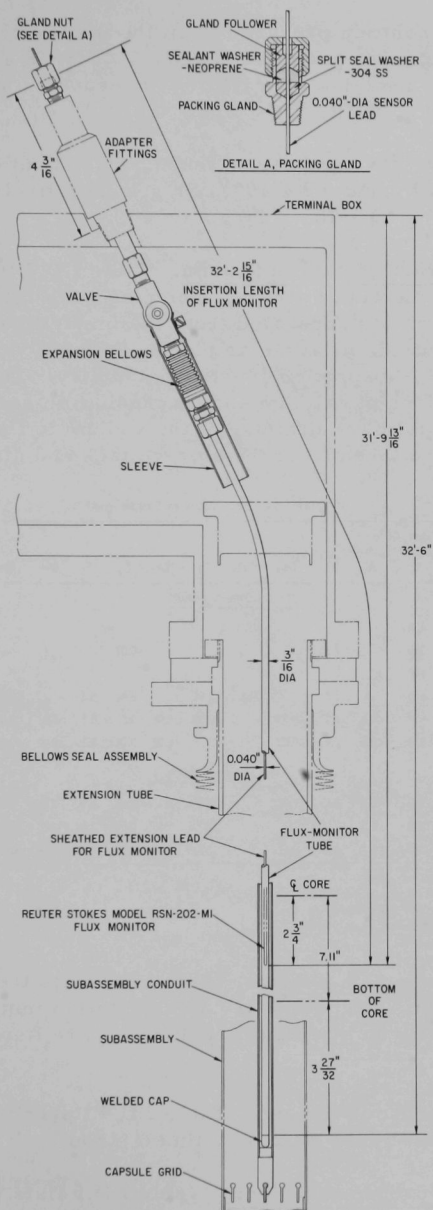


Fig. I.D.1. Flux-monitor Installation in EBR-II  
Test-2 Instrumented Subassembly



A solution prepared from the distillation residue of a primary sodium sample was gamma counted for 16 hr in a Ge(Li) gamma-ray spectrometer. The nuclides indicated by the spectrum were  $^{117m}\text{Sn}$ ,  $^{113}\text{Sn}$ ,  $^{113m}\text{In}$ ,  $^{110m}\text{Ag}$ ,  $^{54}\text{Mn}$ ,  $^{137}\text{Cs}$ , and  $^{125}\text{Sb}$ .

The  $^{24}\text{Na}$  activity of secondary sodium on Sept. 26 and Oct. 17 was  $2.4 \times 10^{-2}$  and  $9.3 \times 10^{-3} \mu\text{Ci/g}$ , respectively. Saturation activity at 50 MWt is  $\sim 3 \times 10^{-2} \mu\text{Ci/g}$ .

(ii) Trace Metals in Sodium. Table I.D.2 lists the results of analyses for trace metals in sodium. Samples were taken in various vessels, and the sodium was separated from the impurities by either solvent extraction or vacuum distillation, as noted. Impurity concentrations were measured by atomic-absorption spectrophotometry. The higher-than-normal concentrations of calcium and magnesium in secondary sodium on Oct. 29 and Nov. 2 followed draining of the sodium to the storage tank. These samples were taken from the storage tank and distilled in line.

TABLE I.D.2. Trace Metals in Sodium (ppm)

Sample Date	Sample Size, g	Sample Flow, gpm	Flush Time, min	Sample Temp, °F	Al	Bi	Ca	Cd	Co	Cr	Cu	Fe	Mg	Mn	Mo	Ni	Pb	Sn	Zn
<u>Primary Sodium</u>																			
9/11/69 <sup>a</sup>	13.5	0.5	13	480				0.025											<0.05
9/11/69 <sup>b</sup>	~10	0.3	10	350		2.1					0.03						10.6	21.2	
9/21/69 <sup>a</sup>	11.6	0.3	15	600														20.6	
9/29/69 <sup>a</sup>	12.4	0.3	15	600		1.8		0.03	<0.04		0.04	0.4		<0.01		0.07	9.8		0.06
9/29/69 <sup>c</sup>	40.5	0.3	15	650	<0.6	2.1	<0.02		<0.03	0.02	0.1	0.01	<0.005	<0.08		<0.03	8.2	20.6	
10/23/69 <sup>c</sup>	53.0	0.4	5	370	<0.6	2.4	<0.02		<0.04	0.02	0.04	0.15	0.02	<0.005	<0.1	<0.04	8.2	19.4	
<u>Secondary Sodium</u>																			
9/29/69 <sup>c</sup>	58.5	0.5	15	500	<0.6	<0.05	<0.02		<0.02	0.1	0.02	0.9	0.03	0.01	<0.06	0.1	0.5	<0.5	
10/29/69 <sup>d</sup>	~125	0.4	15	360	0.5	<0.02	1.7		<0.008	0.13	0.013	0.77	1.2	0.027	<0.016	0.14	0.76	<0.08	
11/2/69 <sup>d</sup>	~125	0.4	15	360	0.2	<0.02	0.1		<0.008	0.1	0.044	0.96	0.64	0.03	<0.016	0.12	0.7	<0.08	

<sup>a</sup>Sampled in quartz; separated by solvent extraction.

<sup>b</sup>Sampled in titanium; separated by vacuum distillation in laboratory.

<sup>c</sup>Sampled in tantalum; separated by vacuum distillation in laboratory.

<sup>d</sup>Sampled in titanium; separated by in-line vacuum distillation.

(iii) Oxygen in Sodium. Table I.D.3 lists the results of analyses for oxygen in sodium by the mercury amalgamation method. Oxygen concentrations as measured by plugging indicators are listed also for comparison.

(iv) Carbon in Sodium. Table I.D.4 lists the results of analyses for carbon in sodium by the oxyacidic flux method.

(v) Hydrogen in Sodium. Table I.D.5 lists the results of analyses for hydrogen in sodium by the isotope dilution method.

TABLE I.D.3. Oxygen in Sodium

Sample Date	Sample Container	Sample Size, g	Sample Flow, gpm	Flush Time, min	Sample Temperature, °F	Aliquot Size, g	Number of Aliquots	Average Concentration, ppm	Oxygen Equivalent of Plugging Run, <sup>a</sup> ppm
<u>Primary Sodium</u>									
9/24/69	Extrusion vessel	15	0.4	15	625	~1	4	3.0 ± 2.6	<0.5
<u>Secondary Sodium</u>									
9/17/69	Extrusion vessel	15	0.8	15	480	~1	4	9.7 ± 2.5	<0.5

<sup>a</sup>Based on solubility data from AI-AEC-12685.

TABLE I.D.4. Carbon in Sodium

Sample Date	Sample Container	Sample Size, g	Sample Flow, gpm	Flush Time, min	Sample Temperature, °F	Aliquot Size, g	Number of Aliquots	Average Concentration, ppm
<u>Primary Sodium</u>								
9/8/69	Extrusion vessel	15	0.5	10	400	~1	4	0.9 ± 0.7
9/24/69	Extrusion vessel	15	0.4	15	625	~1	3	1.0 ± 0.8
10/30/69	Extrusion vessel	15	0.3	15	320	~1	3	0.4 ± 0.15
<u>Secondary Sodium</u>								
9/17/69	Extrusion vessel	15	0.8	15	480	~1	3	1.2 ± 0.2
10/2/69	Quartz vials	~2	0.7	40	530	~1	2	2.0 ± 0.5

TABLE I.D.5. Hydrogen in Sodium

Sample Date	Concentration, ppm
<u>Primary Sodium</u>	
9/2/69	<1.0
<u>Secondary Sodium</u>	
8/29/69	<1.0

(vi) Hydrogen and Nitrogen in Cover Gas.

Table I.D.6 summarizes the concentrations of hydrogen and nitrogen in the primary and secondary argon cover-gas systems. Measurements are made with on-stream gas chromatographs.

(vii) In-line Vacuum-distillation Sodium

Sampler. A sampler designed to distill ~125 g of sodium in line has been successfully tested. Several dis-

tillation runs have been made at various heat inputs, using a stainless steel sample cup with a thermocouple in the sodium at the bottom of the cup. The time required to distill ranged from 2 to 5 hr, depending on the heat input. The ideal appeared to be 3 hr with a sodium temperature of 675-690°F. Two samples frozen in the sample cup after draining the sampler were removed without distilling. The difference in sample weight between the two was approximately 3/4%.

TABLE I.D.6. Hydrogen and Nitrogen in Primary and Secondary Argon Cover-gas Systems (ppm)

	Primary			Secondary		
	High	Low	Average	High	Low	Average
<u>October</u>						
H <sub>2</sub>	360	4	25	4	4	4
N <sub>2</sub>	7000	2600	5200	600	300	450
<u>November</u>						
H <sub>2</sub>	4	0	3	4	0	3
N <sub>2</sub>	4900	1300	3400	450	200	300

Two samples also were distilled in titanium cups and removed for analysis of trace metals. The results are included in Table I.D.2 (the secondary-sodium samples of 10/29 and 11/2).

The sampler will be tested for determination of oxygen after the secondary-sodium system has been filled and normal operation has been resumed.

#### 4. Experimental Irradiation and Testing (R. Neidner)

##### a. Experimental Irradiations

Last Reported: ANL-7632, p. 49 (Oct 1969).

Table I.D.7 shows the status of the experimental subassemblies in EBR-II as of November 15, 1969.

##### b. Operational In-cell Handling and Examination

Not previously reported.

##### (i) Examination Equipment (J. P. Bacca)

New equipment for remote interim and terminal examination of experimental irradiation capsules and elements is being planned and/or developed. The equipment being considered will be for use in making the following examinations: precision dimensional surveys (profilometry), gamma scanning, subassembly straightness and tensile testing, sampling of plenum gases from capsules, weighing, surface examination and photography (including stereoscopic), leak detection, stress-rupture testing of tubing,

TABLE I.D.7. Status of EBR-II Experimental Irradiations as of November 15, 1969 (after Run 38)

Subassembly No. and (Position)	Date Charged	Capsule Content and (Number of Capsules)	Experi- menter	Accumulated Exposure (MWd)	Estimated Goal Exposure (MWd)	Burnup <sup>a</sup>
XG03 (7D1)	7/16/65	UO <sub>2</sub> -20 wt % PuO <sub>2</sub> ( 2)	GE	24,910	28,700	6.4
XG04 (7B1)	7/16/65	UO <sub>2</sub> -20 wt % PuO <sub>2</sub> ( 2)	GE	26,106	45,000	6.7
XO18B (4E2)	10/2/69	Structural ( 3) Structural ( 2) Structural ( 1) Structural ( 1)	GE ANL ANL PNL	600	10,000	0.2 + 5.8 <sup>b</sup> = 6.0 0.2 + 5.8 <sup>b</sup> = 6.0 0.2 0.2
XO20 (6B5)	1/13/67	UO <sub>2</sub> -PuO <sub>2</sub> ( 9) (U <sub>0.8</sub> -Pu <sub>0.2</sub> )C ( 3) Structural ( 4) Structural ( 2) Graphite ( 1)	GE UNC PNL ANL PNL	16,069	20,400	6.5 7.1 4.5 4.5 4.5
XO21B (2D1)	2/23/69	Structural ( 6) Structural ( 1)	PNL PNL	16,240 7,276	23,200 9,000	3.0 + 4.1 <sup>b</sup> = 7.1 3.0
XO27 (4B3)	11/2/67	UO <sub>2</sub> -25 wt % PuO <sub>2</sub> (18) Structural ( 1)	GE PNL	13,392	16,000	7.5 5.3
XO33 <sup>c</sup> (5B4)	12/22/67	(U <sub>0.8</sub> -Pu <sub>0.2</sub> )C (19)	UNC	12,539	12,200	6.2
XO34A (2F1)	9/30/69	Structural ( 4) Structural ( 3)	ORNL ORNL	600	3,800	0.3 + 4.8 <sup>b</sup> = 5.1 0.3
XO35 (7B3)	4/13/68	Structural ( 7)	ORNL	13,184	44,800	3.0
XO36 (7E1)	7/25/68	UO <sub>2</sub> -25 wt % PuO <sub>2</sub> (19)	GE	10,790	43,300	2.8
XO38 (7C5)	5/7/68	Structural ( 7)	INC	12,766	17,700	2.7
XO40A (5B2)	9/30/69	UO <sub>2</sub> -20 wt % PuO <sub>2</sub> (18) UO <sub>2</sub> -20 wt % PuO <sub>2</sub> (16)	ANL GE	600	4,800	0.3 + 3.5 <sup>b</sup> = 3.8 0.3 + 3.6 <sup>b</sup> = 3.9
XO41 (7A3)	7/24/68	Structural ( 7)	PNL	11,226	16,700	2.4
XO43 (4D2)	2/20/69	UO <sub>2</sub> -25 wt % PuO <sub>2</sub> (37)	GE	6,506	11,000	3.5
XO44 <sup>c</sup> (7A1)	9/28/68	Oxide Insulator ( 1)	LASL	9,901	12,000	1.6
XO50 (4C2)	2/23/69	UO <sub>2</sub> -20 wt % PuO <sub>2</sub> ( 4) UO <sub>2</sub> -28 wt % PuO <sub>2</sub> ( 4) UO <sub>2</sub> -20 wt % PuO <sub>2</sub> ( 5) (U <sub>0.82</sub> -Pu <sub>0.18</sub> )C ( 2) Structural ( 4)	GE GE ORNL W GE	6,506	7,500	3.6 + 7.7 <sup>b</sup> = 11.3 3.5 3.5 3.5 2.5 + 5.3 <sup>b</sup> = 7.8
XO51 (3A2)	12/16/68	UO <sub>2</sub> -25 wt % PuO <sub>2</sub> (37)	PNL	7,051	16,400	1.4
XO54 (4E1)	3/31/69	UO <sub>2</sub> -25 wt % PuO <sub>2</sub> (37)	PNL	5,906	10,000	3.1
XO55 (6A4)	2/23/69	(U <sub>0.85</sub> -Pu <sub>0.15</sub> )C (19)	UNC	7,276	20,000	2.3
XO56 (5C2)	4/2/69	UO <sub>2</sub> -25 wt % PuO <sub>2</sub> (37)	GE	5,906	10,600	2.9
XO57 (2B1)	2/23/69	Structural ( 7)	PNL	7,276	15,000	3.0
XO58 (6F1)	4/24/69	UO <sub>2</sub> -25 wt % PuO <sub>2</sub> (37)	GE	5,330	16,000	2.0
XO59 (4A1)	4/23/69	UO <sub>2</sub> -25 wt % PuO <sub>2</sub> (37)	PNL	5,330	17,500	1.8
XO61 (7A5)	4/23/69	Structural ( 7)	INC	6,100	18,000	1.3
XO62 (6F3)	5/23/69	UO <sub>2</sub> -25 wt % PuO <sub>2</sub> (37)	GE	4,198	13,400	1.8
XO63 (7F5)	6/29/69	Magnetic Materials ( 7)	ANL	3,766	5,400	0.8
XO64 (4F2)	5/28/69	UO <sub>2</sub> -25 wt % PuO <sub>2</sub> (19)	GE	4,198	10,700	2.3
XO65A <sup>c</sup> (7E5)	10/2/69	Structural (23)	ANL	600	600	0.1 + 0.3 <sup>b</sup> = 0.4
XO69 (4F1)	10/1/69	UO <sub>2</sub> -25 wt % PuO <sub>2</sub> (37)	PNL	600	20,700	0.2

<sup>a</sup>Estimated unperturbed center burnup accumulated on peak rod (fuels, at. %, nonfuels, nvt x 10<sup>-22</sup>).<sup>b</sup>Previous exposure from another subassembly.<sup>c</sup>Subassemblies XO33, XO44, and XO65A are scheduled for removal before Run-39 startup.

sodium-bond and sodium-level testing, and neutron radiography. In addition, remotely operated equipment is being considered for the following operations: deencapsulation and reencapsulation, metallographic-sample cutting, milling, and correction of defects in capsule sodium bonds observed during interim examinations.

Some of the equipment for accomplishing the above functions has been received at the Fuel Cycle Facility and are either being checked out or modified for in-cell installation. Other equipment is being designed or will be proposed for design and development.

## 5. Materials-Coolant Compatibility (D. W. Cissel)

### a. Evaluation and Surveillance of EBR-II Materials

Last Reported: ANL-7618, pp. 35-36 (Sept 1969).

#### (i) Oxidation of Bi-Sn Alloy (W. E. Ruther)

The factors influencing the rate of dross formation in the fusible seal of the EBR-II reactor were studied in the laboratory, using a rotating cylinder in a beaker of the fusible alloy Bi-42 wt % Sn.

This brief investigation indicated that dross formation in a simple rotating system may be a complex process. A single, linear oxidation rate was found in only those few experiments in which the oxidation product did not mechanically interact with the rotor.

In the more general case, the mechanical interaction of the dross with the rotating system resulted in substantially greater oxidation rates after an induction period. The oxidation rate during the induction period was shown to be related linearly to the circumferential velocity of the rotor in the range of velocities of interest in the EBR-II (0 to 100 in./min) and to be independent of the rotor size. The very small effect of temperature (between 160 and 200°C) during this induction period suggested that the influence of temperature on the chemical reaction is quite small for the range of interest to the reactor.

The secondary oxidation rate, reached after about 600 min, was related linearly to velocity for a given rotor, but was dependent on rotor size. The dross mechanically milled into the initially submerged rotor surfaces permitted access of oxygen to a much larger interface between liquid metal and air. Insufficient data were obtained to establish the relationship between the physical dimensions of the submerged rotor and the secondary oxidation rate. However, a single set of data at 200°C indicated an approximately proportional relationship between the secondary oxidation rate

at constant velocity and the vertical submerged area of the two rotors. This sort of relationship logically might be expected from the physical appearance of the oxidized melt.

The duration of the induction period was related inversely to the degree of wetting of the rotor by the liquid metal. It is suggested that the poorer bond between the solid and liquid resulted in more slippage at the interface and less mechanical force being transmitted to the liquid metal. As a consequence, less shearing was required in the liquid metal, and less tearing of the protective oxide film occurred.

No large effect of melt composition on the secondary oxidation rate was found for variations in tin content between 37 and 47 wt % or for addition of aluminum. Indium in a concentration of 4 wt % proved to be effective in reducing the rate at which the basic alloy formed dross. However, there was very little benefit derived from the indium addition when sodium (at the level found in the actual seal trough) was added to the alloy containing 4 wt % indium.

(ii) Examination of Overheated Primary-sodium Sampler  
(T. D. Claar)

On Aug. 6, 1969, the heater circuits on the EBR-II primary-sodium sampler were found to be energized. Apparently, the heaters had been left on after the sampling operation on Aug. 1. Since the overflow sampler had been heated to a temperature above 1000°F (the upper limit of the temperature indicator), it was removed from the system and examined.

The results of metallographic examination of three sections of the sampler follow:

(a) Type 316 Stainless Steel Swagelok Fitting. In the as-polished condition a thin oxide coating was present at the outer surface (air side); below this oxide, a subsurface reaction layer also was seen. Oxalic acid etching revealed that this layer contained nitride precipitates that were very similar to the nitrides formed in Type 304 stainless steel foils during exposure to nitrogen at 1020°F for one week.

The inner surface (sodium side) also contained a reaction layer. The ID appeared to have undergone nitridation and oxidation, although the oxidation effect was masked by the heavy nitrides present in the layer.

Etching of the section in boiling potassium ferricyanide solution showed that no sigma phase had nucleated during the overheating period.

(b) Type 304 Stainless Steel Tubing. The outer surface of the tubing exhibited an atmospheric oxidation product which penetrated intergranularly to a depth of ~0.8 mil in some areas. The inner surface suffered some degree of intergranular oxidation. The loss of grains due to this penetration caused a general surface-roughening effect; however, the maximum depth of penetration on the inner surface was less than 1 mil.

Both the Type 316 and Type 304 stainless steel components exhibited grain-boundary carbide precipitates, indicating that the materials had been heated within their sensitization-temperature ranges.

(c) Type 304L Stainless Steel Sodium-level Detector. This detector had been partially immersed in sodium while the remaining portion had been exposed to argon above the sodium level. The segment exposed to sodium was heavily oxidized to a depth of 1 mil. The section in the argon space exhibited slight intergranular oxidation less than 0.1 mil deep in isolated areas.

The maximum temperature of the sampler during the overheating cannot be determined accurately. Study of the phases present in the stainless steels indicates a temperature within the broad range of 1000-1650°F.

The interactions of the stainless steels with their environments (air and sodium) and the heating effects were not great enough to cause doubt as to the safe operation of the sampler in the future.

(iii) Examination of EBR-II Neutron Source (Tantalum-clad Antimony Source SO-1915) (R. V. Strain, V. G. Eschen, and D. M. Cheney)

Preliminary results have been obtained from the postirradiation examination of EBR-II neutron source SO-1915. This source had been in the reactor (in Row 7) since initial startup and had accumulated a calculated maximum total fluence of approximately  $4 \times 10^{22}$  nvt. Postirradiation examination included measuring the diameter of the source, and performing metallographic analyses and density determinations with samples of the tantalum cladding of the source.

Table I.D.8 compares the diameters of the irradiated source with those of an unirradiated control source fabricated from the same lot of tantalum tubing. These data indicate that an increase in diameter occurred as a result of irradiation. These initial measurements were made with a micrometer; more accurate measurements will be made soon.



TABLE I.D.8. Diameters (in.) of Irradiated Source SO-1915 and Unirradiated Control Source

	Distance from Top (in.)					
	1	4	8	10	13	15
SO-1915	0.930	0.924	0.919	0.920	0.922	0.922
Control	0.915	0.914	0.914	0.914	0.914	0.914

Table I.D.9 compares the densities of samples of the irradiated and the unirradiated cladding. These data indicate that irradiation swelling of ~4 vol % occurred near the midlength and bottom regions of the

TABLE I.D.9. Densities (g/cc) of Samples of Tantalum Cladding from Irradiated Source SO-1915 and Unirradiated Control Source

	Sample Location		
	Top	Midlength	Bottom
SO-1915	16.5	16.0	16.0
Control	16.67	16.69	16.68

irradiated source. The density determinations were made by the immersion technique, using  $\text{CCl}_4$ . The samples from SO-1915 were very small; larger samples will be run to improve the accuracy of the determinations.

Metallographic examination of samples from the top, middle, and bottom of the irradiated source revealed no evidence of corrosion at

either the OD or the ID surfaces of the tubing. The grain size varied considerably from sample to sample, being smallest at the bottom region and largest near the top end. Whether these variations occurred during fabrication or resulted from irradiation has not been determined. Table I.D.10 compares the microhardnesses of samples of the irradiated and unirradiated cladding. These measurements show that considerable irradiation hardening occurred in the tantalum material. A microhardness traverse ranging from the outside diameter to the inside diameter of the tubing showed no hardness differences. The measurements were taken in about 0.005-in. increments starting within 0.003 in. of the two surfaces.

TABLE I.D.10. Microhardnesses<sup>a</sup> of Samples of Tantalum Cladding from Irradiated Source SO-1915 and Unirradiated Control Source

	Sample Location		
	Top	Midlength	Bottom
SO-1915	217	302	311
Control	98.3	82.1	78.0

<sup>a</sup>Average Diamond Pyramid hardness values.

b. Examination of Materials from EBR-II Surveillance Subassemblies (S. Greenberg)

Last Reported: ANL-7618, p. 36 (Sept 1969).

The graphite-containing cans from SURV-2 have been cut open, and the density of the graphite determined. Table I.D.11 gives the

results. The temperature during irradiation was approximately 370°C. Metallography of the stainless steel is in progress.

TABLE I.D.11. Effect of Reactor Exposure on Density of Graphite in SURV-2

Type of Graphite	Density (g/cm <sup>3</sup> )	
	Before Exposure	After Exposure
Plain	1.5419-1.6376 <sup>a</sup>	1.6933
Borated	1.5601	1.5639

<sup>a</sup>Range for six lots.

It is obvious that there has been no swelling since an increase in density was observed. An increase in density at approximately  $4 \times 10^{21}$  nvt is not altogether unexpected.\*,\*\*

The thickness of the carburized zone on the interior of the cans was similar in general to that after the SURV-1 exposure, i.e., ~0.03 to 0.04 mm. However, in contrast with SURV-1, in which all graphite was easily removable from the cans, some sticking occurred in SURV-2. Additional examination is in progress to determine if there had been a reaction between the graphite and stainless steel.

Tensile samples have been prepared from the can material.

c. Effect of Interstitial Elements in EBR-II Sodium (W. E. Ruther)

Last Reported: ANL-7618, p. 37 (Sept 1969).

A set of refractory metal wires including V, Nb, and V-Cr alloys were exposed to the primary coolant during the 62.5-MWt EBR-II run. All wires, including those of pure vanadium, appear to have survived the exposure. They are being prepared for evaluation of interstitial content by internal friction techniques.

d. LMFBR Materials Evaluations (W. E. Ruther)

Last Reported: ANL-7606, p. 47 (Aug 1969).

The design of the Mark-K1 high-temperature subassembly for materials exposure has been completed. The design outlet-sodium temperature is 1250°F for 50-MWt operation. It is estimated that the outlet-sodium temperature would be ~100°F higher under 62.5-MWt operating conditions.

\*Industrial Graphite Engineering Handbook, Union Carbide Co., Ch. 6, "Nuclear Graphite" (June 1961).

\*\*Reynolds, W. N., "Physical Properties of Graphite," Ch. 7, Elsevier Publ. Co., Amsterdam (1968).

## 6. Systems Engineering (B. C. Cerutti)

### a. Surveillance, Evaluation and Studies of Systems

Last Reported: ANL-7632, pp. 49, 51-52 (Oct 1969).

#### (i) Surveillance and Evaluation of EBR-II Flow-monitoring System (R. O. Haroldsen)

A study of the numerous flow monitors in the EBR-II shutdown circuit was initiated to determine if the flow-monitoring system could be simplified without compromising reactor safety. The study includes some computer analysis of reactor temperature transients following simultaneous failure of both primary coolant pumps as well as other considerations.

### b. Plant Improvements

Not previously reported under this heading.

#### (i) Rotating-plug Seal-cleaning System (L. P. Cooper)

The new freeze-seal temperature-control system was installed during the reactor shutdown.

The blade thermocouples of the large and small plugs (12 and 8, respectively) were removed and replaced with ungrounded iron-constantan thermocouples. These thermocouples were accurately positioned vertically by Swagelok fittings.

The in-plug controller, the control cabinet for the small plug, and the ammeter and alarm panel were removed, as were the extension leads for the thermocouples in the troughs of the large and small plugs. The rewiring associated with this modification was done simultaneously with equipment removal.

The original 0.9X Variac was removed and replaced by new Variacs for the lower heaters of the large and small plugs, making the seal-heating systems of the two plugs independent of each other. The lower-heater sections of the small plug were relocated by a minor rewiring change. The temperature-control cabinets for the large and small plugs and the ammeter cabinet for the seal heater were installed. The cabinets then were wired in place. Thirteen faulty blade heaters were located; the necessary repairs were made to place these heaters back into operation.

Checkout was completed for rewiring changes in motor control center R-4 and for the two Variacs which had been installed. The

control and alarm functions of the temperature-control system were checked and found satisfactory. The freeze seals were melted, and power to the seal heaters was adjusted.

The remaining work consists of checking the heaters, adjusting the heater sections to equalize heat distribution, and monitoring the controller operation.

(ii) Installation of Instrumented Subassembly (J. B. Waldo)

The instrumented-subassembly drive system and the test-1 subassembly were installed in control-rod position No. 6 after the existing control-rod drive and its associated equipment had been removed. Since the control-rod drive was still usable, it was sealed in a specially designed storage tube pressurized with argon. This storage procedure will allow reuse of the drive without disassembly for cleaning.

Six control-rod drives were partially disassembled to allow access to the central support column. An extension column, used to support the instrumented-subassembly elevation drive, then was installed along with the bellows-support structure and other auxiliary equipment. The control-rod drives were reassembled after the installation had been completed.

Circuit and operational checkout of the instrumented subassembly was performed, first using a temporary control cabinet. When operation was shown to be satisfactory, the subassembly was connected to the fuel-handling console, and complete interlock and circuit checkouts were performed in fuel-handling sequences A and H. After the checkouts, the primary pumps were started to allow monitoring of the temperature and flow-readout instrumentation of the subassembly. This completed the testing of the subassembly.

Next, the gripper that secured the extension tube to the subassembly was removed by using the pulling pipe. The lead-cutting tool and drive were installed, and the leads were severed without difficulty. The extension tube and the cutoff tool were removed as an assembly, using the pulling pipe. Separation of the extension tube from the subassembly was very smooth. The subassembly was removed from the reactor, using the normal fuel-handling equipment, and transferred to the temporary coffin.

The test-2 instrumented subassembly was transferred from its shipping container to a storage hole, where all final checks were performed. The subassembly then was installed in the preheater and heated to approximately 620°F. Test 2 was next installed in the primary tank, and final assembly is in progress.

## 7. Leak Detection and Location--Xenon Method (R. E. Rice)

Last Reported: ANL-7618, pp. 40-43 (Sept 1969).

### a. Status of Xenon Tags (P. B. Henault and W. J. Larson)

The anticipated requirements for xenon tags for the next three years have been forecast. Figure I.D.2 summarizes the present status and predicted needs. Thirty-nine different tags may be required at one period sometime during the next three years, probably not until early in CY 1972. After that period, tags now in use will be removed from service as certain subassemblies complete their irradiations, and new tags with the same xenon ratios as in those subassemblies may be used in subassemblies being inserted into the reactor for the first time.

Eighteen unique tags have been prepared, and seven of these are in use or have been designated for use. The 11 remaining tags should fill the needs of EBR-II through July 1970. These tags were prepared in three separate batches, arbitrarily designated the A1, A2, and A3 series. Each batch consists of natural xenon and an isotopically enriched xenon made by Mound Laboratory. Enrichment has been differentiated by the concentration of the lightest isotope,  $^{124}\text{Xe}$ . The A1 series was blended from a nominal 12%-enriched xenon, the A2 from 6%, and the A3 from 1%.

Tables I.D.12, I.D.13, and I.D.14 show the isotopic compositions of the first three series of tags. Also shown is the ratio of  $^{129}\text{Xe}$  to  $^{124}\text{Xe}$  concentrations, a convenient means for identifying each specific tag. Other ratios could be used, but  $^{124}\text{Xe}$  and  $^{129}\text{Xe}$  are among those isotopes least influenced by fission yield and burnup.

TABLE I.D.12. Isotopic Composition  
of A1 Series of Xenon Tags

Xenon Isotope	Isotopic Composition (vol %)				
	Tag 1	Tag 2	Tag 3	Tag 4	Tag 5
124	12.10	8.95	5.82	4.45	1.99
126	4.80	3.27	2.37	1.81	0.85
128	16.70	12.20	9.11	7.31	4.29
129	58.78	47.90	42.46	38.78	31.72
130	2.25	2.81	3.22	3.48	3.85
131	3.13	8.80	12.35	14.30	18.15
132	1.70	9.48	14.50	17.70	22.91
134	0.29	3.53	5.52	6.75	8.72
<u>136</u>	<u>0.25</u>	<u>3.06</u>	<u>4.65</u>	<u>5.42</u>	<u>7.52</u>
129/124 Ratio	4.86	5.35	7.30	8.72	15.94



TABLE I.D.13. Isotopic Composition of A2 Series of Xenon Tags

Xenon Isotope	Isotopic Composition (vol %)							
	Tag 1	Tag 2	Tag 3	Tag 4	Tag 5	Tag 6	Tag 7	Tag 8
124	5.58	3.80	2.58	2.08	1.48	1.19	0.91	0.72
126	1.92	1.31	0.90	0.73	0.55	0.44	0.35	0.30
128	10.32	7.61	5.75	4.83	3.99	3.47	3.11	2.85
129	63.02	51.9	44.0	39.9	36.2	34.0	32.1	30.8
130	4.32	4.13	4.16	4.04	4.05	3.96	4.03	4.01
131	9.43	13.1	15.6	16.9	18.0	18.8	19.4	19.7
132	5.03	11.8	16.6	19.1	21.1	22.5	23.5	24.3
134	0.34	3.57	5.68	6.83	7.88	8.43	9.00	9.33
136	0.026	2.75	4.80	5.68	6.65	7.17	7.69	7.97
129/124 Ratio	11.29	13.66	17.05	19.18	22.91	28.57	35.27	42.78

TABLE I.D.14. Isotopic Composition of A3 Series of Xenon Tags

Xenon Isotope	Isotopic Composition (vol %)				
	Tag 1	Tag 2	Tag 3	Tag 4	Tag 5
124	1.257	0.957	0.779	0.641	0.535
126	0.834	0.646	0.528	0.440	0.369
128	8.02	6.46	5.55	5.10	4.25
129	63.50	53.86	48.26	43.81	40.33
130	5.25	4.94	4.77	4.62	4.53
131	13.11	15.20	16.40	17.32	18.16
132	7.46	12.51	15.44	17.66	19.60
134	0.496	3.08	4.60	5.72	6.65
136	0.080	2.35	3.68	4.69	5.59
129/124 Ratio	50.52	56.28	61.95	68.35	75.38

Table I.D.15 lists those specific tags which have been designated for use or are already in use. The subassemblies noted in the table correspond to the dotted lines in Fig. I.D.2.

TABLE I.D.15. Xenon Tags Now in Use or Designated for Use in EBR-II

Tag Designation <sup>a</sup> (Series/Tag No.)	Experimenter	No. of Experiment or Subassembly	Date Put into Core
A1/2	Battelle	XO73	12/69
A1/3	Battelle	XO74	12/69
A1/5	Argonne	XX01	11/69
A2/1	GE	XO58	4/24/69
A2/3	GE	F-11A	Open
A2/7	Battelle	PNL-17	Open
A3/1	Battelle	XO69	10/1/69

<sup>a</sup>Refers to series designation and tag number in Tables I.D.12 through I.D.14.



Efforts to increase the number of tags available are proceeding in three directions:

(1) Development of a B Series of Tags. Inasmuch as  $^{128}\text{Xe}$  could be produced from the thermal-pile irradiation of  $^{127}\text{I}$ , an early proposal was made to blend  $^{128}\text{Xe}$  with varying mixtures of enriched xenon from Mound Laboratory. These mixtures, termed the B series, if blended with the same conservatism as the A series, would provide about the same number of tags as the A series. A purchase order for the development of a manufacturing process for  $^{128}\text{Xe}$  recently has been issued to Douglas United Nuclear, Inc. Development is expected to be completed in six months. The purchase order also includes the option to produce a 1-liter pilot quantity of  $^{128}\text{Xe}$ .

(2) Development of a C Series of Tags. Quantities of Mound Laboratory xenon enriched in  $^{124}\text{Xe}$  to 5% (720 cc) and 20% (480 cc) were purchased. Calculations indicate that the greatest number of additional tags can be prepared by blending this xenon with "1%" Mound Laboratory xenon. These tags will be termed the C series. Approximately 30 tags should be available from this series.

The Idaho Facilities chemical analytical laboratory is preparing equipment for the blending of this series. The first C-series tags are expected to be blended in Jan 1970. The same apparatus will be used for blending the B series when  $^{128}\text{Xe}$  becomes available.

(3) Refinement of Recovery and Identification Capabilities. The total number of unique tags available from the A, B, and C series is conservatively estimated to be of the order of 60 to 70. However, calculations based on more realistic limits and anticipated efficiencies of the tag-sampling system, charcoal trap, mass spectrometer, etc. put the total possible number of available tags from these three series at several hundred. Efforts are being made to refine the present techniques and establish limits for important variables where possible. These efforts include:

- a) experiments to determine xenon solubility and entrapment in the primary coolant,
- b) experiments to determine the effects of irradiation on tag ratios,
- c) increasing of the sensitivity of the mass spectrometer to the ultimate limit,
- d) provision of the capability to conduct the best possible calibration of the mass spectrometer, and
- e) study of the feasibility of better tag-injection techniques.

b. Xenon-tag-sampling System (C. W. Wilkes)

Drawings and specifications for the xenon-tag-sampling system have been completed, and the components are being fabricated and installed. This system will utilize a charcoal-bed cold trap to concentrate the fission-product xenon isotopes for analysis by a mass spectrometer.

c. Increased-capacity Purging System for Primary Cover Gas  
(C. L. Livengood)

Preliminary design of a higher-capacity system for purging the primary-tank cover gas has been started. The objective of this system is to permit purging of a xenon tag from the primary-tank cover gas within 12 hr after a subassembly containing a leaking fuel element or capsule has been removed from the reactor.

## 8. Reactor Analysis, Testing and Methods Development

Last Reported: ANL-7632, pp. 52-65 (Oct 1969).

### a. Nuclear and Thermal Analyses

#### (i) BEMOD Calculations of a Row-7 Blanket Fuel Pin (J. F. Koenig, C. C. Ford, and C. M. Walter)

The BEMOD computer program was used to determine the characteristics of a blanket fuel pin during irradiation in reactor Row 7 of EBR-II. Calculations were made for the hot pin adjacent to the core with the reactor operating at 50 and at 62.5 MWt. The study was conducted to determine the feasibility of increasing the irradiation beyond the current burnup limit of 0.27 at. %. The results of the calculations indicate that the burnup could be increased to 0.5 at. %.

For an unirradiated blanket fuel pin, fuel expansion of 11% can be accommodated before the fuel contacts the cladding. Since the volume of cold sodium is about double the initial volume of gas in the element, there is a possibility of developing high gas pressures if swelling of the fuel and thermal expansion of the sodium cause displacement of sufficient sodium to the space normally occupied by the gas.

The blanket fuel-swelling characteristics were based on PNL studies\* of fuel with similar composition. The temperature dependence is given by the following equation, with a maximum swelling of 120% per percent of burnup occurring at 895°F:

$$\Delta V/V = \frac{\% \text{ burnup} (1.2^{-1.21 \times 10^{-4} \Delta T^2})}{1 + (P/250)(1 - 0.75 \times 10^{-4} \Delta T^2)}$$

where P is the larger of the plenum pressure or the fuel-cladding contact pressure in psi, and  $\Delta T$  is the difference between 895°F and the average fuel temperature in °F. It was assumed that the fuel was compressible and that a pressure of 1000 psi would compress the swelling 80% at the maximum fuel-swelling temperature. The initial calculation, reported in ANL-7632, indicated that the maximum fuel swelling occurred higher in the pin than did the maximum measured swelling. Therefore, the maximum fuel-swelling temperature was reduced from 995 to 895°F to bring the measured and calculated swelling into agreement. For the 62.5-MWt heat rating, the maximum swelling temperature occurs at the axial flux peak. This calculation should represent the worst fuel-swelling condition.

A subassembly power generation of 114 kW was used for a 7N4 position. This corresponds to an exposure of 12,000 MWd at a maximum

\*Leggett, R. D., et al., Basic Swelling Studies, BNWL-SA-154 (Sept. 19, 1965).

burnup of 0.27 at. %, which is representative of current Row-7 exposure limits. Due to the radial flux profile, the hot pin in the subassembly would generate 42% more heat than the average. This corresponds to 8500 W/pin, or 5700 Btu/hr-ft. If the 22.2-gpm subassembly flow is assumed to distribute itself uniformly in the subassembly, the coolant adjacent to the hot pin would reach 892°F. The heat rating, coolant-temperature rise, and neutron flux for 50-MWt operation were increased by 25% to determine blanket-pin swelling characteristics at 62.5 MWt. The swelling of the annealed Type 304 stainless steel cladding which is caused by neutron fluence was predicted by the following equation:\*

$$\Delta V/V = 4.9 \times 10^{-49} (\phi t)^{1.71} 10^{\left( \frac{1.55 \times 10^4}{T} - \frac{5.99 \times 10^6}{T^2} \right)},$$

where  $\Delta V/V$  is the cladding swelling in percent and  $T$  is the temperature in °K. For the blanket pin, BEMOD calculates that most of the cladding swelling is due to neutron fluence.

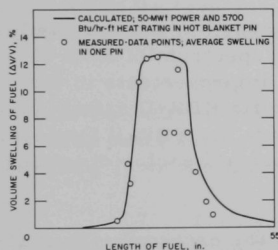


Fig. I.D.3. Calculated and Measured Swelling of Fuel in an EBR-II Blanket Subassembly

The BEMOD calculations indicate that the fuel expands rather rapidly and would be in contact with the cladding at ~0.15-at. % burnup. Once contact is made, the fuel is compressed and its rate of growth reduced. The contact pressure is much greater than the plenum pressure and will cause the cladding to creep. The calculated fuel swelling at the current burnup limit (0.27 at. %) is shown in Fig. I.D.3, which also shows the average measured fuel swelling at this burnup. The agreement between the two indicates that the fuel-swelling model is acceptable, and, therefore, the calculated gas pressure in the pin should be representative of the actual pin pressure.

The maximum calculated burnups at 2% maximum cladding growth are summarized in Table I.D.16. The maximum cladding growth during burnup is shown in Fig. I.D.4. At 0.27-at. % burnup, 95% of the calculated cladding growth is due to neutron fluence. At 2% total growth, ~75% of the growth is due to neutron fluence. The remainder of the growth originates primarily from fuel-cladding contact pressure, which reaches a maximum value of 1000 psi. The buildup of pressure in the gas plenum is

TABLE I.D.16. Maximum Blanket-pin Burnup at 2% Cladding Growth

Condition	Maximum Burnup (at. %)	Irradiation Time (MWd)
<u>50 MWt</u>		
5700 Btu/hr-ft	0.536	24,000
<u>62.5 MWt</u>		
7100 Btu/hr-ft	0.530	23,900

\*Claudson, T., PNL, private communication.

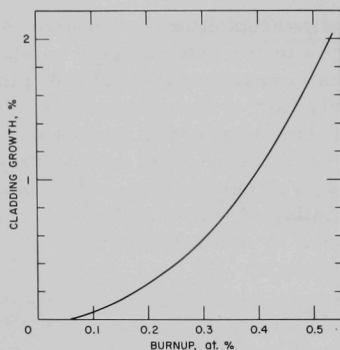


Fig. 1.D.4. Calculated Maximum Growth in Cladding vs Burnup in Blanket Subassembly

negligible, rising to a maximum value of only 200 psi. The cladding growth and resultant creep are controlled by the fuel-cladding contact pressure rather than the plenum pressure. The maximum burnup at 2% cladding growth is essentially unaffected by the allowable variation in the initial sodium level.

The results of these calculations indicate that the burnup limit can be increased to ~0.5 at. %, which corresponds to 2% cladding growth. When this growth is reached, the spacing between subassemblies will be reduced to the point where the subassemblies will have to be replaced.

#### b. EBR-II Reactor Safety Surveillance (A. V. Campise)

The AIROS dynamic-simulation digital code has proved highly effective in providing analytical solutions to a wide spectrum of EBR-II dynamic-response and safety problems. Proposed improvements in the existing AIROS code will adapt the program to specific EBR-II safety questions. The modified AIROS program will provide the EBR-II Project with an excellent means of simulating various abnormal reactor operating conditions.

The dynamic-simulation model couples the neutronic-thermal-hydraulic effects inherent in the EBR-II core in a closed-loop reactivity-feedback system to analyze experimental rod-drop data. If only the effects of fuel axial expansion and sodium density are used, the rod-drop data over the first 40 sec of experiment recording time can be reproduced qualitatively (time response) and quantitatively (magnitude of reactivity feedback). By assuming a value for one parameter (variable positive bowing coefficient) and using predicted negative feedbacks that are independent of power level at full flow, rod-drop data acquired for stainless steel-reflected cores can be shown to agree with this assumed model. The semiquantitative results obtained agree with the results of other types of measurements made during the time the EBR-II was loaded with a stainless steel reflector. The following conclusions come from the application of this model.

1. The prompt-feedback network in EBR-II through Runs 36A is composed principally of effects caused by axial expansion of fuel and by changes in sodium density.

2. Positive bowing from the stainless steel reflector was present in cores in Runs 26B through 29A.

3. At low powers (<12.5 MWt) and with a stainless steel reflector, there was no thermal bowing. Under those conditions, the basic dynamic model using only computed negative temperature coefficients gave excellent results with rod-drop data.

4. If a  $\pm 5\%$  uncertainty in the reactivity worth of the stainless steel drop rod is assumed, the following variations could be made in the system parameters without exceeding the uncertainties of the experimental data:

- a.  $\pm 18.6\%$  variation in the sodium-temperature coefficient;
- b.  $\pm 15.4\%$  variation in the fuel-temperature coefficient;
- c.  $\pm 9.8\%$  variation in the primary-coolant flow;
- d.  $\pm 8.3\%$  variation in the reactor power.

5. The reactivity feedbacks in the radial blanket can be assumed to be zero and still not affect the comparison of theoretical versus experimental rod-drop data.

6. There are definitely reactivity feedbacks from changes in sodium-coolant temperature and from the effects of fuel expansion in the rod-drop data; zeroing out these effects would cause the model to deviate markedly from the experimental measurements.

7. The dynamic-simulation model can be used in analyzing the transient response of EBR-II irradiation cores.

c. Analysis of Subassembly Bowing (D. Mohr and L. K. Chang)

The specific differential equation for unrestrained thermal deflection in BOW-V has been identical to the equation used in all previous ANL bowing programs. This equation can be written as

$$\frac{d^2y}{dz^2} = \frac{-M_T(z)}{I_z \epsilon} = \frac{C \alpha \Delta T(z)}{D},$$

where

y = material displacement of subassembly;

z = axial location along subassembly centerline;

$M_T(z)$  = thermal moment;

$I_z$  = moment of inertia;

$\epsilon$  = Young's modulus;

$C$  = a constant dependent on temperature distribution along the periphery of the hexagonal can;

$\alpha$  = linear coefficient of thermal expansion;

$\Delta T(z)$  = temperature difference across flats of hexagonal can as function of  $z$ ;

$D$  = equivalent outside diameter of the hexagonal can.

The value of  $C$  is significant in BOW-V analysis. Up to the present time,  $C$  has been assumed equal to unity, which is true for the case of a solid rectangular bar in which the temperature distribution varies linearly from side to side. Use of unity for  $C$ , however, was questioned because:

1. hexagonal-can geometry is poorly approximated by a rectangular cross section,
2. detailed temperature calculations for EBR-II subassemblies show that temperature distribution, in general, is not linear, and
3. the hexagonal can, which is assumed to contribute over 95% of the total subassembly rigidity, is hollow.

Analysis of  $M_T(z)$  and  $I_z$  for a hollow hexagonal can with arbitrary temperature distribution along the periphery\* showed:

1. the maximum variation in  $C$  is about 0.6 to 1.25 due to temperature distribution;
2. the actual temperature distributions in EBR-II suggest a  $C$  of 0.65 to 0.70 for most subassemblies;
3. hexagonal-can geometry is well approximated by cylindrical geometry, i.e.,  $C$  is essentially independent of the geometry chosen for this evaluation.

The results of BOW-V calculations of core compression and bowing reactivity versus power, using  $C = 0.70$ , were much closer to experimental values than when  $C = 1.0$ . For Run 25 (stainless steel reflector), for instance, the calculated reactivity values with  $C = 0.7$  are about 10% higher than the measured values, whereas the calculated values with  $C = 1.0$  are at least 70% higher than the measured values.

---

\*This analysis assumed in all cases that the temperature distribution across a hexagonal can was symmetrical about the major axis of symmetry.



d. Work with MELT Codes (G. H. Golden and R. H. Shum)

The MELT-I code\* was used to determine the effects of various ramp rates of reactivity insertion ranging from 10¢/sec to 50\$/sec on a wet-critical EBR-II configuration. The reactor was assumed to be at 0.01% of full 62.5-MWt power and at 2% of full flow. Positive reactivity effects were due to the unbonded ramp input and the resulting collapse of fuel. The only negative effect was a constant fuel-expansion value of  $-3.9 \times 10^{-6} \Delta k/k$  per °K. The results of the calculations are summarized in Table I.D.17.

TABLE I.D.17. Summary of MELT-I Results for EBR-II Wet-critical Configuration at 0.01% Power and 2% Flow

$k_{in}$ (\$/sec)	Time after Start of Transient (sec)	Average Power Density (W/cc of fuel)	Total Energy Release (MW-sec)	Net k (d)	Collapse k (d)	Collapse $\dot{k}$ (\$/sec)	Total $\dot{k}^c$ (\$/sec)
0.10	-9.95 <sup>a</sup>	$-2.0 \times 10^4$	-220	-80	-70 <sup>b</sup>	-10 <sup>b</sup>	-10 <sup>b</sup>
0.50	2.27 <sup>a</sup>	$2.19 \times 10^4$	235	80.0	68.1 <sup>b</sup>	23.7 <sup>b</sup>	24.2 <sup>b</sup>
1.00	1.23 <sup>a</sup>	$2.10 \times 10^4$	248	78.0	62.9 <sup>b</sup>	20.5 <sup>b</sup>	21.5 <sup>b</sup>
5.00	0.310	$1.28 \times 10^5$	240	96.5	49.9	7.57	12.6
10.00	0.176	$1.63 \times 10^5$	234	97.3	29.3	7.29	17.3
10.00 <sup>d</sup>	0.176	$1.63 \times 10^5$	234	97.3	29.3	5.97	16.0
20.00	0.0967	$2.26 \times 10^5$	230	98.1	13.0	4.82	24.8
50.00	0.0411	$4.32 \times 10^5$	218	99.0	2.41	1.95	52.0

<sup>a</sup>Time to reach peak average fuel temperature (2630°K).

<sup>b</sup>Model for collapse k becoming questionable.

<sup>c</sup>Total  $\dot{k} = \dot{k}_{in} + \dot{k}_{collapse}$

<sup>d</sup>In slumping equation,  $(d^2H/dt^2) + \xi(dH/dt) = -g$ ;  $\xi = 0.3$ .

For the following reasons, these results should be considered only as qualitative:

1. The temperature throughout the core as a function of time is not well-characterized because of the projection scheme for heat transfer used by the code and also because the heat content versus temperature for the U-5 wt % Fs fuel was approximated.

2. Characterization of incipient slumping was difficult because of item 1 above, and because of a lack of understanding of the actual physical processes involved.

3. The fuel-expansion effect was assumed constant, i.e., independent of the physical state of the fuel.

4. A perturbation model was used to estimate collapse feedback, which became increasingly inaccurate with the lower ramp insertion rates.

Work is underway to improve these results both by using a newer version of the MELT code and by refining the input data.

\*Waltar, A. E., MELT-I, A Simplified Meltdown Code for Fast Reactor Safety Analysis, BNWL-944 (Dec 1968).

e. Thermal-Hydraulics of a Predominantly Oxide Core for EBR-II  
(G. H. Golden)

To investigate potential safety problems associated with the increasing number of experimental oxide subassemblies being placed in EBR-II, a predominantly oxide core was specified as one limiting point of reference. The thermal-hydraulic behavior of such a core, described in the Progress Report for November 1968, ANL-7518, pp. 39-40, has been computed using the SNAFU modification\* of the EVALUATE code. Key input for these calculations is summarized in Table I.D.18.

TABLE I.D.18. Input for Thermal-Hydraulics Calculations of Oxide Core for EBR-II

Reactor Power	62.5 MWt	
Sodium Inlet Temperature	700°F	
Average $\Delta T$ in Core	190°F	
Fuel-transition Temperatures	1650°C; 2150°F	
Conductance of Fuel-cladding Gap	1000 Btu/hr-ft <sup>2</sup> -°F	
Hot-spot Factors	$F_{coolant} = 1.15$	$F_{gap} = 1.30$
	$F_{film} = 1.25$	$F_{fuel} = 1.20$
	$F_{clad} = 1.15$	
Bypass Flow	0.5%	

Power distributions were obtained via one-dimensional diffusion theory using the ANL-23806 cross-section set. Safety subassemblies were fully inserted, and control subassemblies were 85% inserted. Calculations were done initially for a uniformly enriched core and subsequently with a ratio of enrichment in Rows 5 and 6 equal to that in Rows 1-4 so that a minimum core radial maximum-to-average power distribution was achieved. Results of the thermal-hydraulics calculations are summarized in Table I.D.19. The minimum fuel temperature occurs at an enrichment ratio of 1.3/1; at this enrichment, the peak fuel temperature at 10% over-power is less than the peak fuel temperature at normal power for the "unflattened" core.

TABLE I.D.19. Thermal-Hydraulic Characteristics of Oxide Core Subassemblies in EBR-II (temperatures include hot-spot factors)

Uranium-enrichment Ratio	Radial $P_{max}/P_{avg}$	Peak Linear Power (kW/ft)	Average Coolant Velocity in Peak Subassembly (ft/sec)	Peak Coolant Temperature (°F)	Peak Cladding Temperature (°F)	Peak Fuel Temperature (°F)
0.557/0.557 = 1.0/1	1.259	14.7	23.4	1012	1086	5222
0.637/0.490 = 1.3/1	1.121	13.1	20.3	1004	1084	4854
0.660/0.471 = 1.4/1	1.136	13.3	20.6	1005	1084	4891
0.681/0.454 = 1.5/1	1.157	13.5	21.1	1007	1084	4944
0.637/0.490 = 1.3/1 <sup>a</sup>	1.121	14.4	20.3	1034	1122	5159

<sup>a</sup>10% overpower conditions.

\*See Sect. I.D.8.g for more details of the modification.

f. Temperature Distribution in a Mechanically Mixed Oxide Fuel  
(R. K. Lo)

A transient-heat-transfer computer code (THTB) was used to predict the temperature distribution in heterogeneous  $\text{UO}_2$ - $\text{PuO}_2$  fuel for the case of a power increase following the postulated unplanned insertion of a control rod in an EBR-II core operating at 62.5 MWt. The reactor was assumed to be tripped on a sodium exit temperature of  $\sim 990^\circ\text{F}$ , and the time delay in instrument response was assumed to be 10.0 sec. The fuel rod considered was 0.25 in. in diameter, the cladding was 0.015 in. thick, the  $\text{PuO}_2$  particles were  $20\ \mu$  in size, and the  $\text{UO}_2$  particles  $500\ \mu$ . The contact conductance between the  $\text{PuO}_2$  and the  $\text{UO}_2$  particles was taken as 4000 Btu/hr-ft $^2$ - $^\circ\text{F}$ , and that between the  $\text{UO}_2$  particles and the cladding as 1500 Btu/hr-ft $^2$ - $^\circ\text{F}$ . The heat-transfer coefficient between flowing sodium and the cladding was assumed to be 1400 Btu/hr-ft $^2$ - $^\circ\text{F}$ , and the linear heat generation 16 kW/ft.

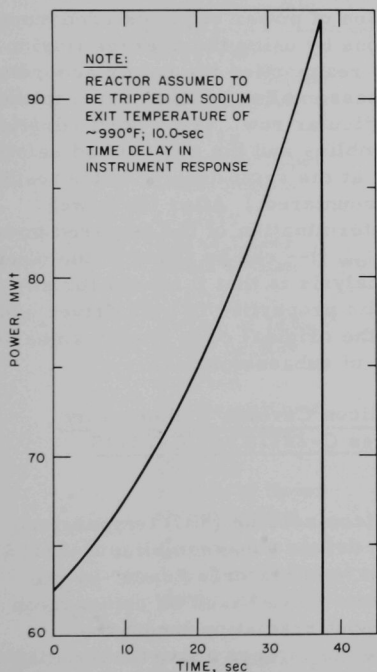


Fig. I.D.5. Power Increase Following a Postulated Insertion of a Control Rod in an EBR-II Core Operating at 62.5 MWt

By assuming that the fuel was located at Row 4 and that all the uranium was  $^{238}\text{U}$ , the relative power density in the plutonium was calculated to be 79.9%, and that in the uranium to be 20.1%. (The volumetric heat generation of  $\text{PuO}_2$  particles was  $5.803 \times 10^8$  Btu/hr-ft $^3$ , and that of  $\text{UO}_2$  particles was  $1.461 \times 10^8$  Btu/hr-ft $^3$ .) By using as input the power trace shown in Fig. I.D.5, computed with the AIROS II-A code, and physical data outlined above, the temperature distribution in the  $\text{PuO}_2$  and  $\text{UO}_2$  particles was obtained. The calculated volume-weighted average temperatures are shown in Fig. I.D.6. For this case, the volume-weighted temperature of  $\text{PuO}_2$  is almost exactly the same as that of the  $\text{UO}_2$ .

g. Thermal-Hydraulics Code for EBR-II (J. L. Gillette)

The thermal-hydraulics code EVALUATE has been rewritten for application to EBR-II and is now called SNAFU. The code modifications include changes in input and in the basic characterization of the reactor. In the first category are changes which: allow the thermal power (instead of the electric power) and the thermal efficiency of the reactor to be

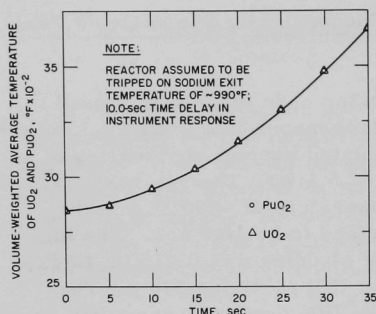


Fig. I.D.6. Calculated Transient Average Temperature for Power Increase Following a Postulated Insertion of a Control Rod in an EBR-II Core Operating at 62.5 MWt

used as input; allow the physical dimensions of the subassemblies to be read in; and allow the area of the reactor to be calculated instead of attempting to characterize EBR-II as a cylinder. A new feature of the code is that it now includes a model for the restructuring of oxide fuel as recently proposed at ANL (see Progress Report for June 1969, ANL-7581, pp. 1-2).

The characterization of the reactor has been changed by dividing the power between the driver subassemblies and the control and safety subassemblies. The design of the control and safety subassemblies makes this division of power necessary for accurate description of EBR-II. The division of power requires a renormal-

ization of the power distribution. This is done by using the average fission density in a region and the region volume to reapportion the power according to the ratio of the mass of fuel in driver subassemblies to that of fuel in the control and safety subassemblies in any particular row. (This normalization procedure assumes that the driver subassemblies and the control and safety subassemblies contain the same kind of fuel at the same density, but is readily modified when different types of fuel are encountered.) After the power reapportionment has been completed, the determination of the required power ratios--( $\bar{P}_{row i} / \bar{P}_{core}$ ) and ( $\bar{P}_{max row i} / \bar{P}_{row i}$ )-- can be found in the usual manner. The advantage of this method of analysis is that it allows for accurate determination of the thermal-hydraulic properties of both driver and control and safety subassemblies, whereas the original code simply smeared the power over the core containing all kinds of subassemblies.

#### h. Postirradiation Evaluation of Silicon Carbide Temperature Monitors in Driver Subassemblies C-2211S and C-2214S (V. G. Eschen)

Postirradiation evaluation of silicon carbide (SiC) temperature monitors removed from various positions in driver subassemblies C-2211S and C-2214S was completed. The irradiation temperatures "seen" by the SiC capsules were calculated. The calculations were based on comparison of preirradiation length with the changes in postirradiation length that resulted from heat treating the samples at temperatures above the irradiation temperatures. The results of the calculations are presented in Table I.D.20.

The temperatures listed in the table appear to be higher than those obtained from other types of sensors used in the same subassemblies, which were known to be reasonably accurate. Therefore, improvement in

the SiC technique is considered possible and desirable. One way to improve the technique appears to be to increase the length of the SiC monitors to 1 in. from the currently used 1/2 in. This should proportionately increase the magnitude of the change in length that is induced by irradiation. Therefore, measurable length changes could be obtained at heat-treating temperature intervals that are smaller, thus providing more data points for relating length changes as a function of heat-treating temperatures. This should improve the accuracy of the temperature-measuring system. Present plans include evaluation of temperature monitors of greater length.

TABLE I.D.20. Postirradiation Experimental Results for  
Silicon Carbide Temperature Monitors from Driver  
Subassemblies C-2211S and C-2214S

Subassembly Number and Location of Capsule in Subassembly	Capsule Identification	Irradiation Temperature Indicated by Monitor (°F)
C-2211S	20-1-A	1000
Center of Upper Shield Section	20-1-B	1000
C-2211S	20-2-A	1015
Bottom of Upper Shield Section	20-2-B <sup>a</sup>	-
C-2211S	20-3-A	725
Top of Lower Shield Section	20-3-B	720
C-2211S	20-4-A	725
Bottom of Lower Shield Section	20-4-B	710
C-2214S	20-5-A	1050
Middle of Upper Shield Section	20-5-B	1065
C-2214S	20-6-A	1055
Bottom of Upper Shield Section	20-6-B	1065
C-2214S	20-7-A	760
Top of Lower Shield Section	20-7-B	750
C-2211S	21-11-A	905
Top of Upper Shield Section	21-11-B	905
C-2211S	21-12-A	960
Top of Upper Shield Section	21-12-B	965

<sup>a</sup>Specimen was found to be broken when removed from the capsule.

## 9. Driver Fuel Development (C. M. Walter)

### a. High Burnup Encapsulated Irradiations (W. N. Beck)

Last Reported: ANL-7618, pp. 56-57 (Sept 1969).

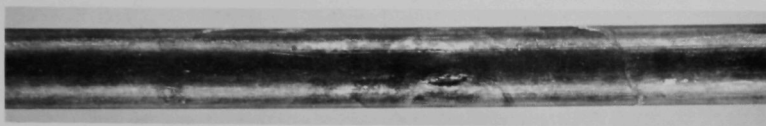
(i) Postirradiation Examination of Encapsulated Mark-IA Element BF08. Mark-IA Element BF08, which had been irradiated at a maximum cladding temperature of 478°C and to a calculated burnup of 2.6 at. %, is being given a detailed metallographic examination. The element was recovered in excellent condition. The maximum measured change in the element diameter ( $\Delta D/D$ ) was 1.2%, of which 0.5% is calculated to be due to swelling of the cladding. The fuel, a high-swelling alloy containing 78 ppm of silicon, had swollen to make intimate contact with the ID of the cladding; the extreme ends, however, were separated from the cladding by an annulus of 0.002 in. The fuel column had elongated 2.7%, but was still 0.062 in. shorter than the maximum length allowed in the element design. The amount of fission gas released to the plenum of the element was determined to be 0.54% of theoretical.

An attempt is being made to determine the plenum pressures in three high-burnup Mark-IA elements (including Element BF08) at their respective operating temperatures. An apparatus has been built and installed in the metallurgy Alpha-Gamma Hot Cell to permit pressurizing the element plenum while at temperature. The length of the fuel element first is measured as a function of temperature. Next, the plenum of the element is punctured, letting the plenum gas escape. Then gas from an outside source is forced into the element to bring its length back to that of the intact element. The first test was conducted with Element BF08. The results were not conclusive because the cladding of the element experienced an unexpected localized break while the element was at 450°C and the pressure in its plenum was 3000 psi. Tube-burst tests previously performed on irradiated element tubing indicated that, at 450°C, failure should be expected at pressures near 7500 to 8000 psi. Figure I.D.7 shows the break, which is 0.080 in. long and which produced an elevation of 0.015 in. in the cladding. Transverse metallographic sections were made through the area of the fracture. Etched surfaces of the cladding in the immediate area of the failure exhibit intergranular separation. The failed section will be examined by an electron microprobe for evidence of elemental carbon in the grain boundaries.

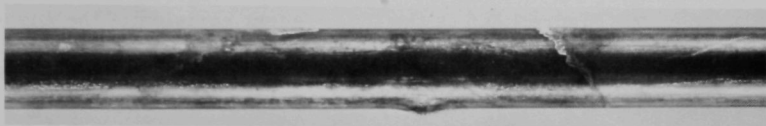
Figure I.D.8 shows the transverse section through the middle of the break. The fuel did not expand and follow the contour of the deformed cladding; instead, it appears to have been compressed. The diameter of the cladding on each side of the break did not change as a result of the applied pressure; however, a continuous narrow channel now interconnects the area of the failure and the plenum. An expulsion of sodium



accompanied the break, signifying that the bond sodium which accumulated in the plenum region created the hydrostatic pressure that was applied to the weak section of the cladding.

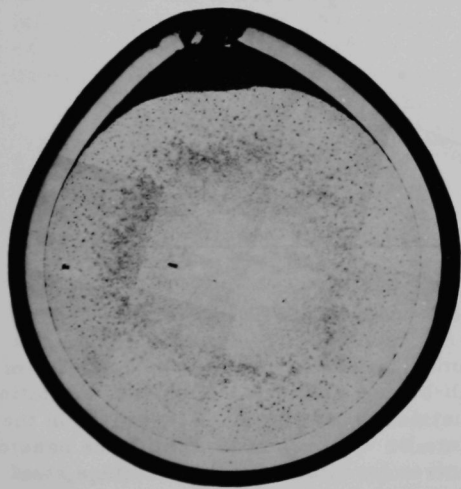


3.3X



3.3X

Fig. I.D.7. Localized Cladding Break in Element BF08 (2.6-at. % Burnup) Which Occurred during Postirradiation Pressure Tests at 3000 psi and 450°C



17X

Fig. I.D.8. Transverse Section through Middle of Break in Element BF08 Which Occurred during Postirradiation Pressure Tests at 3000 psi and 450°C

Two additional elements (BF02 and BF03), which have reached a calculated maximum burnup of 3.7 at. %, are scheduled to be pressure tested.

(ii) Postirradiation Examination of Mark-II Elements. Irradiated encapsulated Mark-II Element 207 has been sectioned and is being examined. The element had been irradiated at a maximum cladding temperature of 531°C and to a calculated burnup of 3.5 at. %. The fuel is making intimate contact with the ID of the cladding over its entire length. The crimp-type restrainer had been initially set at 0.20 in. above the fuel column. Neutron radiographs which had been taken at 2-at. % burnup showed the fuel touching the bottom edge of the crimps. The fuel is now even with the top edge of the crimp

and is domed. Fuel volume expansion is calculated to be 38%. The fission gas released to the plenum was recovered and was determined to be 49% of



theoretical. Void formation and bubble distribution are very similar to those observed in elements examined at lower burnups. There is no evidence of diffusion zones or of interaction between the fuel and the cladding.

#### b. Fuel and Cladding Surveillance

Last Reported: ANL-7632, pp. 65-71 (Oct 1969).

##### (i) Surveillance of Extended-burnup Driver Fuel (J. P. Bacca, A. K. Chakraborty, and G. C. McClellan)

Figure I.D.9 is the most recent revision of the curve relating irradiation swelling of driver fuel to burnup. This figure is based on all data obtained from examinations of fuel produced in both the hot line and cold line of the Fuel Cycle Facility.

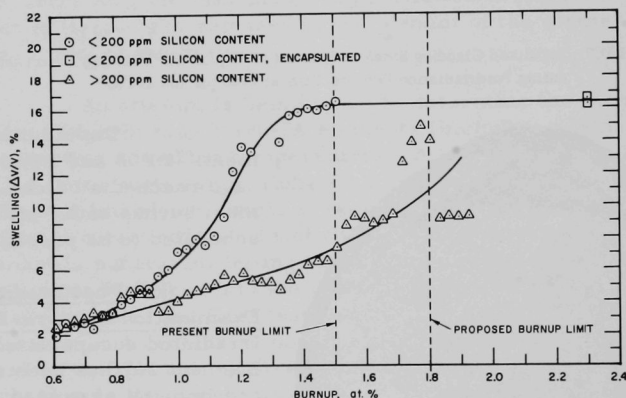


Fig. I.D.9. Volume Swelling of Mark-IA Driver Fuel as a Function of Burnup

Figure I.D.10 summarizes the changes in the diameter of driver fuel as measured for 36 high-burnup elements. Elements exhibiting more than and less than 14% volumetric fuel swelling are identified in the figure. All but 4 of the 36 data points lie within the 95% confidence band of the swelling expected from fast-neutron irradiation of the stainless steel cladding\* of the fuel elements. Therefore, no real plastic strain of the cladding can be discerned at the burnup levels considered to date.

The information shown was used in an ANL proposal to RDT for increasing the maximum burnup limit of EBR-II driver fuel from the present 1.5 to 1.8 at. %. These limits are indicated on Fig. I.D.9.

\*Claudson, T. T., PNL, private communication.

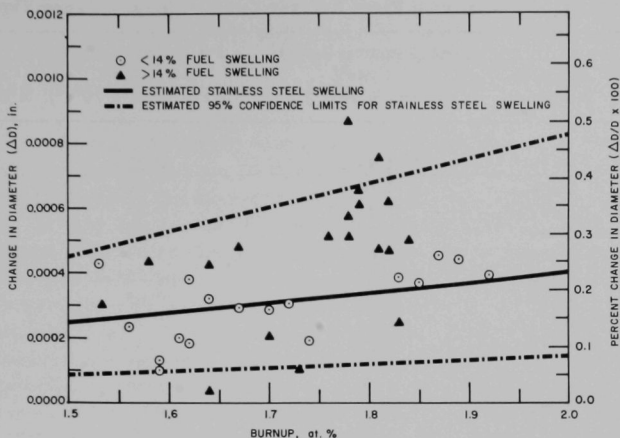


Fig. I.D.10. Diameter Change of Mark-IA Driver-fuel Element as a Function of Burnup

(ii) In-pile Creep Studies (C. M. Walter and M. A. Pugacz)

Uncertainty as to the proper creep equation for BEMOD calculations has led to the development of a program to obtain missing information in this area. There is an almost universal interest in in-pile creep data for stainless steel for use in core design and for predicting the capability of fuel elements throughout the LMFBFR community.

The initial experiment of the program consists of irradiating a Mark-B37 subassembly (XO65) containing 18 pressurized annealed Type 304L stainless steel tubes exposed directly to the flowing primary sodium in EBR-II. These tubes are 0.290 in. in outside diameter, have a 20-mil wall, and are 60 in. long. They have been charged with helium in groups of three to give hoop stresses of 10,000, 15,000, 20,000, 25,000, 30,000, and 35,000 psi at the 700°F sodium inlet temperature, and are being irradiated in a 7N5 position. The remaining 19 positions in the subassembly contain dummy tubes, rods, temperature monitors, and flux monitors.

Table I.D.21 presents the results of the first reactor run (1200 MWd) of the experiment. The  $\Delta D/D$  values (% change in diameter) are greater at the tops of the tubes than at the bottoms. This is a result of higher temperatures at the tops, which are mainly due to radial conduction of heat into the subassembly from adjacent subassemblies. The  $\Delta D/D$  values at the bottoms (which are at 700°F) are quite consistent with the values for primary thermal creep found in out-of-pile thermal controls (see Table I.D.22). A typical diameter profile, shown in Fig. I.D.11, gives no indication of enhanced creep in the high-flux region within the data scatter. (The bottom of the reactor core is 23 in. above the tube bottoms.) The figure plots average values of diameter measurements at 0° and 90° orientations for the pre- and postirradiation conditions.

TABLE I.D.21. Results from First Reactor Cycle of In-pile Creep Experiment<sup>a</sup>

Initial Hoop Stress (psi)	Capsule Number	Peak Fluence (calc) >0.1 MeV (n/cm <sup>2</sup> × 10 <sup>-21</sup> )	Peak Flux (calc) >0.1 MeV (n/cm <sup>2</sup> -sec × 10 <sup>-15</sup> )	$\Delta D/D$ (%)	
				Bottom	Top
Dummy					
Dosimeter	P-19	1.93	0.93	0.07	0.06
10,000	P-32	2.13	1.02	0.07	0.08
10,000	P-39	1.93	0.93	0.09	0.09
10,000	P-49	1.87	0.90	0.13	0.09
15,000	P-34	2.23	1.07	0.12	0.12
15,000	P-40	1.56	0.75	0.09	0.13
15,000	P-43	1.71	0.83	0.06	0.13
20,000	P-35	2.13	1.02	0.15	0.33
20,000	P-41	1.93	0.93	0.12	0.34
20,000	P-42	1.71	0.83	0.13	0.19
25,000	P-30	2.08	1.00	0.23	0.60
25,000	P-44	1.96	0.95	0.43	0.52
25,000	P-57	1.87	0.90	0.34	0.45
30,000	P-36	2.44	1.17	0.66	1.02
30,000	P-37	1.76	0.85	0.72	0.90
30,000	P-29	1.56	0.75	0.83	0.91
35,000	P-38	2.34	1.12	0.95	1.22
35,000	P-45	2.19	1.05	1.14	1.14
35,000	P-48	1.93	0.93	0.86	1.52

<sup>a</sup>Time at power, 544 hr; total time in reactor, 1154 hr.

TABLE I.D.22. Out-of-pile Biaxial Creep of Thermal Controls (725°F)<sup>a</sup>

Hoop Stress (psi)	$\Delta D/D$ (%)
15,000	0.02
20,000	0.07
25,000	0.25
30,000	0.65
35,000	0.95

<sup>a</sup>Creep test ran for 25 to 200 hr. The  $\Delta D/D$  values appear to be independent of time.

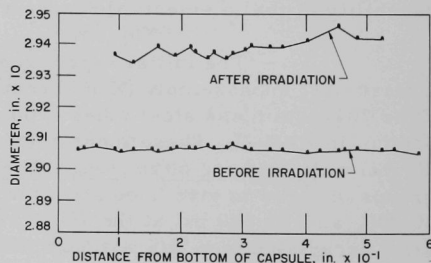


Fig. I.D.11. Pre- and Postirradiation Diameter Profiles of In-pile Creep Capsule P-38. Initial hoop stress was 35,000 psi.

The first attempt at measuring temperatures by use of melt wires was unsuccessful. Temperature-monitoring capsules containing silicon carbide pellets and sodium-expansion indicators are being assembled for the earliest possible insertion into the subassembly. The temperature near the tube tops is not known. After this temperature has been determined, more-thorough out-of-pile tests with thermal controls will be performed.

Subassembly XO65 has been irradiated for a second cycle (600 MWd) in EBR-II and is awaiting inspection. It is hoped that succeeding

cycles (three to six are planned) will show increasing  $\Delta D/D$  values in the high-flux portion of the tubes. At EBR-II operating temperatures, secondary thermal creep in stainless steel should be near zero.

Some important facts learned from the first experiment (Creep 1) will aid in the design of the second experiment (Creep 2). There is only one well-defined temperature in EBR-II: the 700°F sodium inlet temperature. It was hoped that Creep 1 would operate at 700°F, but radial conduction from adjacent subassemblies turned out to be a significant problem. Creep 2 will employ a subassembly design (double hexagonal can with an intermediate gas gap) that should effectively thermally insulate the test subassembly from adjacent subassemblies. Creep 2 will not use as-received annealed tubing; this tubing has been straightened and sized after annealing, producing small coldworked areas which cause nonuniform strain. Creep-1 tubes are wire wrapped. The wrap will be eliminated in Creep 2, thereby avoiding the possibility of the stress interaction between tubes that results from crowding of tube against tube during irradiation. Creep-1 tubes contain solid stainless steel filler rods, occupying 90% of the tube volume, to reduce the energy release in the event of a rupture. Unfortunately, if appreciable strain occurs during testing, the filler rod accentuates the stress reduction on the tube by a factor of 10. Creep 2 will eliminate or greatly reduce the size of this filler rod so that more constant stress is attained during the irradiation tests.

The tubes for Creep 2 will be obtained from PNL. They will be made of Type 316 stainless steel and will have an outside diameter of 0.230 in. and a wall thickness of 15 mils. The experiment will explore effects of flux, fluence, stress, cold work, grain size, and heat treatment on flux-controlled creep at 700°F.

A future in-pile creep experiment will explore the effects of temperature, using a subassembly that preheats sodium in a gamma-heating section. The hot primary sodium will flow by the pressurized tubes in the testing chamber.

#### 10. Operation with Failed Fuel (R. R. Smith)

Last Reported: ANL-7632, pp. 71-76 (Oct 1969).

##### a. TREAT Simulations of EBR-II Fuel Failures

- (i) Flat-topped TREAT Transient with Partially Bonded Mark-IA EBR-II Fuel Element EBR-MF-2 (R. M. Fryer and R. R. Smith)

The second in a series of experiments to investigate the effects of residual bond sodium on melting in a Mark-IA EBR-II fuel element

has been performed. A 6%-enriched fuel element (EBR-MF-2) was subjected to a flat-topped TREAT transient in flowing sodium in the Mark-I sodium loop. To simulate the loss of bond, the fuel element was loaded with a deficient quantity of bond sodium, then sealed and impact bonded. This procedure produced an element with a normal bond along the lower 4 in., a partial bond along the center 4 in., and no bond over the upper  $5\frac{1}{2}$  in.

The test specimen, enriched to 6 wt % in  $^{235}\text{U}$ , was subjected for approximately 8 sec to a flat-topped TREAT transient, during which the average power density corresponded to an EBR-II power level of 100 MWt. The actual power profile is illustrated in Fig. I.D.12. The inlet and outlet coolant sodium temperatures in the loop during the transient are shown in Fig. I.D.13.

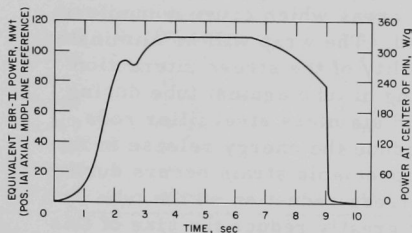


Fig. I.D.12. Power History for Element EBR-MR-2

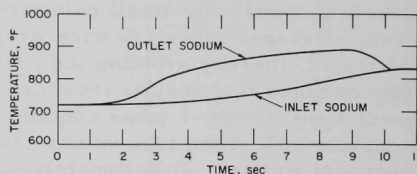


Fig. I.D.13. Sodium Temperatures in Mark-I Loop during TREAT Transient for Element EBR-MR-2

A neutron radiograph of the test element in the loop showed that the restrainer-to-fuel separation had increased from 0.5 to 1.0 in., thus clearly indicating fuel melting. The fuel specimen has been removed from the loop and cleaned. Extensive postirradiation examinations will be conducted. These will include jacket profilometry, gamma scans, total-fission determinations, and metallographic examinations.

(ii) Postirradiation Examination of Element EBR-MF-1  
(D. L. Mitchell, R. V. Strain, and D. M. Cheney)

Element EBR-MF-1, a partially bonded Mark-IA driver-fuel element, has been irradiated in the TREAT reactor to determine if fuel melting would occur under conditions that would simulate extreme overpower conditions in EBR-II for a short time (~10 sec). Before irradiation, the lower  $4\frac{1}{2}$  in. of the fuel pin in the element had been completely bonded, but the upper 9 in. had been only wetted with sodium throughout half of the pin circumference.

Postirradiation eddy-current bond testing and neutron radiography showed that the fuel pin had not slumped during the TREAT test. Measurements of the diameter of the element did not reveal any straining of the jacket.

The cladding was removed from the fuel pin. The lower half of the pin was found to be surrounded with sodium, except for two voids, and the upper half of the element had only 180° (circumferential) of sodium in the annulus. Measurements of the pin itself revealed no appreciable changes in diameter or length.

Metallographic examination of samples from the pin revealed no evidence of fuel melting. The microstructure and the microhardness values indicated that the upper portion of the pin had exceeded the gamma-phase transition temperature ( $\sim 650^{\circ}\text{C}$ ) and had been cooled from that transition temperature at a fairly rapid rate. The samples from the lower (bonded) section of the fuel pin are typical of unirradiated, as-bonded fuel pins.

These results indicate that the partial bonding near the top of the element provided relatively good heat transfer from the fuel pin during the TREAT test.

b. Fuel-motion Transducer (J. R. Karvinen, A. A. Madson, and J. W. Rizzie)

The first calibration tests of the fuel-motion transducer in the argon cell of the Fuel Cycle Facility yielded unanticipated results. Only 5 mils of expansion were recorded with the quartz rod. The fuel pin selected (from Subassembly 2178) then was loaded, and again only a few mils of movement were recorded. A neutron radiograph showed that the pushrod for connecting the fuel with the sensing piston of the monitor was not touching the top of the fuel. The assembly was disassembled, and the pushrod was found to be binding on the fuel cladding. Accordingly, the relative motion between the cladding and the supporting jacket was being recorded. This measurement was obscured because only friction contact was being provided; therefore, no conclusions relative to motion between the fuel cladding and the fixture can be made.

After the pushrod has been inserted correctly, a calibration was made with the quartz rod. This time a separation of 146 mils over the temperature range from 100 to 1000°F was noted. With the fuel pin loaded, a negative expansion of 15 mils was recorded. This indicates that the fuel has a lower coefficient of expansion than the stainless steel jacket, and expands 131 mils over the same temperature range.

Another effect was an irreversible 15-mil expansion of the fuel in the final three heat cycles of 100 to 1100°F. In the two previous calibration tests, the maximum temperature was limited to 908°F. After the third higher-temperature cycle, the expansion curve returned each time to the same point as at the end of the third cycle. The fuel was removed from the fixture and was remeasured by a dial indicator provided in the fixture for preparing the fuel pins. This measurement indicated 23 mils of growth from the initial measurement made on the uncycled pin.



## 11. Physics Mock-up Studies

Not previously reported.

### a. Planning for EBR-II Critical-assembly Experiments (D. Meneghetti)

Planning for EBR-II critical-assembly experiments and scoping calculations relative to the experimental assemblies are under way. The critical assemblies being considered are of both the heterogeneous-core and of the homogeneous-core types. They are: (1) a homogeneous EBR-II type core having a depleted-uranium-rich radial reflector; (2) a homogeneous EBR-II type core having a nickel-rich radial reflector; (3) a heterogeneous EBR-II type core having a nickel-rich radial reflector; and (4) a two-zoned heterogeneous EBR-II core, with a nickel radial reflector, in which the central core region consists of mixed-oxide- and/or carbide-fueled drawers of dilution representing a large oxide or carbide system, and the outer core region consists of the current EBR-II driver composition. In a "heterogeneous" core, as defined here, the representative EBR-II sub-assemblies are simulated with the drawers of the critical assembly. "Homogeneous" refers to loading the critical assembly with a smeared EBR-II core composition.

Studies of the gross characteristics of a nickel-reflected EBR-II system will be undertaken largely with the heterogeneous-core, nickel-reflected mockup assembly. The homogeneous cores having depleted-uranium or nickel reflectors will be used primarily for correlating proton-recoil spectra with dosimetry foil activities and for studies of axial-reflector variations. Experiments with the two-zoned assembly will enable the generation of data necessary for understanding the characteristics of EBR-II having clusters of very dilute oxide or carbide fuels.

### b. Effects of Leakage Absorptions on the Values of Flux-weighted Cross Sections in Thin-slab-cell Calculations (D. Meneghetti and K. E. Phillips)

Flux variations within ZPR critical-assembly drawers are usually obtained by slab-cell calculations. Since such calculations inherently do not account for the effects of overall leakage into or out of the cell, the use of a leakage absorption applied throughout the cell is frequently used.

Cell flux-averaged cross sections derived both by use and by nonuse of leakage absorptions have been calculated for a series of simple binary-cell situations. The results have been compared with corresponding averaged cross sections obtained by direct two-dimensional calculations. The latter use infinitely high layers of disk-shaped binary cells. The leakage from the systems were radial and thus in directions parallel to the plane of the binary cells.



One-group, applied-source calculations were used. The single-group cross sections for transport and removal corresponded approximately to those of neutrons above 1.35 MeV. For the examples whose results are described below, the "fissile" and "diluent" regions were 0.64 and 4.48 cm thick, respectively.

With the applied source in the fuel, one-dimensional cell calculations of the flux gave space-averaged removal cross sections of 0.0417 and 0.0407  $\text{cm}^{-1}$  with and without leakage absorptions, respectively. The direct heterogeneous two-dimensional calculation gave a value of 0.0418  $\text{cm}^{-1}$ .

To augment further the parallel leakage, the calculations were repeated with the "diluent" region reduced to one-eighth of its original density. The removal values from the one-dimensional fine-flux determinations then were 0.0196 and 0.0183  $\text{cm}^{-1}$  with and without the use of leakage absorptions, respectively. The direct two-dimensional calculation gave a value of 0.0197  $\text{cm}^{-1}$ .

#### c. Development of the MELT-II Code (R. H. Shum)

The MELT-II code, a FORTRAN-IV version of the method written for UNIVAC 1108, has been obtained from Battelle Northwest Laboratory and is being modified for the IBM 360/75 computer. MELT-II is a coupled neutronics and heat-transfer code designed primarily for investigating fast-reactor core behavior under major accident conditions. However, inter-comparison\* of MELT-II with the FORE-II and NUTIGER codes indicates that MELT-II can be useful for investigating a wide variety of mild transients.

MELT-II is capable of calculating temperatures in up to 10 radial channels (fuel pin at 10 radial locations), each consisting of up to 20 axial segments and 15 radial nodes (12 fuel nodes plus the bond, cladding, and coolant nodes). Thermal conductivity and specific heat can be specified as a function of temperature, and all pin materials are allowed to undergo one phase change. Inlet temperature of the coolant plenum can be specified as a function of time, and the flow rate within each channel can be time dependent. Initial steady-state power from fission-product heating can be specified in addition to the neutronic power.

An implicit scheme is used to obtain fuel-pin temperatures, and a variable-time-step algorithm is used to govern the neutronics computations. Feedback due to axial fuel expansion, axial cladding expansion, sodium density change, fuel collapse, Doppler effect, and sodium voiding can be accommodated. Spatial weighting factors can be used for the Doppler and sodium-feedback effects. Scram conditions can be initiated by a power, period, or sodium-outlet-temperature trip, and in all cases, the actual scram reactivity change can be delayed beyond the trip setting by a specified time.

---

\*Fast Flux Test Facility Periodic Technical Report, BNWL-941 (May 1969).

For accident conditions that do not lead to a prompt critical situation, a zero-lifetime approximation can be employed to minimize computer time. A mixed-mode option also has been developed to combine the calculational advantages of the "exact" point kinetics formulation with the zero-lifetime approach.

## E. EBR-II--Operations

### 1. Reactor Plant (G. E. Deegan)

Last Reported: ANL-7632, p. 77 (Oct 1969).

The reactor remained shut down for an extended period of maintenance and for installation of the instrumented subassembly. Cooldown of all plant systems was completed on Oct. 21, and the steam system was drained and placed in dry layup.

The test-1 instrumented subassembly was installed, and its operation and protective interlocks in fuel handling were functionally checked. Readout of the subassembly instrumentation also was checked with primary-system flow and a bulk-sodium temperature of 580°F. Instrumentation leads then were successfully severed. All tests associated with the subassembly were satisfactory. Difficulty was experienced, however, in obtaining the full 360° rotation of the small rotating plug of the reactor. By raising the temperature of the primary-tank bulk sodium to 650°F, rotation was accomplished, and the test-1 instrumented subassembly was transferred to the storage basket. While the bulk sodium was being cooled to 580°F, test 1 was transferred to the temporary coffin and the test-2 instrumented subassembly preheated. Test 2 is being installed in reactor position 5F3.

The loading changes following Run 38B and before the reactor cooldown included the following:

Structural experiment XO65A was removed from the reactor and transferred to the Fuel Cycle Facility because of the undesirability of leaving the experiment immersed in sodium for an extended period of time. Two stainless steel core-dummy subassemblies and one natural-uranium core-dummy subassembly were installed in the core to provide increased shutdown margin during the cooldown. The No. 6 control rod was removed, and the position it had occupied was left vacant for the instrumented subassembly.

### 2. Fuel Cycle Facility (M. J. Feldman)

#### a. Fuel (D. L. Mitchell)

Last Reported: ANL-7632, p. 78 (Oct 1969).

(i) Cold-line Production and Assembly. Table I.E.1 summarizes the production activities for Oct. 16 through Nov. 15, 1969, and for the year to date.

TABLE I.E.1. Production Summary for FCF Cold Line

	10/16/69 through 11/15/69		Total This Year	
	Mark IA	Mark II	Mark IA	Mark II
Alloy-preparation runs				
New fuel	0	0	11	8
Remelts	<u>3</u>	<u>0</u>	<u>18</u>	<u>3</u>
Total	3	0	29	11
Injection-casting runs	3	0	39	10
Pins processed				
Accepted	263	0	3,759	941
Rejected	3	0	119	53
Elements welded	621	0	4,333	884
Elements rewelded	0	0	0	69 <sup>a</sup>
Elements leaktested				
Accepted	672	0	4,206	804
Rejected	6	0	94	21
Elements bondtested				
Accepted	776	0	4,023	934
Rejected	76	0	412	9
Subassemblies fabricated (cold-line fuel)	6	0	37	6
Bonded elements received from vendor	0		24,313 <sup>b</sup>	
Inspected and accepted	214		23,621 <sup>b,c</sup>	
Inspected and rejected	11		1,251 <sup>b</sup>	
Unbonded elements received from vendor	7,025		9,204 <sup>d</sup>	
Impact bonded, inspected, and accepted by ANL	0		1,979	
Impact bonded, inspected, and rejected by ANL	0		190	
Subassemblies fabricated (vendor fuel)	0		16 <sup>e</sup>	
Total elements available for subassembly fabrication as of 11/15/69				
Cold-line fuel				
Mark IA	1,448			
Mark II	234			
Vendor fuel (Mark IA)	22,608 <sup>f</sup>			

<sup>a</sup>Includes 64 elements in which visual examination of welds indicated that they were not acceptable for potentially high-burnup experiments.

<sup>b</sup>Total includes figures for 1968.

<sup>c</sup>Includes fuel elements returned to vendor for rework to correct voids in sodium bond and after rework sent back to ANL for reinspection.

<sup>d</sup>Ten unbonded vendor elements were set aside for historical samples.

<sup>e</sup>Includes subassemblies made up of a mixture of vendor and cold-line fuel elements.

<sup>f</sup>This figure does not include vendor elements that were impact bonded by ANL.

Six Mark-IA subassemblies containing fuel elements produced in the cold line were fabricated in the cold line during the month.

A total of 7025 unbonded fuel elements were received this month from the Aerojet-General Corporation (AGC) for impact bonding by ANL; none was impact bonded during the month. Data relating to receipt, impact bonding, and acceptance of these AGC elements are included in Table I.E.1.

(ii) Inspection of Vendor Fuel. The 225 AGC-fabricated elements received last month have been inspected. Of these, 214 were accepted. The remaining 11 were vendor rejects. The current number (as of November 15, 1969) of AGC elements available after verification inspection is 22,608, not including the AGC elements that have been impact bonded by ANL. A summary of the data relating to receipt and acceptance of the fuel produced by AGC is included in Table I.E.1.

b. Surveillance (M. J. Feldman, J. P. Bacca, and E. R. Ebersole)

Last Reported: ANL-7632, pp. 78-92 (Oct 1969).

(i) Postirradiation Analysis of EBR-II Fuel (J. P. Bacca)

(a) Influence of Composition on Irradiation-induced Swelling of U-5 wt % Fs Driver-fuel Alloy (S. T. Zegler)

An analysis was made of all postirradiation swelling data obtained to date for batches of U-5 wt % Fs driver fuel which deviated in composition from that required by Revision 5 of the product specifications for the Mark-IA fuel (Specification FCF-1, Product Specification for the EBR-II Driver Fuel Elements). The findings indicate that the tolerance limits for certain component elements of the alloy, as defined by Revision 5, can be expanded without causing any significant change in the amount of irradiation swelling of the alloy. Table I.E.2 lists the elements

TABLE I.E.2. Composition Ranges of Alloying Elements and Impurity Levels in U-5 wt % Fs Driver-fuel Alloy as Specified in Revision 5 and Revision 7 (Proposed) of Specification FCF-1<sup>a</sup>

Element	Revision 5	Revision 7 (Proposed)
<u>Alloy Composition Range (wt %)</u>		
Molybdenum	$2.44 \pm 0.17$	$2.44 \pm 0.17$
Ruthenium	$1.94 \pm 0.16$	$1.95 \pm 0.25$
Rhodium	$0.28 \pm 0.05$	$0.28 \pm 0.05$
Palladium	$0.19 \pm 0.04$	$0.19 \pm 0.04$
Zirconium	$0.10 \pm 0.03$	$0.09 \pm 0.06$
Niobium	$0.01 \pm 0.006$	$0.015 \pm 0.012$
Silicon	$0.04 \pm 0.012$	$0.05 \pm 0.027$
<u>Maximum Impurity Levels (ppm)</u>		
Aluminum	300	400
Carbon	400	600
Nickel	200	250
Total Impurities	2200	2550

<sup>a</sup>Product Specification for the EBR-II Driver Fuel Elements.

(alloying and impurities) that were studied, their tolerance limits as defined by Revision 5 of Specification FCF-1, and the specific extent to which the analysis indicates that the tolerance limit of each may be extended for a proposed revision (number 7) of Specification FCF-1. Tabulated in Table I.E.3 for each element studied are the most extreme deviations in composition from the specifications given in Revision 5 of Specification FCF-1, and the corresponding measured maximum values of irradiation swelling and swelling rate.

TABLE I.E.3. Summary of Maximum Swelling and Swelling Rate for Largest Deviations from Specification FCF-1 (Revision 5)<sup>a</sup> of Component Materials in EBR-II Driver Fuel

Element	Value Deviating from Specification (wt %)		Silicon Content of Fuel (ppm)	Fuel Batch No.	Subassembly No.	Maximum Burnup (at. %)	Maximum Total Volume Swelling of Fuel ( $\Delta V/V$ ) (%)	Maximum Swelling Rate <sup>b</sup>
	Min	Max						
Silicon	0.024			0427	C-2085	1.46	5.86	4.0
		0.092		4265	C-2163	1.20	6.56	5.5
Molybdenum	1.91		213	0301	C-283	1.20	12.4	10.2
		2.76	102	SL-16	C-186	1.20	14.7	12.3
Ruthenium	1.73		307	CL-045	C-2130	1.10	5.3	4.8
		2.61	260	4012	B-342	1.14	4.3	3.8
		2.72	785	R-410	C-2077	0.79	3.7	4.7
Rhodium	0.18		170	0408	C-2049	0.88	7.14	8.1
	0.20		630	0703 <sup>c</sup>	C-2175	1.17	7.84	6.7
		0.39	350	0450	C-2112	1.19	6.38	5.4
Palladium	0.12		90	0422	C-2101	1.45	15.8	10.9
Zirconium	0.028		568	4225	C-2103	1.16	7.08	6.1
		0.25	300	CL-025	C-2148	1.47	6.02	4.1
Niobium	0.002		362	0702 <sup>c</sup>	C-2184	1.63	16.7	10.25
		0.021	100	0437	C-2093	1.39	16.7	12.0
		0.097	224	4247	C-2135	0.97	4.7	4.8
Carbon		0.067	1111	4264	C-2163	1.19	6.28	5.3
		0.078	881	4261	C-2156	0.86	5.1	5.9
Aluminum		0.059	330	0454	C-2112	1.18	5.54	4.7

<sup>a</sup>Product Specification for the EBR-II Driver Fuel Elements.

<sup>b</sup>Maximum swelling rate = ( $\Delta V/V$ ) (l/burnup).

<sup>c</sup>70%-enriched driver fuel.

c. Experimental Support (J. P. Bacca and N. R. Grant)

Last Reported: ANL-7632, pp. 93-94 (Oct 1969).

(i) Comparison of Measured and Calculated Diameter Changes for Capsules C-1 and C-17 from Experimental Irradiation Subassembly XO12 (R. V. Strain)

Calculations of the changes in diameter resulting from irradiation-induced swelling of stainless steel were made with two capsules (numbers C-1 and C-17) from Subassembly XO12, using the following equation:

$$\Delta V(\%) = 10^{-48.310}(\phi t)^{1.71} 10^{\left( \frac{1.549 \times 10^4}{T} - \frac{5.988 \times 10^6}{T^2} \right)},$$

where

$\Delta V(\%)$  = percent volume change of the stainless steel;

$(\phi t)$  = neutron fluence having energy greater than 0.1 MeV;

T = temperature in degrees Kelvin.

The diameter change in the capsules due to the swelling of the stainless steel was assumed to be one-third of the volume swelling of the stainless steel, since this swelling is considered to be isotropic.

The temperatures used in the calculations were average values of the temperatures of the outside- and inside-diameter surfaces of the capsules, as calculated using the HECTIC code. The fluences used were calculated and were based on the axial-flux profiles given in the Laboratory's "Guide for Irradiation Experiments in EBR-II."

Figures I.E.1 and I.E.2 show the rather good agreement that resulted when the calculated capsule diameters were compared with the measured capsule diameters. The diameters of the capsules were measured with a remotely operated Bausch & Lomb Model DR-25B optical gauge. The measurements are considered to be accurate to  $\pm 0.0001$  in.

Stainless steel swelling was calculated for only the fueled portion of the capsules that had been irradiated in the core region of the reactor; no flux values were available for the axial blanket regions. Because

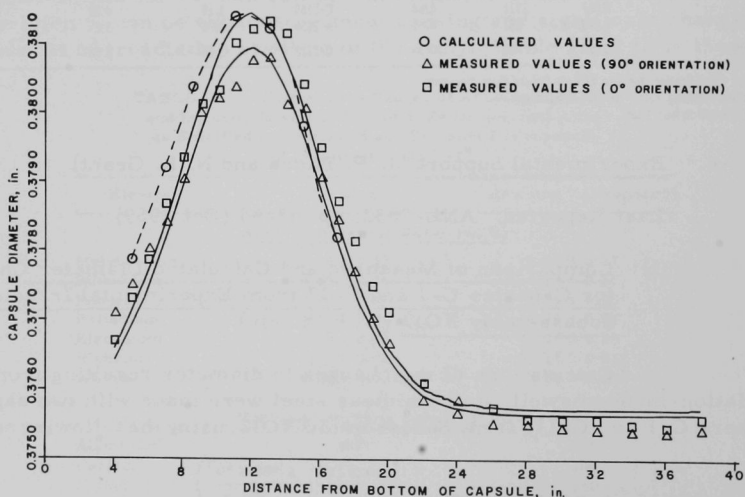


Fig. I.E.1. Diameter Profile of Capsule C-1 Subassembly XO12

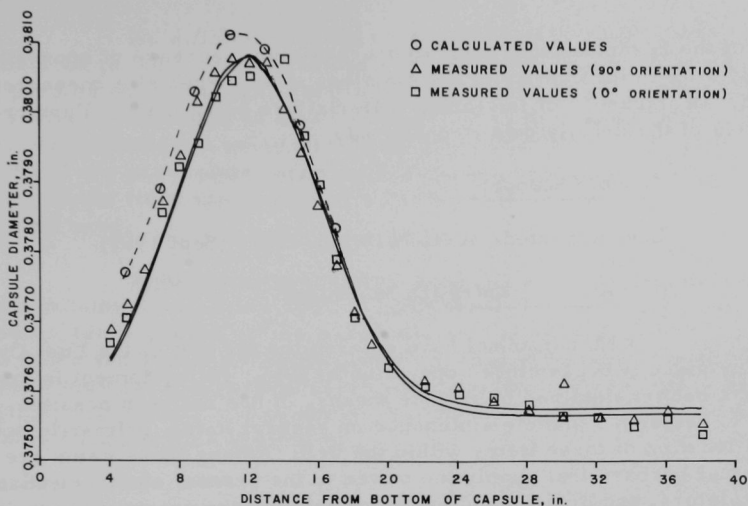


Fig. 1.E.2. Diameter Profile of Capsule C-17 from Subassembly XO12

of inherent errors in the values used in the calculations as well as perturbations in the neutron flux around experimental subassemblies in the EBR-II core, there is some uncertainty in the calculated fluence values for the core region. The differences between the calculated and measured diameter changes are probably within the range of error in the fluence values used in these calculations.

- (ii) The Effect of Irradiation in EBR-II on Type 304 Stainless Steel: An Interim Report on Experimental Subassembly XA08 (C. L. Meyers, R. V. Strain, E. R. Ebersole, and F. D. McGinnis)

Experimental Subassembly XA08 was irradiated in EBR-II for a total exposure of about 19,000 MWd (calculated total fluence of approximately  $8 \times 10^{22}$  n/cm<sup>2</sup>). The subassembly contained eight capsules loaded with Group C-2 carbide fuel and eleven capsules loaded with structural-metals samples. The subassembly was surrounded by driver-fuel subassemblies during more than 95% of its exposure time in the core, and was removed from the core on June 29, 1969.

Visual examination of the subassembly in the Fuel Cycle Facility indicated that significant expansion (lateral bulging) of the Type 304 stainless steel hexagonal tubing had occurred as a result of its irradiation service. Flat-to-flat measurements of the tubing in all three radial orientations indicated a maximum increase of 0.056 in. (2.5%) over the preirradiation nominal dimensions of the tubing. Precision density measurements (using CCl<sub>4</sub>) of samples taken from along the length of several



flats of the hexagonal tube indicated a maximum decrease of approximately 2.7% in the density of the stainless steel. Precision measurements of the wall thickness of the tubing material are being made. Further analysis of the density data is under way.

#### d. Reactor Support

Last Reported: ANL-7618, pp. 77-78 (Sept 1969).

##### (i) Air-cell Entry (D. M. Paige)

No personnel have entered the air cell of the Fuel Cycle Facility since it began closed operation in 1965. All equipment in the cell has been maintained by remote means. It has not been possible, however, to perform remote maintenance on several items, primarily because of the location of these items within the cell. Among these items are the electrical busbars that supply the power to the cranes, electromechanical manipulators, and bridges and bridge wheels for the cranes and manipulators. Although no major problems have been encountered with these items, it was decided that the time during which the reactor was shut down for installation of the instrumented subassembly should be utilized to examine and perform maintenance on them.

Before starting remote cleanup of the cell interior, all fuel, irradiated structural material, and process equipment (except the vertical assembly-dismantler and the final-assembly machine) were removed from the cell. (The final-assembly machine was subsequently removed from the cell after the doors were opened; the assembly-dismantler will remain in the cell.) The cleanup campaign is completed. Remote cleaning of the cell was accomplished with use of the in-cell manipulators and appropriate tools for sweeping, dry mopping, and vacuuming. After an initial entry to the cell was made to determine approximate working time required, direct cleaning operations were performed by washing with a solution of soap and water and rinsing with clear water. The reduction in radioactivity levels in the cell during the various cleaning operations is shown in Table I.E.4.

TABLE I.E.4. Radiation Levels in the Air Cell of the Fuel Cycle Facility during Cleaning Operations

Date of Survey	Radiation Level (R/hr)										West Pits	East Pits	East End, Center	Door
	Window Number <sup>a</sup>													
	1	2	3	4	5	6	7	8	9					
10/15/69 <sup>b</sup>	14	8.0	3.0	1.1	2.7	6.7	29	26	21	7.0	16	15	36	
10/17/69 <sup>c</sup>	2.3	3.0	2.0	0.4	1.2	2.8	7.7	4.1	1.3	3.5	3.5	1.3	1.6	
10/20/69	0.37	0.47	0.50	0.25	0.76	0.90	0.44	0.39	0.31	1.0	0.37	0.30	0.29	
10/24/69 <sup>d</sup>	0.20	0.22	0.15	0.15	0.18	0.21	0.25	0.27	0.19	0.20	0.25	0.19	0.18	
10/31/69 <sup>e</sup> (4 to 8 in. from floor)	0.06	0.06	0.08	0.05	0.58	0.55	0.32	0.22	0.25	0.37	0.28	0.30	0.10	

<sup>a</sup>Radiation readings were made 4 ft above floor, at window locations, except as noted in survey of 10/31/69.

<sup>b</sup>First survey; seven fuel elements still in cell.

<sup>c</sup>Halfway through remote cleanup; one fuel element still in cell.

<sup>d</sup>Completion of remote cleanup operations.

<sup>e</sup>Completion of direct cleanup operations.

No difficulties were encountered in decontaminating the cell surfaces to the levels of radioactivity indicated in the table. Because of the pyrometallurgical fuel-recovery process employed at EBR-II, these surfaces were easy to clean so that they were free of contamination. Since the contamination arising from the pyrometallurgical process is in the form of dry particulate which settles out on a surface, it does not become readily fixed and is readily susceptible to cleaning by the techniques used.

Equipment maintenance is in progress. Work on the crane and manipulator bridges and their respective busbars is almost complete. In general, the condition of this equipment was much better than expected. Maintenance and repair of the electromechanical manipulator carriages have been started. Concurrently with the maintenance work being done, electrical, instrument, and pneumatic services are being installed for new in-cell examination equipment.

## PUBLICATIONS

### Pumps for Sodium-Cooled Fast Breeder Reactors

R. C. Allen

Reactor Fuel-Process. Technol. 12(3), 264-278 (Summer 1969)

### Fault Propagation in an EBR-II Mark-II Driver-Fuel Subassembly

A. V. Campise

ANL-7560 (March 1969)

### Flow Properties of Suspensions with High Solids Concentration

E. C. Gay, P. A. Nelson, and W. P. Armstrong\*

AIChE Journal 15(6), 815-822 (Nov 1969)

### Study of Loading of EBR-II Electric Power System

H. Kacinskas

ANL/EBR-005\*\* (July 1969)

### Argonne Advanced Research Reactor Critical Experiments

K. E. Plumlee, J. W. Daughtry, T. W. Johnson, W. R. Robinson,

R. A. Schultz, and G. S. Stanford

ANL-7483 (Feb 1969)

### Conceptual System Design Description of the EBR-II In-core Instrument Test Facility

O. Seim, E. Hutter, T. Sullivan, R. Olp, J. Pardini, E. Filewicz, and R. Brubaker

ANL/EBR-004\*\* (June 1969)

---

\*Washington University.

\*\*One of a series of "blueback" topical reports prepared by the EBR-II Project.

Physicochemical Mechanics of Metals and Nuclear Reactors

F. A. Smith

Int. J. Nondestructive Testing 1, 237-249 (Nov 1969)

Some Observations on Phenomena Affecting Wear of Bearing Materials in Sliding Contact in Sodium and Argon at Temperatures up to 1200°F

E. S. Sowa, K. C. Tsao,\* C. Fiala, and C. J. Divona

ANL-7580 (July 1969)

Operation of a Pyrochemical Processing-Remote Refabrication Plant; the EBR-II Fuel Cycle Facility

C. E. Stevenson, M. J. Feldman, D. C. Hampson, D. M. Paige, and N. J. Swanson

Chem. Eng. Progr. Symp. Ser. 94, 65, 61-69 (1969)

The following appeared in Proc. 17th Conf. on Remote Systems Technology, Am. Nucl. Soc., San Francisco, November 1969:

Gastight Shielding Window Design for the Hot Fuel Examination Facility

T. W. Eckels and D. P. Mingesz

pp. 192-195

Containment Experience at the EBR-II Fuel Cycle Facility and Future Plans (Panel Discussion)

K. R. Ferguson

pp. 145-146

A Titanium Gettering System for Purification of Glove Box Atmospheres

M. L. Kyle, R. D. Pierce, and K. R. Tobias

pp. 185-191

Design of the Hot Fuel Examination Facility Argon System

E. W. Landow and P. R. Hirsch

pp. 196-200

Irradiation Tests of Hot Cell Lamps

R. A. Marbach

pp. 222-223

A Vertical Assembler-Dismantler for the Fuel Cycle Facility

W. L. Sales, D. L. Mitchell, J. R. White, and J. P. Simon\*\*

pp. 26-33

Preliminary Design of the Hot Fuel Examination Facility (HFEF)

N. J. Swanson, J. F. Lindberg, D. P. Mingesz, R. C. Watson, K. R. Ferguson, and J. R. White

pp. 131-140

---

\*The University of Wisconsin.

\*\*National Accelerator Laboratory.

## II. OTHER FAST REACTORS--OTHER FAST BREEDER REACTORS--FUEL DEVELOPMENT

### A. Irradiation Effects, Mechanical Properties and Fabrication

#### 1. Mechanical Properties of Type 316 Austenitic Stainless Steel (J. E. Tesk, S. D. Harkness, and R. Carlander)

Not previously reported.

Capsule AO3-D1, containing two concentric tubes of Type 316 austenitic stainless steel in an inert atmosphere of 90% argon and 10% helium, has been assembled and is planned for insertion into EBR-II as part of the Group O-3 experimental Subassembly XO72. The outer tube is from the same lot of tubing that was used to encapsulate the Group O-3 experimental fuel pins. The tube will serve as a standard for tube burst or tube rupture experiments that will be performed on the Group O-3 fuel pins after irradiation to ~10% burnup. This tube will receive nearly the identical neutron exposure as the fuel cladding at temperatures close to the fuel cladding temperatures. One important difference between the irradiation history of the fuel-pin cladding and the tube standard will be the lack of possible cesium penetration in the standard.

The inner tube serves as a susceptor to raise the temperature of the outer tube to the desired values. It is expected that information on free swelling at high temperatures (~500-650°C) will be available from the inner tube. Temperature and flux profiles are expected to be nearly symmetric with respect to the reactor midplane. Half of the inner tube has been cold worked to ~20% to investigate the effects of cold work on free swelling by comparison with swelling of the annealed half of the inner tube. Temperature and flux monitors have been installed inside the inner tube.

### III. GENERAL REACTOR TECHNOLOGY

#### A. Applied and Reactor Physics Development

##### 1. Theoretical Reactor Physics--Research and Development

###### a. Theoretical Reactor Physics

###### (i) Reactor Computation and Code Development (B. J. Toppel)

Last Reported: ANL-7577, p. 130 (April-May 1969).

(a) Spatial Flux Synthesis. A series of calculations have been run to test the performance of the SYNID code in a variety of situations.

In one set of test cases a cylindrical reactor, bare in the radial direction and with four material regions in the z-direction, was used. Moreover, cell boundary conditions were imposed in the r-direction. The flux is then separable and flat in the r-variable. The trial functions used were functions of r and were synthesized in the z-direction. Six energy groups were used. The physical situation selected is very simple, enough to allow clear-cut qualitative prediction of what the code should do, but permitting nevertheless to test the working of a variety of synthesis options.

The results were compared with the results obtained by codes using finite-difference techniques (DIFF2D). As can be appreciated from Table III.A.1, which summarizes the results, the synthesis variables (i.e., number of synthesis regions), location of synthesis region boundaries, and number and type of trial functions as a function of region and group were varied widely. The ability of the code to handle a variety of boundary conditions at the top and bottom of the reactor was also tested. The agreement in  $k_{\text{eff}}$  values was in general excellent. The fluxes in the r direction were flat to the sixth significant figure in all cases tested and agreed quite well with the comparison fluxes in the z-direction. The trial functions used were such that in all cases the exact solution could be reproduced. The trial functions have been named  $H_{gk}^n$  and  $H_{gk}^{*n}$ , with g for energy group, k for synthesis region and n for trial function number;  $\phi_g(z_k)$ ,  $\phi_g(z_L)$ ,  $\phi_g^*(z_k)$  or  $\phi_g^*(z_L)$  are fluxes and adjoints from a finite difference calculation at the mesh points k or L;  $\Delta k$  is the difference in k between synthesis and the finite-difference calculation.

Another set of calculations was run to test the ability of the code to handle different types of boundary conditions in the transverse coordinate direction, i.e., that coordinate over which the trial functions are defined. These tests used a square bare reactor with one set of

TABLE III.A.1. Summary of a Comparison of Synthesis (SYNID) and Finite-difference (DIFF2D) Calculations

No.	Number of Synthesis Regions	Region Boundaries (Mesh Point)	Left Boundary Condition	Right Boundary Condition	Trial Function Description	$\Delta k$
1	2	4	$\theta' = 0$	$\theta' + \frac{\theta}{20} = 0$	$H_{gk}^1 - H_{gk}^{+1} = 1$	$<10^{-6}$
2	4	1, 2, 5	*	*	$H_{gk}^1 - H_{gk}^{+1} = 1$	*
3	2	5	*	*	$H_{g1}^1 - H_{g1}^{+1} = 1$ $H_{g2}^1 - H_{g2}^{+1} = r$ $H_{g2}^2 - H_{g2}^{+2} = 1 - r$	*
4	2	5	*	*	$H_{g1}^1 - H_{g1}^{+1} = 1$ ; $H_{g2}^1 - H_{g2}^{+1} = r$ and $H_{g1}^1 - H_{g1}^{+1} = r$ ; $H_{g2}^1 - H_{g2}^{+1} = 1 - r$ $H_{g2}^2 - H_{g2}^{+2} = 1 - r$ for $g = 1, 2, 3$ and $H_{g2}^1 - H_{g2}^{+1} = 1$ for $g = 4, 5, 6$	*
5	2	5	*	*	$H_{gk}^1 - H_{gk}^{+1} = r$ , $H_{gk}^2 - H_{gk}^{+2} = 1 - r$ $g = 1, \dots, 6$ $k = 1, 2$	*
6	3	3, 5	*	*	$H_{g2}^1 - H_{g2}^{+1} = r$ , $H_{g2}^2 - H_{g2}^{+2} = r^2$ , $H_{g2}^3 - H_{g2}^{+3} = 1 - r - r^2$ all $g$ $H_{gk}^1 - H_{gk}^{+1}$ all $g$ , $k = 1, 3$	*
7	2	5	*	*	$H_{gk}^1 - 1$ , $H_{gk}^{+1} = 10$ all $g$ , $k = 1, 2$	*
8	2	5	*	*	$H_{gk}^1 = g + 2$ , $H_{gk}^{+1} = 1/(g+2)$ all $g$ , $k = 1, 2$	*
9	2	5	*	*	$H_{g1}^1 = g + 2$ , $H_{g1}^{+1} = 1/(g+2)$ $H_{g2}^1 = (g+2)^2$ , $H_{g2}^{+1} = 1/(g+2)^2$ all $g$	*
10	2	5	*	*	$H_{gk}^1 = r + 1$ , $H_{gk}^{+1} = r/2 - 1$ $H_{gk}^2 = -r$ , $H_{gk}^{+2} = 2 - r/2$ all $g$ , $k = 1, 2$	*
11	14	1, 2, ..., 13	*	*	$H_{gk}^1 - \theta_g(z_k)$ , $H_{gk}^{+1} - \theta_g^{+1}(z_k)$ all $g$ ; $z_k$ is $k$ th mesh point	*
12	4	1, 3, 6	*	*	$H_{gk}^1 - \theta_g(z_k)$ , $H_{gk}^{+1} - \theta_g^{+1}(z_k)$ all $g$ , and for $k = 1$ , $L = 1$ , for $k = 2$ , $L = 4$ , for $k = 3$ , $L = 7$ and for $k = 4$ , $L = 12$	*
13	14	1, 2, ..., 13	*	*	$H_{gk}^1 - H_{gk}^{+1} = \theta_g(z_k)$ all $g$ , all $k$	*
14	14	1, 2, ..., 13	*	*	$H_{gk}^1 - H_{gk}^{+1} = \theta_g^{+1}(z_k)$ all $g$ , all $k$	*
15	14	1, 2, ..., 13	*	*	$H_{gk}^1 - \theta_g^{+1}(z_k)$ , $H_{gk}^{+1} - \theta_g(z_k)$ , all $g$ , all $k$	*
16	3	3, 6	*	*	$H_{g2}^1 - H_{g2}^{+1} = r^1$ , $i = 1, 2, 3$ ; $H_{g2}^4 - H_{g2}^{+4} = 1 - r - r^2 - r^3$ all $g$ $H_{gk}^1 - H_{gk}^{+1} = 1$ all $g$ and $k = 1, 3$	*
17	3	3, 6	*	*	$H_{g2}^1 - H_{g2}^{+1} = r^1$ , $i = 1, 2, 3, 4$ , $H_{g2}^5 - H_{g2}^{+5} = 1 - r - r^2 - r^3 - r^4$ , all $g$ $H_{gk}^1 - H_{gk}^{+1} = 1$ all $g$ and $k = 1, 3$	*
18	3	3, 6	*	*	$H_{g2}^1 - H_{g2}^{+1} = r^1$ , $i = 1, 2, \dots, 5$ , $H_{g2}^6 - H_{g2}^{+6} = 1 - r - r^2 - r^3 - r^4 - r^5$ all $g$ $H_{gk}^1 - H_{gk}^{+1} = 1$ all $g$ and $k = 1, 3$	*
19	2	3	$\theta' = 0$	$\theta' = 0$	$H_{g1}^1 - H_{g1}^{+1} = 8r^2 - 8r + 1$ , $H_{g1}^2 - H_{g1}^{+2} = 10r^2 - 10r + 3$ , $H_{g1}^3 - H_{g1}^{+3} = 2r^2 - 2r + 1$ all $g$ $H_{g2}^1 = r + 1$ , $H_{g2}^{+1} = 5r - 5/2$ , $H_{g2}^2 = -r + 1$ , $H_{g2}^{+2} = -5r + 7/2$ all $g$	*
20	2	3	$\theta' = 0$	$\theta' = 0$	Same as in #19	*
21	2	3	$\theta' + \frac{1}{20} \theta = 0$	$\theta' = 0$	Same as in #19	*
22	2	3	$\theta' = 0$	$\theta' = 0$	Same as in #19	*
23	2	3	$\theta' = 0$	$\theta' = 0$	Same as in #19	*
24	2	3	$\theta' + \frac{1}{20} \theta = 0$	$\theta' = 0$	Same as in #19	*
25	2	3	$\theta' = 0$	$\theta' + \frac{1}{20} \theta = 0$	Same as in #19	*
26	2	3	$\theta' = 0$	$\theta' + \frac{1}{20} \theta = 0$	Same as in #19	*
27	2	3	$\theta' + \frac{1}{20} \theta = 0$	$\theta' + \frac{1}{20} \theta = 0$	Same as in #19	*

fixed boundary conditions at the extremes of the x-coordinate ( $\phi' = 0$  at the left, and  $\phi = 0$  on the right). Three different reference cases were run for this geometry using DIFF2D which differ only in the boundary conditions imposed at the y-coordinate extremes. The values of  $k_{\text{eff}}$  obtained for the three reference runs are the following:

$$\left. \begin{array}{ll} k = 0.58643 & \phi_g = 0 \\ k = 1.21046 & \phi'_g = 0; g = 1, 2, \dots, 6 \\ k = 0.68424 & D_g \phi'_g + a \phi_g = 0 \end{array} \right\} \text{at both y-coordinate boundaries}$$

The synthesis calculations used as trial functions y-dependent flux profiles from these reference runs. Trial function number one comes from the reference case with  $\phi_g = 0$  conditions in the y-direction, number two from the case with  $\phi'_g = 0$  conditions, and number three from the remaining case with  $D_g \phi'_g + a \phi_g = 0$  conditions.

By means of input parameters\* the user decides which boundary conditions should be implicitly imposed by the variational functional in the y-direction. The code then should proceed to select or combine the trial functions accordingly.

Table III.A.2 summarizes the results of the tests up to now. Five synthesis calculations were performed in each basic case considered: with the exact trial function for the case (Runs 1, 6, 11); with the exact trial function and one of the others (Runs 2, 4, 8, 9, 12, 13); with two functions, excluding the exact one (Runs 3, 7, 14); with three trial functions (Runs 5, 10, 15).

TABLE III.A.2. Boundary Condition Test

No.	Boundary Conditions	Trial Function 1	Trial Function 2	Trial Function 3	k	$\Delta k$	$R_1$	$R_2$	Observations
1	$\phi' = 0$	No	Yes	No	1.210463	$\sim 10^{-8}$	-	-	
2	$\phi' = 0$	Yes	Yes	No	1.210463	$\sim 10^{-8}$	$\sim 10^{14}$	-	
3	$\phi' = 0$	Yes	No	Yes	1.192213	$1.8 \times 10^{-2}$	-	-	Two inexact trial functions
4	$\phi' = 0$	No	Yes	Yes	1.210463	$\sim 10^{-8}$	$\sim 10^{14}$	-	
5	$\phi' = 0$	Yes	Yes	Yes	1.210463	$\sim 10^{-8}$	$\sim 10^{10}$	$\sim 10^{10}$	
6	$D\phi' + a\phi = 0$	No	No	Yes	0.683971	$\sim 2.7 \times 10^{-4}$	-	-	
7	$D\phi' + a\phi = 0$	Yes	Yes	No	0.683633	$6.1 \times 10^{-4}$	-	-	Two inexact trial functions
8	$D\phi' + a\phi = 0$	Yes	No	Yes	0.683972	$2.7 \times 10^{-4}$	$\sim 2 \times 10^2$	-	
9	$D\phi' + a\phi = 0$	No	Yes	Yes	0.683973	$2.7 \times 10^{-4}$	$\sim 1 \times 10^3$	-	
10	$D\phi' + a\phi = 0$	Yes	Yes	Yes	0.683973	$2.7 \times 10^{-4}$	$\sim 1 \times 10^2$	$1 \times 10^2$	
11	$\phi = 0$	Yes	No	No	0.586208	$2.2 \times 10^{-4}$	-	-	
12	$\phi = 0$	Yes	Yes	No	gross errors	-	-	-	
13	$\phi = 0$	Yes	No	Yes	gross errors	-	-	-	
14	$\phi = 0$	No	Yes	Yes	gross errors	-	-	-	
15	$\phi = 0$	Yes	Yes	Yes	0.586128	$3.1 \times 10^{-4}$	$\sim 1 \times 10^2$	$\sim 1 \times 10^1$	

\*Luco, V., Boundary Conditions in Variational Flux Synthesis, ANL-7510 (1969).



Two synthesis regions were defined, but the same set was used in both. When using the exact trial function alone the result should be exact in  $k$  and in the fluxes. This is not so for boundary conditions other than  $\phi' = 0$ , due to discrepancies in the numerical treatment between DIFF2D and SYN1D.

In those cases when the exact trial function is among the set used, the code should reject the others. The parameters  $R_1$  and  $R_2$  in the table are a measure of this rejection. They are defined as typical values of the ratio of mixing function for exact solution over mixing function for the nonexact functions.

The cases for  $\phi_g = 0$  with two trial functions gave grossly mistaken results, and the amount of rejection in Case 15 with three trial functions is perhaps too low. These difficulties are presently under study.

Runs 3 and 7 are interesting. Here the code was able to combine two clearly inappropriate functions in such a way as to give small errors in  $k$  and fairly acceptable fluxes.

## 2. Nuclear Data--Research and Development

### a. Determination of Nuclear Constants

#### (i) Fast-neutron Cross Sections and Other Nuclear Constants (A. B. Smith)

Last Reported: ANL-7581, pp.\*87-88 (June 1969).

(a) Fast-neutron Total and Scattering Cross Sections of Bismuth.\* Total neutron cross sections of bismuth have been measured with resolutions of  $\approx 1$  keV over the energy range from 0.2 to 1.4 MeV. Differential elastic-scattering cross sections were also determined at intervals of  $< 50$  keV from 0.3 to 1.5 MeV with resolutions of  $\sim 20$  keV (see Fig. III.A.1). The inelastic neutron excitation of a state at  $896 \pm 1$  keV was

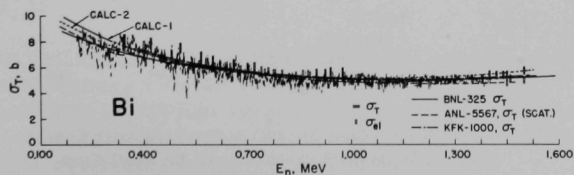


Fig. III.A.1. The Total Neutron and Differential Elastic-scattering Cross Sections of Bismuth

\*This work was in cooperation with the staff of the Pelindaba Laboratory South African Atomic Energy Board, Transvaal, Republic of South Africa.

observed and the respective differential excitation cross sections determined with incident resolutions of  $\approx 10$  keV. Partially resolved resonance structure was evident in all the measured values. The experimental results were assayed for possible intermediate structure, and were compared with the results of optical model and statistical calculations. The model calculations were cognizant of the fluctuation and correlation of compound-nucleus resonance widths and of the shell closure at  $N = 126$ .

(b) Investigation of Low-excitation States in  $^{75}\text{As}$  by the  $^{75}\text{As}(n,n'\gamma)$  Reactions. The energies and relative intensities of gamma rays produced by the inelastic scattering of monoenergetic neutrons from an arsenic sample were measured at several incident-neutron energies below 1500 keV with a 7.2-cm<sup>3</sup> Ge(Li) detector placed at 90° to the incident neutron beam. Background measurements were also made at each neutron energy using a carbon scatterer in place of the arsenic sample. Shielding and fast-coincidence circuitry were employed to reduce background problems. The gated pulse-height spectra were recorded in a 512-channel analyzer. Protons from a pulsed Van de Graaff accelerator were bunched by a Mobley magnet and focused on a target of lithium evaporated onto a tantalum backing to produce nanosecond bursts of neutrons via the  $^7\text{Li}(p,n)^7\text{Be}$  reaction. A level scheme for  $^{75}\text{As}$  has been deduced from the observed transitions, and has been compared with results from Coulomb-excitation measurements of  $^{75}\text{As}^*$  and studies of the decay of  $^{75}\text{Se}^{**}$  and  $^{75}\text{Ge}^\dagger$ .

This work represents the initial results of a comprehensive study of  $(n,n'\gamma)$  processes.

(c) Fast Neutrons Incident on Holmium. Total neutron, elastic- and inelastic-scattering cross sections of natural holmium were studied (see Fig. III.A.2). The total neutron cross sections were measured from 0.1 to 1.5 MeV with resolutions of  $< 5$  keV and precisions of  $\sim 1\%$ . Differential elastic- and inelastic-scattering cross sections were determined

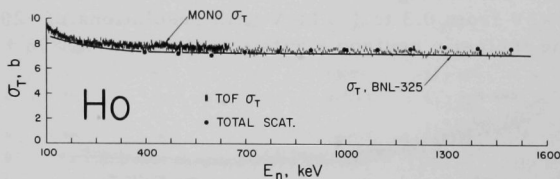


Fig. III.A.2. Total Neutron Cross Section and Total Scattering Cross Section for Holmium Compared with the Total Cross Section Determined by Time-of-flight Measurement

\*Robinson, R. L., *et al.*, Nucl. Phys. **A104**, 401 (1967).

\*\*Raeside, D. E., *et al.*, Nucl. Phys. **A130**, 677 (1969).

†Ng, Anne, *et al.*, Phys. Rev. **176**, 1329 (1968).

for incident neutron energies of 0.3 to 1.5 MeV. The inelastic neutron excitation of 14 states in holmium was observed and the respective cross sections measured. The experimental results have been considered in the context of: the optical model, direct reaction processes, statistical concepts, particularly with respect to fluctuations and correlations in compound-nucleus resonance structure, and in terms of the unified nuclear model.\*

This study is particularly of interest in the context of scattering from heavy deformed nuclei. The fissile, fertile, and heavy fission-product nuclei have such characteristic deformation.

b. Reactor Code Center (M. Butler)

Last Reported: ANL-7632, pp. 102-103 (Oct 1969).

Three code-conversion routines were prepared to permit the Center to process tapes containing program contributions received from General Electric Advanced Products Operation and Knolls Atomic Power Laboratory. These routines translate into BCD (binary-coded-decimal) from GE IMCV code, CDC display code, or the UNIVAC field-data character set.

In addition, five programs were incorporated into the library. Two of these were revisions replacing the existing FLANGE-1 and GASKET programs (ACC Nos. 247 and 263, respectively). Gulf General Atomic supplied these UNIVAC 1108 versions, which are programmed in FORTRAN V. The documentation for the new FLANGE-1, which, like its predecessor, computes neutron-scattering kernels for a large class of moderators from the scattering law determined by GASKET, is not yet available. The new version of GASKET includes the option selecting the diffusive or Brownian motion mode rather than the free-gas mode.

The three new programs assimilated include the KAPL DATATRAN System designed for the CDC-6600 (ACC No. 386), the ORNL CITATION program written for the IBM-360 (ACC No. 387), and the Japan Atomic Energy Research Institute EPSILON code for the IBM-7090 (ENEA No. E171).

DATATRAN is a data-handling language developed for the KAPL modular system of large related reactor computer programs. It is written in the FORTRAN and COMPASS languages, and the current distribution is by means of a CDC EDITSYM file with a small BCD modification package. In this form it is restricted to use on a 6600 system.

CITATION is a nuclear reactor core analysis code for one to three spatial dimensions. It is designed for use on either an IBM 360/91

---

\* Mottelson, B., and Nilsson, S., Kgl. Danske Vidensk. Selsk. Mat.-fys. Skr. 1, No. 8 (1959).

or an IBM 360/75 with bulk core storage. A minimum of 300,000 directly addressable words of memory is required for program execution.

The Japanese code EPSILON was written in FORTRAN 2 to compute fast-fission effects in multiregion lattices of cylindrical rods and slabs by the collision probability method. A maximum of 100 energy groups is permitted.

## B. Reactor Fuels and Materials Development

### 1. Fuels and Claddings--Research and Development

#### a. Behavior of Reactor Materials

##### (i) Experimental Studies of Swelling Mechanisms and Gas Release in Fuel Materials

##### (a) Interactions between Gas Bubbles and Moving Grain Boundaries (S. R. Pati)

Last Reported: ANL-7606, p. 92 (Aug 1969).

Interaction between grain boundaries and gas bubbles plays an important role in the nucleation, coalescence, and subsequent migration behavior of gas bubbles and voids in fuel materials. In metallic and carbide fuels, in particular, it is expected that the interaction between moving grain boundaries and inert-gas bubbles has a strong influence on the rate of fission-gas release because of the relatively small thermal gradient in these fuels during irradiation. Work on the interaction between moving grain boundaries and helium bubbles in single crystals of copper has shown that the interaction is strong enough to cause sweeping of the gas bubbles by the moving grain boundaries. Sweeping measurements have

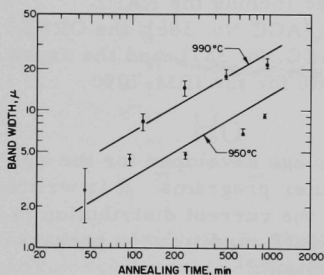


Fig. III.B.1

Variation in the Bubble-free Band Width as a Function of Annealing Time at the Annealing Temperatures

been completed at two annealing temperatures, 950 and 990°C. Details of the experimental technique have been described in ANL-7606. Figure III.B.1 shows the effect of annealing time on the width of the bubble-free region behind the moving grain boundary at each annealing temperature. The points in Fig. III.B.1 have been connected by solid lines with a slope of 1/2, which suggests that the bubble-free band width  $x$  increases with time  $t$  as

$$x^2 = At,$$

where  $A$  is a constant. It is evident from the experimental points that appreciable deviation

from the assumed parabolic time dependence occurs, especially at longer annealing times. This discrepancy could arise from the coarsening of helium bubbles on the grain boundaries.

A parabolic dependence of swept band width with annealing time has been observed in the dragging of oxide inclusions through a metal matrix;\* the same kinetics might be expected for inert-gas-bubble dragging. Additional experimental data are necessary to establish the time dependence more precisely. The kinetics of bubble dragging are being studied at other annealing temperatures in order to determine the activation energy associated with the dragging process and to establish the dragging mechanism.

(b) Thermal-gradient Migration of Bubbles and Pores  
(D. R. O'Boyle)

(1) Surface Diffusion in Uranium Dioxide  
(P. W. Maiya)

Not previously reported.

Surface-diffusion studies have been initiated on single crystals of  $\text{UO}_2$  grown by a floating zone technique.\*\* Three specimens (~7 by 7 by 7 mm) were prepared from a large crystal, with two parallel surfaces oriented parallel to the (100), (110), and (111) planes. The surfaces, determined by X-ray back-reflection techniques, were within  $\pm 1^\circ$  from the specified orientations, and the X-ray diffraction spots indicated a high degree of crystal perfection. The analysis of a specimen indicated that the concentrations of hydrogen, carbon, nitrogen, and oxygen were 19, 12, 11 ppm, and 11.97 wt %, respectively.

A series of sinusoidal profiles of periodicity ranging from 5 to 40  $\mu$  were produced on the polished crystal surfaces by a photoetching technique.† Briefly, the method consists of forming an image of a diffraction-grating replica on a crystal surface coated with a thin layer of photoresist-emulsion, followed by selective etching. Satisfactory etching of sinusoidal profiles on  $\text{UO}_2$  was accomplished by using a solution described by Manley.†† The rate of dissolution of  $\text{UO}_2$  was approximately 2  $\mu/\text{min}$  while the crystal was stationary in the solution. Etching times were typically on the order of 15-45 sec.

It should be noted that the initial as-etched profile need not be purely sinusoidal, since the profile assumes the sinusoidal shape

\*Ashby, M. F., and Centamore, R. M. A., The Dragging of Small Oxide Particles by Migrating Grain Boundaries in Copper, *Acta Met.* **16**, 1081 (1968).

\*\*Obtained from G. W. Clark and J. C. Wilson, Oak Ridge National Laboratory.

†Maiya, P. S., and Blakely, J. M., *Appl. Phys. Letters* **7**, 60 (1965).

††Manley, A. J., *J. Nucl. Mater.* **15**, 143 (1965).

at elevated temperatures due to the rapid decay of harmonics above the fundamental. A typical sinusoidal profile produced on the (100) plane of  $\text{UO}_2$  is shown in Fig. III.B.2. The amplitude of the sinusoidal profile decreased exponentially with time during the isothermal annealing treatment, in accordance with the theory of surface smoothing developed by Mullins.\* The surface-diffusion coefficient is determined from the relaxation times associated with the decay of the sinusoidal profiles. The effect of profile spacing on the relaxation process is being investigated on the low-index planes of  $\text{UO}_2$  in order to obtain quantitative information on the anisotropy of surface diffusivity and surface free energy in the temperature range from 1600 to 2100°C.

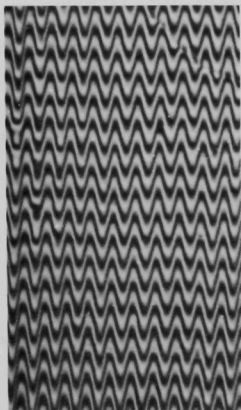


Fig. III.B.2

Sinusoidal Surface Profile on the (100) Plane of  $\text{UO}_2$ , 7.86- $\mu$  Wavelength. Specimen was annealed at 1660°C for 16 hr in a helium atmosphere (one fringe corresponds to a change in height of 0.27  $\mu$ ).

(c) Development of Temperature-gradient Vacuum Furnace (R. O. Meyer)

Not previously reported.

A program has been initiated to obtain measurements out of pile in order to determine migration of gas bubbles in steep temperature gradients. These measurements require special high-temperature equipment that is not commercially available; in particular, the success of this thermomigration program depends upon designing a good temperature-gradient vacuum furnace. An apparatus capable of producing very steep temperature gradients will be described.

An initial survey of a number of thermal-gradient furnaces described in the literature and inspection of two designs revealed several problem areas. First, the ability to achieve temperature rapidly is desirable because gas bubbles move very rapidly (up to several thousand angstroms per second in gradients of 1000°C/cm) and, therefore, short anneals may be required. Resistance heating does not appear to give adequate heating rates. Errors as large as 25% were reported by Weaver\*\* because he was unable to heat specimens to temperature rapidly. Second, molybdenum from furnace parts has caused the downfall of several diffusion experiments in  $\text{UN}^\dagger$  and  $\text{Ni}^\ddagger$  and both of these materials are likely to find their way into our apparatus. Finally, sufficient total power must be

\*Mullins, W. W., "Solid Surface Morphologies Governed by Capillarity," Metal Surfaces: Structure, Energetics, and Kinetics, American Society for Metals (1963).

\*\* Weaver, S. C., ORNL-TM-2016 (1967).

$^\dagger$  Reimann, D. K., Oak Ridge National Laboratory, private communication.

$^\ddagger$  Mock, Willis, Jr., Thesis, University of Illinois (1968).



available. It was possible to estimate that Weaver's and Mock's heat losses were between 400 and 800 W in excess of heat flow through their specimens. For 3/8-in.-dia  $\text{UO}_2$  in a gradient of  $1000^\circ\text{C}/\text{cm}$ , this heat flow is only  $\sim 20$  W. For a good conductor, such as copper, it is about 2.5 kW.

With these considerations in mind, power from an rf induction generator was chosen. Induction heating has the advantage of generating heat in the part desired (the tungsten heat conductor discussed later) without the necessity of heat transfer from a resistance-heated element. By virtue of this property, the heating process is very rapid. A 5-kW unit was selected as the smallest size practical. Molybdenum was not used for any furnace parts in order to avoid sample contamination. Several design considerations were found to be critical. Close rf coupling to the tungsten heat conductor was necessary. A loosely wound, 4-turn coil was completely inadequate, but our tightly wound, 10-turn coil with a 1/8-in. gap works quite well. Also, the  $\text{Al}_2\text{O}_3$  insulating cylinder between the coil and the tungsten heat conductor not only keeps the copper coil clean, but also reduces total heat loss by more than a factor of two by reducing heat transfer to the water-cooled copper coil.

During initial tests of the apparatus, the highest gradient achieved was  $1600^\circ\text{C}/\text{cm}$  in Type 304 stainless steel. Stainless steel (thermal conductivity  $k = 0.24$  W/cm- $^\circ\text{C}$ ) requires greater heat flow for a given gradient than does  $\text{UO}_2$  ( $k = 0.030$  W/cm- $^\circ\text{C}$ ) and, therefore, provides a better test than an insulator would. This gradient was measured with two Pt-Rh alloy thermocouples threaded through small holes in the stainless steel. The hottest end of this stainless steel specimen was about  $1285^\circ\text{C}$ , and the rf generator power setting was 50%.

High-temperature operation has been tested using  $\text{Al}_2\text{O}_3$  samples ( $k = 0.086$  W/cm- $^\circ\text{C}$ ). The maximum furnace temperature (temperature in tungsten heat conductor) achieved to date has been approximately  $1800^\circ\text{C}$  with a power setting of 70%. Higher temperatures were not attempted due to thermocouple failure around  $1800^\circ\text{C}$ .

The tests achieving a furnace temperature of  $1800^\circ\text{C}$  and a gradient of  $1600^\circ\text{C}/\text{cm}$  do not demonstrate the maximum capability of the apparatus. They do demonstrate the ability to perform the experiments that are planned.

With the  $\text{Al}_2\text{O}_3$  samples, heat flow by conduction through the  $\text{Al}_2\text{O}_3$  was always small ( $<100$  W). Neglecting this flow, heat loss in the furnace was primarily due to radiation from the tungsten heat conductor. This heat loss is a fundamental property of the furnace and can be measured from cooling curves (temperature versus time). The rate of heat loss can be written as

$$\frac{dQ}{dt} = \frac{dQ}{dT} \frac{dT}{dt}$$



where  $dT/dt$  is obtained from the cooling curve, and for 1 g of material

$$\frac{dQ}{dT} = c,$$

where  $c$  is the specific heat. Thus, the rate of heat loss from the tungsten heat conductor of mass  $m$  is

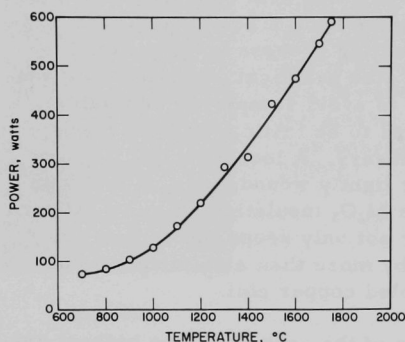


Fig. III.B.3. Furnace Heat Loss (excluding conduction through sample) vs Temperature of Tungsten Heat Conductor

$$\frac{dQ}{dt} = mc \frac{dT}{dt}.$$

Figure III.B.3 shows the averaged result of such calculations for seven cooling curves starting at various temperatures between 1000 and 1750°C. The power required to operate the furnace at a given temperature and producing a given gradient in a sample will be given by the sum of a number from this graph and the heat flux through the sample. Heat losses (see Fig. III.B.3) are about as expected, i.e., 400-800 W at high temperatures.

It is planned to begin studies on the migration of sinter pores in

UO<sub>2</sub> in the near future and to follow with studies of the migration of cyclotron-injected helium gas bubbles in UO<sub>2</sub>.

(d) Solid-fission-product Swelling (A. E. Dwight and D. R. O'Boyle)

Last Reported: ANL-7606, pp. 94-95 (Aug 1969).

Previous work (see Progress Report for April-May 1969, ANL-7577, pp. 143-144) has shown that the crystal structure of the white metallic inclusions formed in mixed-oxide fuel irradiated in a fast-neutron flux is hexagonal, based upon the Mo-Rh epsilon phase. Subsequent work indicated complete solid solubility between the  $\epsilon$  phase and ruthenium as well as the extent of the  $\epsilon$  phase in the Mo-Ru-Rh ternary system at 20 and 40 at. % ruthenium. Data were obtained by X-ray diffraction of arc-melted alloys annealed at 1140°C.

X-ray diffraction studies of additional alloys have resulted in an isothermal section (1140°C) through the Mo-Ru-Rh system (see Fig. III.B.4). The circles represent the compositions of the alloys examined. The single phase  $\epsilon$  field and the two-phase Mo +  $\epsilon$  field occupy the largest part of the diagram. The extensive composition range

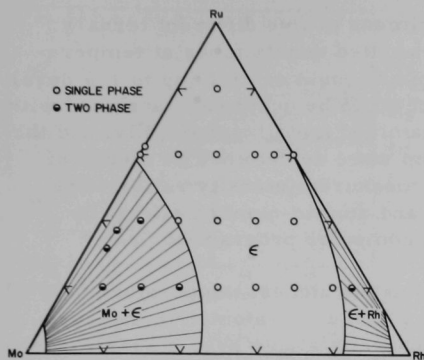


Fig. III.B.4. Mo-Ru-Rh Isotherm at 1140°C

Mo, Tc, Ru, Rh, and Pd. However, in a hyperstoichiometric fuel system, the excess oxygen is expected to oxidize all of the molybdenum to  $\text{MoO}_2$  so that none is available to alloy with the Tc, Ru, Rh, and Pd. Rand and Markin\*\* have estimated that the critical stoichiometries for the initial and total oxidation of molybdenum to  $\text{MoO}_2$  are 1.957 and 1.985, respectively. Referring to Fig. III.B.4, these two conditions correspond to the average composition of the metallic fission-product phase that lies near the  $\epsilon$  side of the Mo +  $\epsilon$  two-phase field, and to the composition of the fission-product phase that lies along the Ru-Rh side of the ternary system near 10 wt % rhodium. Thus, over almost the entire range of fuel stoichiometries in mixed-oxide fuel, the second long-period fission-product elements will form a close-packed hexagonal phase ( $\epsilon$  in Fig. III.B.4). The second phase that may also form is bcc molybdenum with a small amount of ruthenium and rhodium in solid solution.

## (ii) Metallic Fuel

### (a) Phase Studies (D. R. O'Boyle)

Not previously reported.

To establish the phases in equilibrium in the uranium corner of the uranium-plutonium-zirconium system, a series of high-purity binary uranium-plutonium and ternary uranium-plutonium-zirconium alloys that have a plutonium-to-uranium ratio of 1:4 were prepared by arc melting the pure elements. Following homogenization at approximately 1000°C in

of the  $\epsilon$  phase and the work of Darby et al.\* indicate that the  $\epsilon$  phase should exhibit solubility for small amounts of technetium and palladium, as has been observed.

The amount of fission-product molybdenum that is available as an alloying element to form inclusions in mixed-oxide fuel varies with the stoichiometry of the fuel. In a hypo-stoichiometric oxide system, none of the molybdenum is expected to be oxidized to  $\text{MoO}_2$  and the molybdenum content of the inclusions will be about 45 wt % based on the fission yield of

\*Darby, J. B., Lam, D. J., Norton, L. J., and Downey, J. W., Intermediate Phases in Binary Systems of Technetium-99 with Several Transition Elements, J. Less-Common Metals 4, 558-563 (1962).

\*\*Rand, M. H., and Markin, T. L., Some Thermodynamic Aspects of (U,Pu)O<sub>2</sub> Solid Solutions and Their Use as Nuclear Fuels, Proc. Vienna Symp., Thermodynamics of Nuclear Materials (1967).

the gamma single-phase region, 27 specimens of five different ternary alloys were isothermally annealed in evacuated quartz tubes at temperatures between 590 and 700°C for a sufficient length of time (up to 170 days) to allow the phases to grow to a size that could be accurately analyzed with the microprobe. Each specimen was examined metallographically, and the compositions of the phases in equilibrium were determined by means of point counts and mechanical scans. All measured intensity ratios were corrected for absorption, fluorescence, and atomic-number effects by using a modified version of the Magic II computer program of Gray.\*

The alloys annealed at the highest temperature (700°C) were found to contain only the bcc gamma phase. Dilatometric measurements have established that the gamma phase is stable over a wide range of temperatures up to approximately 1100°C. Figure III.B.5 shows that the gamma solvus temperature decreases rapidly near the U-Zr and U-Pu binary sides of the system, sweeps rapidly over the central part of the system, and then pulls back to the plutonium corner. The open circles represent the compositions of the gamma phase, as determined by microprobe analysis.

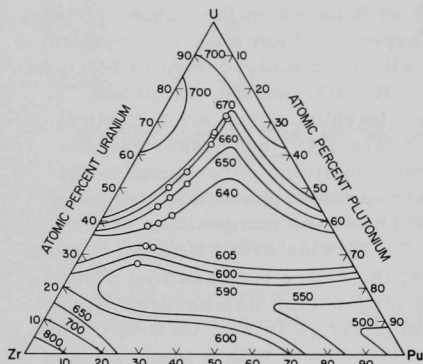


Fig. III.B.5. Uranium-Plutonium-Zirconium  
Gamma-phase Solid Solution De-  
composition Temperatures

Alloys annealed in the temperature range from 590 to 670°C were generally two-phase and consisted of zeta-uranium-plutonium and gamma. The extent of the zeta and gamma single-phase regions is shown in the isopleth through the ternary system (see Fig. III.B.6).

An impurity phase commonly observed in commercial-purity uranium-plutonium-zirconium alloys was previously identified as oxygen-stabilized alpha zirconium that contains some uranium and plutonium in solid solution. The solid solubility of uranium and plutonium in the alpha-zirconium phase was measured in alloys annealed at temperatures between 350 and 1100°C (see Fig. III.B.7). The maximum solid solubility over this temperature range is 3.8 wt % for uranium and 2.4 wt % for plutonium.

\*Gray, L. J., X-ray Mass Absorption Coefficients and Quantitative Microanalysis of Metallurgical Systems, Including Refractory Metal-Interstitial Compounds, Ph.D. Thesis, University of Illinois (1969).

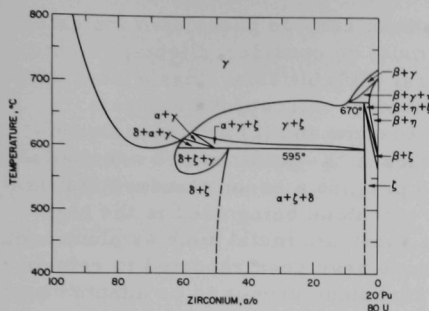


Fig. III.B.6. Section through the Uranium-Plutonium-Zirconium Ternary System at Pu/U = 1/4. Phases in equilibrium studied in alloys with <60 at. % zirconium.

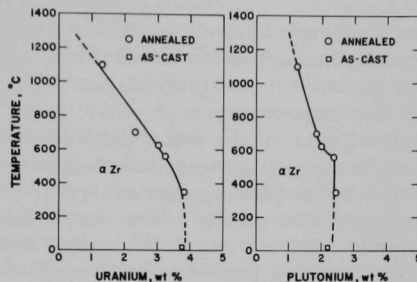


Fig. III.B.7. Solid Solubility of Uranium and Plutonium in Oxygen-stabilized Alpha Zirconium

## b. Chemistry of Irradiated Fuels (C. E. Crouthamel)

### (i) Postirradiation Studies of Reactor Fuels and Cladding

Last Reported: ANL-7606, pp. 96-97 (Aug 1969).

Electron microprobe studies of two vibratorily compacted uranium-plutonium carbide fuel pins (UC-20 wt % PuC) are continuing. One of the fuel pins (SMV-1) was clad with Type 316 stainless steel and had been irradiated in EBR-II to 2.6 at. % burnup; the second pin (SMV-2) was clad with Type 304 stainless steel and had been irradiated in EBR-II to 6.9 at. % burnup. The fuel-cladding interactions observed in both fuel pins were discussed previously (see ANL-7606).

Both the UC and PuC fractions of the original fuel material were hyperstoichiometric, the UC containing UC<sub>2</sub> and the PuC containing Pu<sub>2</sub>C<sub>3</sub>. The average particle size of the PuC was <44 μm and that of the UC was 500-1700 μm. Postirradiation metallographic examination showed that the physical characteristics of the fuel material had not been altered appreciably during irradiation: the UC was present as large, discrete particles, and the PuC as a finely divided, porous material.

Preliminary studies have been conducted to determine the distribution of fission products in the SMV-2 fuel pin. Spectral profiles taken of the homogeneous uranium carbide particles revealed detectable quantities of zirconium and molybdenum. Typical particles (average size, ~700 μm) located near the center and periphery of the fuel were examined for these elements. No concentration difference was observed for either elements as a function of (1) location within a given particle or (2) location of the particle within the fuel pin.

Examination of the uranium carbide phase also indicated the presence of xenon, but this finding must be considered tentative until further confirmation is obtained. Several difficulties are associated with the positive identification of xenon by electron microprobe analysis: (1) the concentration of xenon in the fuel is low and (2) accurate experimental data on the wavelength of the xenon L X-ray lines are not available. At present, an attempt is being made to prepare a xenon standard that is suitable for microprobe analysis. The technique being used is the high-energy impaction of xenon atoms into a substrate metal such as aluminum. (Xenon samples prepared by this technique have been reported to remain fixed for long periods of time.) If this technique proves to be adaptable to microprobe studies, it should provide a means of establishing accurate values for the wavelengths of the xenon L X-ray lines.

Spectral analysis of the porous plutonium carbide phase indicated the presence of neodymium, palladium, and cesium. The cesium was observed throughout the plutonium carbide in localized concentrations. This is in contrast to the behavior of cesium in oxide fuels, where cesium is found primarily in the cooler zones (i.e., near the cladding) of the fuel.

Further studies of the distribution of fission products in the carbide fuels are in progress.

#### c. Thermodynamics of Fuel Materials

- (i) Total Vapor Pressures and Carbon Potentials in the Ternary U-C-Pu System (P. E. Blackburn and M. Tetenbaum)

Last Reported: ANL-7606, pp. 97-98 (Aug 1969).

The study of the vaporization behavior of the uranium-carbon system is continuing. Measurements of the total pressure of uranium-bearing species and carbon activity are being made as a function of temperature and  $UC_x$  compositions, using the transpiration method with hydrogen-methane mixtures as carrier gases. Emphasis has been placed on measuring carbon activities in the uranium-carbon system; these measurements will ultimately be extended to plutonium carbides. Plans are also in progress to investigate the effect of oxygen contamination in the U-C system; in particular, the influence of oxygen on carbon activity will be investigated.

Estimates of the activity of uranium at various  $UC_x$  compositions can be made from  $\Delta\bar{G}_U$  values derived from our carbon activity measurements (see Progress Report for April-May 1969, ANL-7577, pp. 149-151) and the application of the Gibbs-Duhem equation in the form

$$\Delta \bar{G}_U(UC_x) - \Delta \bar{G}_U(UC_{1.00}) = - \int_{\Delta \bar{G}_C(UC_{1.00})}^{\Delta \bar{G}_C(UC_x)} \frac{N_C}{N_U} d\Delta \bar{G}_C.$$

The standard free energy of formation of  $UC_{1.00}$  was estimated from the heat of formation of  $UC_{1.00}$  and the appropriate free energy functions.

For  $\Delta H_{298}^\circ(UC_{1.00})$ , we used the recent value of  $-23.2 \pm 1$  kcal/mol obtained by Storms and Huber\* by means of combustion calorimetry. The results are summarized in Fig. III.B.8. In general, the calculated uranium activity values are in good agreement with values based on Storms\*\* adjusted vapor pressure values for  $UC_x$  and 126.3 kcal/mol as the heat of vaporization of uranium.†

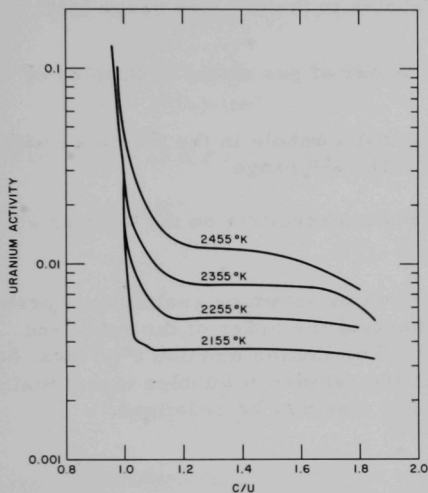


Fig. III.B.8. Uranium Activities Derived from Gibbs-Duhem Integration of Carbon Activity

It should be noted that the shapes of the calculated curves shown in Fig. III.B.8 are consistent with expectations, namely, a sharp increase in uranium activity near the stoichiometric composition as the composition of the condensed phase is reduced toward the lower phase boundary,  $U(\ell) + UC(s)$ , in the hypostoichiometric region.

#### d. Oxide Fuel Studies

##### (i) Oxide-fuel Swelling Mechanisms and Models (R. B. Poeppel)

Last Reported: ANL-7595, pp. 91-92 (July 1969).

A rigorous derivation of the counting procedure previously described has been developed. The counting procedure uses the formula

$$\sum_{s=1}^n f(n)f(s) \times N_{av}(s) \times P(s,n)/[N_{av}(n+1) - N_{av}(n)] \quad (1)$$

\*Storms, E. K., and Huber, E. J., J. Nucl. Mater. **23**, 19 (1967).

\*\*Storms, E. K., The Refractory Carbides, Academic Press, New York, New York (1967), Ch. XI, p. 205.

†Ackermann, R. J., and Rauh, E. G., J. Phys. Chem. **73**, 769 (1969).



for the rate of growth of fission-gas bubbles from the size range  $(n)^{\text{th}}$  to the  $(n+1)^{\text{th}}$ , where

$n^{\text{th}}$  size range is defined as all bubbles that contain between  $m^{n-1}$  and  $m^n - 1$  inclusive gas atoms;

$m$  is an integer  $>2$ ;

$f(n)$  is the number of bubbles in the  $n^{\text{th}}$  size range (per unit mass of fuel);

$N_{\text{av}}(n)$  is the average number of gas atoms in bubbles of the  $n^{\text{th}}$  range;

$P(s,n)$  is the probability that a bubble in the  $n^{\text{th}}$  range will coalesce with a bubble in the  $s^{\text{th}}$  range.

The formula was derived using a conservation condition on the number of gas atoms.

Equation (1) may be derived by summing coalescence probability over all pairs of bubbles, interchanging the order of the sums and making appropriate approximations. The distribution function  $f^*(i)$  must be defined on the bubble size space;  $f^*(i)$  is the number of bubbles that contain  $i$  gas atoms. The functions  $f(n)$  and  $N_{\text{av}}(n)$  may now be redefined:

$$f(n) \equiv \sum_{i=m^{n-1}}^{m^n-1} f^*(i) \quad (2)$$

and

$$N_{\text{av}}(n) \equiv \sum_{i=m^{n-1}}^{m^n-1} if^*(i)/f(n). \quad (3)$$

These definitions are consistent with the verbal ones used above.

If  $j$  is the size of a gas bubble in the  $(n-1)^{\text{th}}$  range, then coalescence of a bubble of size  $i$  with one of size  $j-i$ , where  $i$  and  $j-i$  are both less than  $m^n$ , will produce a new bubble in the  $(n+1)^{\text{th}}$  range. The total number of bubbles produced of size  $j$  is determined by summing the coalescence probability  $P(i, j-i)$  over all such pairs. Each pair must be counted only once, and the summations are different depending on whether  $j$  is odd or even.

Since  $m^n - 1$  is the size of the largest bubble not in the  $(n+1)^{\text{th}}$  range, the largest  $j$  considered is  $2(m^n - 1)$ . The total number of



bubbles growing into the  $(n+1)$ th range is obtained by summing over  $j$  from  $m^n$  to  $2(m^n - 1)$ , i.e.,

$$\sum_{j=m^n}^{2m^n-2} \left\{ \begin{array}{l} \sum_{i=j-(m^n-1)}^{i=(1/2)j} f^*(i)f^*(j-i) p(i, j-i) \quad j \text{ even} \\ \sum_{i=j-(m^n-1)}^{(1/2)(j-1)} f^*(i)f^*(j-i) p(i, j-i) \quad j \text{ odd} \end{array} \right\}. \quad (4)$$

If the order of the summations are interchanged, Eq. (4) becomes

$$\begin{aligned} & \sum_{i=1}^{(1/2)m^n} f^*(i) \sum_{j=m^n}^{m^n+i-1} f^*(j-i) p(i, j-i) \\ & + \sum_{i=(1/2)m^n+1}^{m^n-1} f^*(i) \sum_{j=2i}^{m^n+i-1} f^*(j-i) p(i, j-i). \end{aligned} \quad (5)$$

The distribution function  $f^*( )$  on  $i$  can be related to the distribution  $f( )$  on  $n$  by  $f( ) = f^*( ) di/dn$ .<sup>†</sup> The derivative  $di/dn$  may be approximated over the range of the second sum in the first term by  $N_{av}(n+1) - N_{av}(n)$ . If the coalescence probability is also considered to be a constant of the sum, Eq. (5) becomes

$$\begin{aligned} & \left( \sum_{i=1}^{m^n-1} f^*(i)p(i,n)if(n) \right) / (N_{av}(n+1) - N_{av}(n)) \\ & + \sum_{i=m^{n-1}}^{(1/2)m^n} f^*(i) \sum_{j=m^n}^{m^n+i-1} f^*(j-i) p(i, j-i) \\ & + \sum_{i=(1/2)m^n+1}^{m^n-1} f^*(i) \sum_{j=2i}^{m^n+i-1} f^*(j)p(i, j-i). \end{aligned} \quad (6)$$

<sup>†</sup>Cramer, Harald, Mathematical Methods of Statistics, Princeton University Press (1946), p. 292.

The sum over  $i$  is then partitioned into sums over ranges  $s$  with  $p(i,n)$  averaged for each range:

$$\left( \sum_{s=1}^{m-1} P(s,n)f(n) \sum_{i=m^{s-1}}^{m^s-1} if^*(i) \right) / (N_{av}(n+1) - N_{av}(n)) \\ + P(n,n)f^2(n)N_{av}(n)/(N_{av}(n+1) - N_{av}(n)). \quad (7)$$

The substitution in the last term may be considered a definition for  $P(n,n)$ . If Eq. (2) is used in Eq. (7) the result is

$$\frac{\sum_{s=1}^n P(s,n)f(n)N_{av}(s)f(s)}{N_{av}(n+1) - N_{av}(n)}. \quad (8)$$

Expression (8) is the same as that derived by the method using conservation of gas atoms. It is the basis for a computer program<sup>†</sup> that is now being written to calculate bubble-size distribution in mixed-oxide fuels.

(ii) Fuel Swelling Studies (L. C. Michels and G. M. Dragel)

Last Reported: ANL-7595, p. 1 (July 1969).

A technique for the preparation of two-stage replicas has been developed to examine oxide fuels in the electron microscope. This is a modified version of a technique previously used at ANL to examine irradiated carbide fuels.<sup>††</sup>

The initial steps in the preparation of the replicas are carried out remotely in the Metallurgy Division Alpha-Gamma hot cell. Irradiated oxide fuel specimens that have been ground, polished, and etched are used. Plastic replicas of the surface of the specimen are made by placing acetyl cellulose tape, softened with acetone, in contact with the fuel. After hardening, the tape is stripped from the specimen and given an initial cleaning in the hot cell to remove as many adhering bits of fuel as possible. The plastic tape is alternately dipped in an acid solution in methyl alcohol and in a detergent-water solution, both of which are in an ultrasonic cleaner. The plastic replica is then transferred from the hot cell to a fume hood, where additional cleaning steps are carried out until  $\alpha$  and  $\beta$ - $\gamma$  activity is reduced to a minimum.

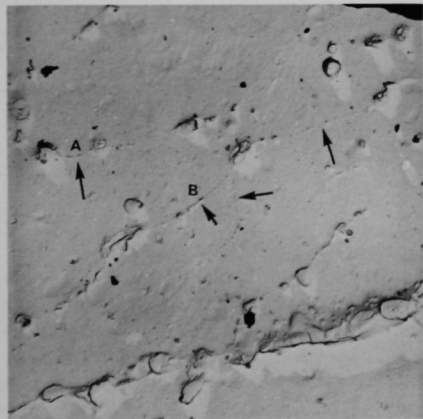
<sup>†</sup>Li, Che-Yu, Pati, S. R., Poeppel, R. B., Scattergood, R. O., and Weeks, R. W., Some Considerations of the Behavior of Fission Gas Bubbles in Mixed-oxide Fuels, to be presented at the Winter ANS Meeting, San Francisco, November/December 1969.

<sup>††</sup>Yoon, Y. K., Watanabe, H., and Kittel, J. H., Plutonium as a Reactor Fuel, IAEA, Vienna, 1967, p. 455.

Following cleaning, the plastic replica is flattened by heating between two glass slides at a temperature not exceeding 70°C. The plastic replica is then placed in a vacuum evaporator and shadowed with Pt-20% Pd at a 30° shadow angle, followed by a vertical deposition of carbon. A layer of melted paraffin is then applied to the shadowed and carbon-coated plastic replica. The purpose of the paraffin coating is to provide support for the fragile platinum-palladium-carbon replica during dissolution of the plastic. The plastic expands during dissolution and without the paraffin support the replica would be destroyed.

Small pieces (approximately 1/16 in. by 1/16 in.) are cut from the paraffin-coated replica and are attached (using acetone), plastic side down, to the 0.125-in.-dia copper grids. Several of the mounted specimens are placed in a wire-mesh basket and introduced into a reflux condenser, where the plastic tape is slowly dissolved in condensing acetone vapor. The paraffin also is dissolved in condensing xylene vapor in the reflux condenser. The platinum-palladium-carbon replica remains on the copper grid. Acetone vapor was used as the final cleaning step in the reflux condenser. The replicas are ready for examination in the electron microscope. The activity at this stage has been reduced to 200-300 dpm  $\alpha$  (fixed) and 0.1-0.3 mR/hr  $\beta$ - $\gamma$  total for three to five specimens.

This technique has been used to prepare replicas of metallographic sections from fuel element SOV-6. The fuel in this element consisted of vibratorily compacted Dynapak particles of (U,Pu)O<sub>2</sub>. The specimen examined was a transverse section taken from the midplane of the fuel column. The burnup achieved was 2.7 at. %, and the fuel surface and centerline operating temperatures were calculated to be 865 and 2565°C, respectively.



X1200

Fig. III.B.9. Replica Electron Micrograph of an Area in the Columnar-to-equiaxed Grain Transition Region of Element SOV-6. The center of the element is to the upper right.

The most important observation was of what appears to be subgrain boundaries in the equiaxed grains and in the transition region between the equiaxed and columnar grains. These subgrain boundaries are shown in Fig. III.B.9, and, in the lower portion of the figure, a grain boundary is evident, along which large gas bubbles have collected. Many small bubbles and some larger gas bubbles and inclusions lie along the subgrain boundaries indicating that they are efficient trapping sites for fission gases. Some of these boundaries are bowed (see Fig. III.B.9, A and B), suggesting

either that the boundaries are migrating or that the associated large bubbles or inclusions are moving and dragging the boundary. It is difficult to establish which movement is occurring because the temperature gradient in the fuel is perpendicular to either migration. If the subgrain boundaries are migrating, this could be a mechanism for sweeping fission gas bubbles to grain boundaries. In either event, the trapping of gas bubbles on the subgrain boundaries would have to be considered in calculating release rates of fission gases.

(iii) Fuel-element Performance (L. A. Neimark, F. L. Brown, W. F. Murphy, and H. V. Rhude)

(a) Examination of Group O-2 Fuel Elements

Last Reported: ANL-7632, pp. 109-110 (Oct 1969).

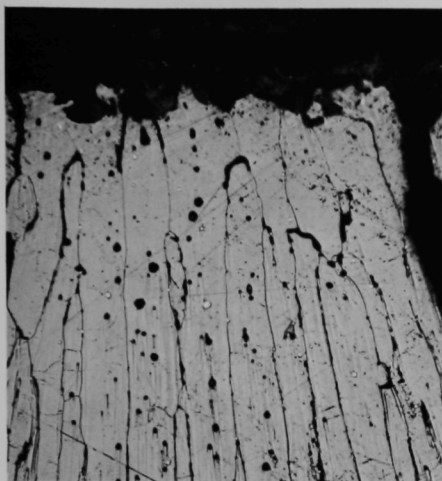
Analysis of the fission gas recovered from the plenum of SOV-1 showed that the mixed-oxide fuel in this element (irradiated in EBR-II) had released 57% of the fission gas generated, based on an estimated maximum burnup of 5.0 at. %. This gas release was comparable to the release from the same fuel material irradiated in a companion element to 3.6 at. % burnup at 6% higher initial operating power. Table III.B.1 summarizes the design parameters, operating conditions, and the results of dimensional inspections and fission-gas release measurements for the three stainless steel-clad elements in Group O-2.

TABLE III.B.1. Summary of Group O-2 Type 304 Stainless Steel-clad Fuel Elements

Element	Burnup (at. %)	Max Heat Generation (kW/ft)	Fuel Smear Density (%)	Max Diameter Increase (%)	Length Increase (%)	Volume Increase (%)	Gas Release (%)
SOV-1	5.0	20.1, 19.5 <sup>a</sup>	80	0.61	0.16	0.82	57
SOV-3	3.7	21.4	83	0.40	0.08	0.67	-
SOV-7	3.6	21.3	85	0.40	0.09	0.62	61

<sup>a</sup>Second burnup increment of 1.4 at. %.

Metallographic examination of SOV-1 continued with the etched sections. The etchant was 8 parts 30% H<sub>2</sub>O<sub>2</sub> and 2 parts concentrated H<sub>2</sub>SO<sub>4</sub>. Etching was by immersion at room temperature. Evident in the etched microstructure of the columnar grain region were what appeared to be bubble trails indicating movement of spherical bubbles to the central void (see Fig. III.B.10). These bubble trails were observed at all elevations in the fuel column. Etching first revealed trails near the outer boundary of the columnar grain region; additional etching was required to develop the trails in the microstructure closer to the center of the fuel. Adjacent to the central void the trails appeared short and fainter, even though etching was prolonged for several hours.



FP-11652       $A_2O_2 + H_2SO_4$  etch      150X

Fig. III.B.10. Bubble Trails in Columnar Grain Adjacent to the Central Void (top) near the Top End of SOV-1

Evidence of fuel-cladding interactions was found along the length of the element but mainly in the upper half. This attack is believed to be by iodine, with the resultant removal of grain-boundary material as iodides. The calculated cladding-interface temperature at which this attack became apparent was  $550^{\circ}C$ . The maximum depth of attack found by optical metallography was 8.8 mils, halfway between the midlength and the top of the fuel column, where the calculated temperature was  $590^{\circ}C$ , the maximum cladding temperature obtained in the element.

Grain-boundary carbide precipitation, previously observed in the stainless steel cladding of Group O-2 elements after 3.6 at. % burnup, was again found in SOV-1 after 5.0 at. %, but in no more

marked degree. Cladding-hardness increases were the same as previously observed after 3.6 at. % burnup--from 25 to 56% higher than the preirradiation value of 174 DPH--with the largest increase occurring in the cooler operating region near the bottom of the element.

#### (b) Preparation of Group O-3 Fuel Elements

Last Reported: ANL-7632, p. 110 (Oct 1969).

Eighteen encapsulated mixed-oxide fuel elements of Group O-3 have passed all inspections called for in the quality assurance plan and were accepted for irradiation by the experimenter. The capsules have been shipped to Idaho for loading into EBR-II Subassembly XO72, which is scheduled for irradiation beginning with Run 39. A summary of the design variables in the 18 Group O-3 fuel elements is given in Table III.B.2.

A nineteenth capsule, to complete the complement of the 19-capsule Mark-A subassembly, is in preparation. This capsule will contain a specimen of Type 316 stainless steel tubing from the same batch as that of the cladding on four of the fueled Group O-3 elements. This tubing will provide control specimens for postirradiation mechanical property tests on the element cladding to assess the effects of fuel-cladding chemical interactions.

TABLE III.B.2. Summary of the As-loaded Group O-3 Fuel Elements

Capsule Identification	Fuel Type	Stainless Steel Cladding	Cladding Dimensions OD/ID (in.)	Fuel Length (in.)	Pellet Diameter (in.)	Average Smear Density (% T.D.) <sup>b</sup>	Max Smear Density (% T.D.) <sup>b</sup>
ASOPC-1	Pellet <sup>a</sup>	Type 304	0.290/0.260	12.16	0.256	79.8	80.2
ASOPC-2	Pellet	Type 304	0.290/0.260	12.19	0.256	79.6	80.4
ASOPC-3	Pellet	Type 304	0.290/0.260	12.16	0.256	82.5	83.9
ASOPC-4	Pellet	Type 304	0.290/0.260	12.16	0.256	82.4	83.6
ASOPC-5	Pellet	Type 304	0.290/0.260	12.08	0.246	76.8	77.4
ASOPC-6	Pellet	Type 304	0.290/0.260	12.01	0.246	76.8	77.4
ASOPC-7	Pellet	Type 316	0.290/0.260	11.93	0.257	83.0	85.0
ASOPC-8	Pellet	Type 316	0.290/0.260	11.97	0.257	82.9	85.3
ASOPC-9	Pellet	Type 318	0.290/0.260	12.19	0.256	82.4	83.6
ASOPC-10	Pellet	Type 318	0.290/0.260	11.94	0.257	82.4	84.9
ASOV-14	Dynapak <sup>c</sup>	Type 304	0.290/0.250	12.00	-	79.7	-
ASOV-15	Dynapak	Type 304	0.290/0.250	12.00	-	79.5	-
ASOV-16	Dynapak	Type 304	0.290/0.250	12.00	-	80.2	-
ASOVG-17	Sol-gel <sup>d</sup>	Type 304	0.290/0.260	12.00	-	79.7	-
ASOVG-18	Sol-gel	Type 304	0.289/0.260	12.00	-	79.5	-
ASOVG-19	Sol-gel	Type 316	0.289/0.260	12.00	-	79.3	-
ASOVG-20	Sol-gel	Type 316	0.290/0.260	12.00	-	79.4	-
ASOVG-21	Sol-gel	Type 318	0.290/0.260	12.00	-	80.1	-

<sup>a</sup>Solid solution pellets of (U<sub>0.8</sub>Pu<sub>0.2</sub>)O<sub>2</sub>.<sup>b</sup>Theoretical density, 11.07 g/cm<sup>3</sup>.<sup>c</sup>Sol-gel microspheres, vibratorily compacted (U<sub>0.8</sub>Pu<sub>0.2</sub>)O<sub>2</sub>.<sup>d</sup>Dynapak powder, vibratorily compacted (U<sub>0.8</sub>Pu<sub>0.2</sub>)O<sub>2</sub>.

### (c) Out-of-reactor Simulation Experiments

Not previously reported.

The mechanical interaction between fuel and cladding in the form of homogeneous and nonhomogeneous stresses is believed to be one of the major causes of fuel-element failure. Out-of-reactor experiments to study specific aspects of fuel-element behavior are being undertaken to understand these mechanical interactions better, and to aid in developing analytical models of fuel-cladding mechanical interactions that can be used in computer codes to predict fuel-element lifetime. Phenomena to be investigated are cladding ridging, axial and radial ratcheting on thermal cycling, local interactions between cracked fuel and cladding, and dry-slumping of the fuel.

A mockup of a high-temperature furnace that incorporates a tungsten heating element for internal, axial heating of a fuel column has been built and tested. Data from these tests are being used to finalize the design of a furnace suitable for these experiments. Procurement of annular fuel pellets and cladding for the initial experiments has been initiated.



## 2. Techniques of Fabrication and Testing--Research and Development

### a. Nondestructive Testing Research and Development (H. Berger)

#### (i) Laser Studies and Holography (N. Fernelius)

Last Reported: ANL-7618, pp. 97-99 (Sept 1969).

Some investigations were made to alleviate the problem of repositioning a developed hologram for real-time interferometric studies. Several samples of photochromic glass were obtained from the Corning Glass research laboratory. This glass darkens when exposed to ultraviolet light and bleaches when exposed to red light. Since it is immaterial whether a hologram is taken with positive or negative film, we hoped to bleach out a hologram on a properly darkened glass plate. If this had been feasible, a reference hologram for real-time interferometric studies that could have been developed in situ would have resulted and both repositioning and emulsion shrinkage problems would have been avoided.

Several crucial difficulties were encountered: (1) the glass sample could not be darkened appreciably with existing sources of ultraviolet light, (2) the darkening of photochromic glass fades even when kept in the dark, and (3) the red-light intensities necessary for bleaching were somewhat greater than expected.

Some samples of gamma-irradiated glass ( $>10^6$  rad) were obtained that were light brown in color. No darker colored centers were perceived when irradiated with our ultraviolet source. Some samples of cobalt glass that had been irradiated with doses  $>10^5$  to  $10^6$  rad were tested. We were unable to bleach out the dark purple color even though the glass was illuminated by a 20-mW undispersed He-Ne laser beam for several days.

#### (ii) Development of High-temperature Piezoelectric Transducers (R. H. Selner)

Last Reported: ANL-7595, p. 102 (July 1969).

A circumferential butt weld in the Core Components Test Loop (CCTL) was inspected\* with a conventional ultrasonic shear-wave technique. The cold-weld inspection was conducted at room temperature to determine if any discontinuities existed in this highly stressed weld. Two discontinuities with reflection amplitudes about 30 and 75% of that obtained from the standard reflector (2.38-mm diameter by 38.1-mm long) were detected. Continuous or periodic monitoring of the largest discontinuity

---

\*In accordance with ASME Boiler and Pressure Vessel Code, Section III, Nuclear Vessels, Appendix IX, 201-230 (1968).



with the test loop in operation is planned provided an ultrasonic transducer, which can operate up to 600°C, can be designed and manufactured.

The shear-wave transducer used in the cold-weld inspection generated a 70° shear wave into the loop wall (Type 304 stainless steel) by mode converting a longitudinal wave from a plastic wedge (generally Lucite). A similar scheme can be utilized in a high-temperature transducer by replacing the Lucite wedge with one of fused silica. Because the longitudinal velocity is much higher in fused silica than Lucite, a suitable shear-wave angle (45° or higher) cannot be produced in stainless steel with a fused silica wedge angle approaching 90°. However, a fused silica wedge with an angle of 58° and with a shear-wave transducer will generate a 45° shear wave in stainless steel. A high-temperature transducer incorporating these features is being constructed.

A high-temperature vacuum furnace facility (maximum operating temperature of 2400°C) is being assembled. When complete, this facility will increase our production capabilities of brazed acoustic sensors.

Alternative techniques of attaching lithium niobate and other piezoelectric crystals to metals and other high-temperature materials are being investigated. A zirconia-base cement that has a maximum operating temperature of about 2200°C has been ordered and received. Experiments to determine the capabilities of this cement will be conducted.

### 3. Engineering Properties of Reactor Materials--Research and Development

#### a. High Temperature Mechanical Properties of Ceramic Fuels

##### (i) Plastic Yielding and Fracture of Fuel Oxides (B. J. Wrona and J. T. A. Roberts)

Not previously reported.

An Instron Universal testing machine and high-temperature furnace, which were enclosed in an inert-atmosphere dry box, will be used to study the out-of-pile, short-term, high-temperature mechanical properties of  $\text{UO}_2$ - $\text{PuO}_2$  compounds in four-point bending. The aim of this program is to investigate the influence of  $\text{PuO}_2$  on the mechanical properties of  $\text{UO}_2$  as a function of density, grain size, and stoichiometry. Initially, the composition will be  $\text{UO}_2$ -20 wt %  $\text{PuO}_2$ , which is the proposed starting fuel for the LMFBR series. The mechanical-properties data are necessary input for the fuel-lifetime prediction codes. At the same time, it is hoped to elucidate flow and fracture mechanisms.

Test specimens were fabricated as follows. An intimate mixture of  $\text{UO}_2$ -20 wt %  $\text{PuO}_2$  was achieved by ball milling with 0.5 wt % carbowax 4000 in ethyl alcohol for 3 hr. After drying, the powder was pressed into slugs at a pressure of 6000 psi, then the slugs were pulverized and pressed into bars at a pressure of 12,000 psi. The bars were sintered at a temperature of 1575°C in a flowing He-6%  $\text{H}_2$  atmosphere for 4 hr. Typical dimensions of the sintered bars were 1.77 by 0.21 by 0.23 cm. The sintered bars were nearly fully reacted, with an oxygen-to-metal ratio of 1.977, and were 90% of theoretical density. The grain size has not been determined because a suitable etchant has not been found. However, the grain size is probably small.

Typical load-deflection curves for specimens deformed at a strain rate of 0.097/hr are reproduced in Fig. III.B.11. At 1000°C, completely brittle behavior was observed. The two specimens tested so far failed at stresses of 941 and 1083  $\text{kg}/\text{cm}^2$ , and possessed Young's moduli of 780,000  $\text{kg}/\text{cm}^2$  ( $11.1 \times 10^6$  psi) and 800,250  $\text{kg}/\text{cm}^2$  ( $11.4 \times 10^6$  psi), respectively. Plastic deformation was observed at 1400°C, and the elastic region was almost negligible; however, the specimens did fail after relatively small deflections. At 1500 and 1600°C the specimens tested were completely plastic, and no elastic region was detected. The material work hardened up to the maximum deflection measured, without failure.

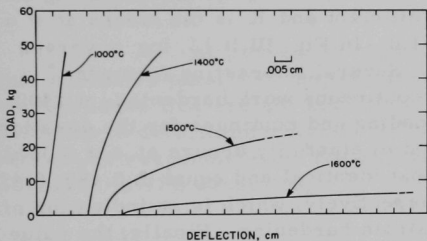


Fig. III.B.11. Load-deflection Curves at Four Temperatures

To analyze the load-deflection curves, the Nadai\* procedure for the analysis of a plastically bent beam was employed. The maximum stress parallel to the outer tension and compression surfaces of the bend specimen is

$$\sigma = \frac{2a}{bh^2} \left( W + \frac{\delta}{2} \frac{\partial W}{\partial \delta} \right), \quad (1)$$

where  $a$  is the distance between the inner and outer loading contacts,  $b$  is the specimen width,  $h$  is the thickness,  $W$  is the transverse load applied to the specimen, and  $\delta$  is the total transverse deflection (elastic plus plastic) of the specimen between the inner contacts. In the absence of plasticity, Eq. (1) reduces to the conventional formula for the rupture modulus:

$$\sigma_F = M_R = 3Wa/bh^2 \quad (2)$$

for an elastically bent beam.

\*Nadai, A., Theory of the Flow and Fracture of Solids, McGraw-Hill Book Co., Inc., New York (1950), p. 353.

All the data obtained so far are summarized in Fig. III.B.12 in the form of plots of maximum stress and plastic strain versus temperature.

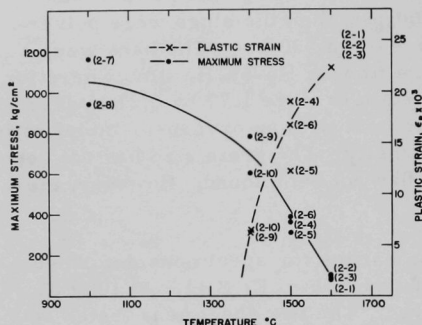


Fig. III.B.12. Maximum Stress and Plastic Strain vs Temperature for All Specimens Tested

The brittle-ductile transition lies somewhere in the 1000-1400°C temperature range. This compares favorably with the 1250°C transition temperature reported for a higher density (97%)  $\text{UO}_2$  material.\*

A material deforming plastically in the strain-hardening region generally obeys the stress-strain relationship

$$\sigma = K\epsilon^n, \quad (3)$$

where  $n$  is the strain-hardening coefficient and  $K$  is the stress at  $\epsilon = 1.0$ . In Fig. III.B.13,  $\log \sigma$  versus

$\log \epsilon$  is plotted at three temperatures. Several interesting features emerge. First, the linear plots imply continuous work hardening; at 1500 and 1600°C this starts at the onset of loading and continues for the duration of the test, but at 1400°C a small amount of elasticity occurs at  $\epsilon \leq 0.00025$ . Second, the slopes of the plots are almost identical and equal to 0.489, 0.434, and 0.455 at 1400, 1500, and 1600°C, respectively, which is an indication of approximately the same coefficient of strain hardening. Finally, the value of  $K$  increases exponentially with decreasing temperature (see Fig. III.B.14).

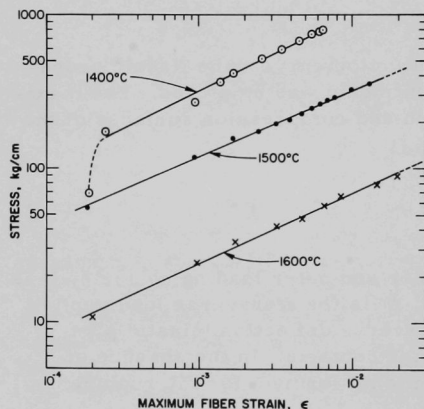


Fig. III.B.13. Plot of  $\log \sigma$  vs  $\log \epsilon$  at Three Temperatures

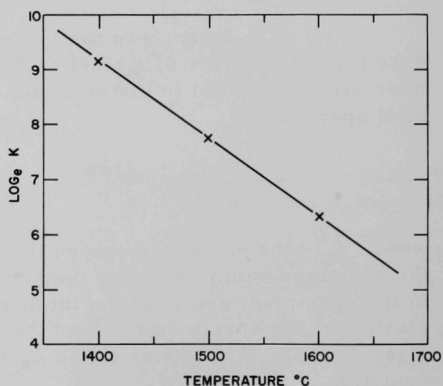


Fig. III.B.14. Plot of  $\log_e K$  vs Temperature

\*Beals, R. J., and Canon, R. F., ANL Report at 28th Meeting of High Temperature Fuels Committee, May 13-15, 1969.

Tentatively, these results permit writing an equation of deformation that excludes an elastic contribution for the temperature range 1400-1600°C. Thus,

$$\sigma = K\epsilon^{0.459 \pm 0.022},$$

where

$$K = e^{(28.83 - 0.014T)}.$$

Therefore,

$$\sigma = e^{(28.83 - 0.014T)} \epsilon^{0.459 \pm 0.022},$$

or

$$\sigma = 3.3 \times 10^{12} e^{-0.014T} \epsilon^{0.459 \pm 0.022}.$$

At present, no firm conclusion can be drawn to explain this extensive plasticity, nor the mechanism involved. Deformation data on 90% dense  $\text{UO}_2$  are not available, but are being collected. This data will help to determine whether the additional porosity or the introduction of  $\text{PuO}_2$  is responsible for the change in deformation behavior that is observed in 97% dense  $\text{UO}_2$ .

## C. Engineering Development--Research and Development

### 1. Instrumentation and Control

#### a. Boiling Detector (T. T. Anderson)

Last Reported: ANL-7632, pp. 113-114 (Oct 1969).

##### (i) Acoustic Method

##### (a) Boiling-sodium Spectra in Simulated Reactor Geometries (T. T. Anderson)

When sodium boiling is initiated in an LMFBF channel, increased resistance to flow caused by the sodium vapor would change the hydraulic characteristics of the boiling channel relative to adjacent channels. A calculational procedure\* has been developed to relate time-dependent pressure drops to mass flowrate in terms of a "hydraulic impedance." Tests on a single-channel natural- or forced-convection boiling loop show the method to apply for (1) single-phase forced-convection flow, (2) two-phase forced-convection flow, and (3) two-phase hydrodynamically unstable natural-convection flow. Conceptually, the method can be used to determine the interrelationship between sodium vapor and the perturbed flow in a fuel subassembly.

##### (b) Irradiation and Resistance Tests of Piezoelectric and Insulator Materials (T. T. Anderson and S. L. Halverson)

A third irradiation has been performed with 1-2-MeV electrons on high-phase-match Y-cut lithium niobate clamped in an electromechanical transducer assembly (test rig H-2). The two previous tests had focused on detecting acoustic signals in the presence of the ionizing radiation; this test was concerned with measuring basic crystal properties in the presence of the radiation. For this purpose, transducer impedance was measured at the resonance frequencies of the crystal. A change in resonance properties could then be interpreted as a radiation-induced effect in the crystal under irradiation. Charge and voltage output from the crystal were measured for mechanical excitation provided by an ultrasonic transducer (0-1 MHz, 0-5 MHz frequency scans).

These data were obtained on X-Y recorders for conditions before, during, and after irradiation. Conversion of the large quantity of data to electromechanical characteristics was made difficult by the

---

\*Anderson, T. T., Hydraulic Impedance: A Tool for Predicting Boiling Loop Stability, (to be presented at the ANS Winter Meeting, San Francisco, Nov. 30-Dec. 4, 1969).

transmission-line characteristics of a 50-ft coaxial cable between the crystal and the impedance-measuring system. Because this same problem would apply to measuring in-reactor characteristics of piezoelectric devices, a computer program has been written to convert the raw impedance data directly into transducer efficiency, quality factor  $Q$ , sensitivity, and the electromechanical-transducer phasor. Data processing has just begun, but several qualitative statements can be made.

Direct examination of the on-line X-Y plots of impedance showed that, during irradiation, resonance peaks decreased and the first resonance region contained a larger number of small-amplitude resonances. Electrical resistivity of the assembly decreased by factors of  $10^2$  to  $10^4$ . After the irradiations, there was a short-term partial recovery of resonance characteristics (within 5 min), followed by a more extensive recovery (hours to days).

When electrons partially penetrated the crystal, damage appeared to be more severe than during complete penetration. Tests are in progress to determine whether this effect at the lower energies could be attributed to asymmetrical straining of the crystal.

Another electron-irradiation test of lithium niobate is planned to compare the short-term after-irradiation effects for different crystal orientations and compositions. From optical and electrical measurements of the crystals, we hope to estimate how electrons trapped in the crystal would affect transducer performance in a reactor environment.

(c) Development of High-temperature Detector  
(A. P. Gavin)

Acoustic vibration response has been measured for test rigs that had a nickel or stainless steel rod to transmit vibrations between a mechanical shaker on one end and a lithium niobate transducer assembly on the other. Performance of the transducer assembly has been improved by sandwiching the crystal between the stainless steel transmission rod and a stainless steel terminating rod to form a "Hopkinson-bar transducer."\* Fortuitously for high-temperature applications, stainless steel provides an excellent acoustic impedance match to lithium niobate, allowing optimum transmission of acoustic energy.

Tests are being prepared to measure the high-temperature performance of the transducer assembly in the lightweight furnace described in ANL-7632.

---

\*Thompson, R. A., Quartz Crystal Pressure Bar Transducer with a Two Microsecond Response, SCL-DR-66-110, Sandia Corp. (March 1967).

## 2. Heat Transfer and Fluid Flow (M. Petrick)

### a. LMFBR Burnout Limitations (R. J. Schiltz and R. Rohde)

Last Reported: ANL-7632, pp. 114-116 (Oct 1969).

(i) Preparation of Apparatus. The main piping system assembly is ~25% complete.

The six 1.5-in. valves for the loop have been received from the shop after extensive rework, repair, and final inspection involving dye-penetrant checks and radiography. Two of these valves have been welded into part of the piping system. Fabrication of the oil-cooling system for the electromagnetic helical induction pump is ~25% complete.

The design of the transition section for the heat exchanger to the air-duct system has been completed. The air-cooled heat exchanger has been instrumented with thermocouples and fitted with electric heaters. The unit is being prepared so that the vibration characteristics can be observed when the unit is subjected to the maximum air-blower output.

System piping changes have necessitated a final thermal-expansion analysis and hanger-load analysis. A contract for this work has been initiated.

The extension of the loop superstructure has been completed and a portion of the equipment for the tests has been mounted on this extension.

### b. Heat Transfer in Liquid-Metal Heat Exchangers

#### (i) Boundary-value Problems in Forced-convection Heat Transfer (R. P. Stein)

Not previously reported.

This new research activity has as its main objective the unification, generalization, and extension of previous investigations of heat transfer in liquid-metal-cooled reactor channels and heat exchangers.

An analytical study considered the general case of a single-pass shell-and-tube heat exchanger with fully developed laminar flow through the tube side and a turbulently flowing nonmetallic fluid through the shell side. The shell-side heat-transfer coefficient was taken as constant, an assumption considered to be a good approximation for the turbulent flow of nonmetallic fluids in un baffled, or closely spaced baffled, heat exchangers. Heat-transfer coefficients were not used for the tube side. Instead, the



two-dimensional convection equation (based on the usual assumptions of temperature-independent properties, negligible axial conduction, etc.) served as the basis of the study.

An interesting result of the study (similar to previous results) is that the customary heat-exchanger design formulas can be made to apply by use of the actual fully developed overall heat-transfer coefficient and an effective additional heat-exchanger length. The overall heat-transfer coefficient depends, of course, on the tube-side heat-transfer coefficient which, as noted in previous studies, depends on the operating conditions of the exchanger in a complex manner. The effective additional heat-exchanger length accounts for the high rates of heat transfer in the thermal-entrance region of the exchanger and also depends on the operating conditions of the exchanger.

The operating conditions of the exchanger can be characterized by two dimensionless quantities,  $K_T$  and  $H$ , and by whether the flow is countercurrent or cocurrent. The quantity  $K_T$ , a relative total thermal resistance of the heat-exchanger wall and shell-side convection, is defined by

$$K_T = \frac{b'k}{ak_w} + \frac{k}{h(a+b)},$$

where  $k$  is thermal conductivity of tube-side fluid,  $k_w$  is thermal conductivity of wall,  $h$  is heat-transfer coefficient for shell side,  $a$  is inside radius of tube,  $b$  is wall thickness, and  $b' = a \ln [1 + (b/a)] \approx b$  for  $b/a \ll 1$ . The quantity  $H$  is the ratio of heat capacity to flowrate, defined by  $H = C_2 W_2 / C_1 W_1$ , where  $C_i$  is the specific heat of fluid  $i$ ,  $W_i$  is mass rate of flow of fluid  $i$ ;  $i = 1$  identifies the tube-side fluid and  $i = 2$  refers to the shell-side fluid.

The fully developed overall heat-transfer coefficient is conveniently expressed as an overall Nusselt number  $Nu_1^0 = 2aU_1/k$ , where  $U_1$  is the fully developed overall heat-transfer coefficient referred to the tube side. For sufficiently large values of  $K_T$  (say  $K_T > 10$ ),  $Nu_1^0 \sim 2/K_T$ , indicating that heat-transfer rates are controlled by the shell-side and wall thermal resistance so that tube-side coefficients need not be known accurately.

A dimensionless heat-exchanger length is defined by  $Z = (4/Pe_1)(L/D)$ , where  $Pe_1$  is the tube-side Peclet number,  $L$  is the heat-exchanger length, and  $D$  is the tube inside diameter. With the effective additional heat-exchanger length denoted by  $\Delta L$ ,  $\Delta Z$  represents its dimensionless counterpart when  $L$  is replaced by  $\Delta L$  in the above definition of  $Z$ . For sufficiently large values of  $Z$ , both  $\Delta Z$  and the tube-side Nusselt number become independent of  $Z$ , and the heat transfer is considered "fully developed."

Table III.C.1 shows representative values of the various dimensionless quantities as a function of the heat-exchanger operating conditions. Included in the table is the dimensionless length  $Z^*$  required for "fully developed" heat-transfer conditions, and the heat-exchanger effectiveness  $\epsilon^*$  corresponding to  $Z^*$ . Thus, the customary heat-exchanger design formulas can be used with  $U_1$  determined from  $Nu_1^0$  and with  $L$  replaced by  $L + \Delta L$ , as determined from  $\Delta Z$ , provided  $Z > Z^*$  or  $\epsilon > \epsilon^*$ . Also included in the table are values of the fully developed tube-side Nusselt number  $Nu_1$ . Recall that for fully developed laminar flow in a tube,  $Nu_1 = 3.66$  corresponds to the boundary condition of uniform wall temperature;  $Nu_1 = 4.36$  corresponds to the boundary condition of uniform wall flux.

TABLE III.C.1. Various Heat-exchanger Quantities  
as a Function of Operating Conditions

$K_T$	$H$	$Nu_1^0$	$Nu_1$	$\Delta Z$	$Z^*$	$\epsilon^*$
<u>Cocurrent Flow</u>						
0.1	0.1	1.02	1.07	0.167	0.080	0.938
	1	2.76	3.21	0.059	0.120	0.630
	10	3.13	3.71	0.046	0.113	0.421
1	0.1	0.91	1.67	0.091	0.235	0.962
	1	1.32	3.87	0.018	0.170	0.390
	10	1.34	4.10	0.015	0.156	0.223
<u>Countercurrent Flow</u>						
0.1	0.1	6.07	8.71	0.004	0.016	0.693
	1	3.58	4.37	0.032	0.098	0.317
	10	3.21	3.82	0.043	0.111	0.383
1	0.1	1.503	6.05	0.004	0.068	0.645
	1	1.371	4.37	0.013	0.141	0.173
	10	1.350	4.15	0.014	0.153	0.200

### 3. Engineering Mechanics (G. S. Rosenberg)

#### a. Structural Dynamics--Structure-Fluid Dynamics (M. W. Wambsganss, Jr.)

##### (i) Mathematical Modeling of Parallel-flow-induced Vibration (S. S. Chen)

Last Reported: ANL-7618, pp. 108-109 (Sept 1969).

An analytical solution has been obtained for the displacement statistics of a simply supported rod in parallel flow. The motion is

described by Paidoussis' equation<sup>†</sup> and the system is postulated to be excited by pressure fluctuations in the turbulent boundary layer.

The mathematical model for the turbulent-boundary-layer pressure is based on that of Bakewell.<sup>††</sup> The power spectral densities of turbulent wall pressure obtained by Bakewell and others<sup>‡</sup> are shown in Fig. III.C.1, where  $V$  is flow velocity,  $\rho$  is fluid density,  $\omega$  is circular frequency, and  $\delta^*$  is displacement thickness. Numerical calculations were performed using the dashed curve of Fig. III.C.1, which correlates the data of Bakewell and Clinch<sup>‡</sup> quite well. Using Bakewell's data for the space-time correlation function and following a random-vibration approach, the power spectral density of the rod displacement,  $y(x, t)$ , can be written as

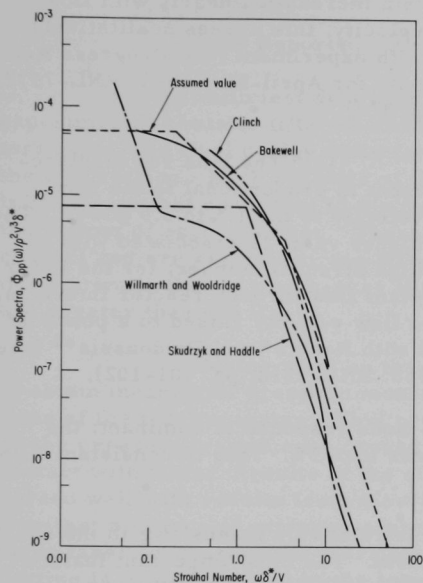


Fig. III.C.1. Nondimensional Spectral Densities of Turbulent-boundary-layer Pressure

where  $D_e$  is the effective rod diameter,<sup>‡‡</sup>  $\phi_n(x)$  is the orthonormal mode,  $H_n(\omega)$  is the transfer function, and  $J_n^2(\omega)$  is the joint acceptance. The curves of the joint acceptance for the first five modes are shown in Fig. III.C.2, where  $\gamma$  is a dimensionless frequency. The physical significance of the joint acceptance is that it represents the "effectiveness" of the pressure in exciting a mode of the rod. It will take on a relatively large value when the pressure correlation has a significant contribution at the predominant wavelength of the mode concerned.

<sup>†</sup>Paidoussis, M. P., Dynamics of Flexible Slender Cylinder in Axial Flow, Part I, Theory, J. Fluid Mech. **26**, 717-736 (1966).

<sup>††</sup>Bakewell, H. P., Jr., Turbulent Wall-Pressure Fluctuations on a Body of Revolution, J. Acoust. Soc. Am. **43**, 1358-1363 (1968).

<sup>‡</sup>Clinch, J. M., Measurements of the Wall Pressure Field at the Surface of a Smooth-Walled Pipe Containing Turbulent Water Flow, J. Sound Vib. **9**, 398-419 (1969); Willmarth, W. W., and Wooldridge, C. Z., Measurements of the Fluctuating Pressure at the Wall beneath a Thick Turbulent Boundary Layer, J. Fluid Mech. **14**, 187-210 (1962); Skudrzyk, E. J., and Haddle, G. P., Noise Production in a Turbulent Boundary Layer by Smooth and Rough Surfaces, J. Acoust. Soc. Am. **32**, 19-34 (1960).

<sup>‡‡</sup>Reavis, J. R., WVI-Westinghouse Vibration Correlation for Maximum Fuel Element Displacement in Parallel Turbulent Flow, Trans. Am. Nucl. Soc. **10**, 1, 369-370 (June 1967).

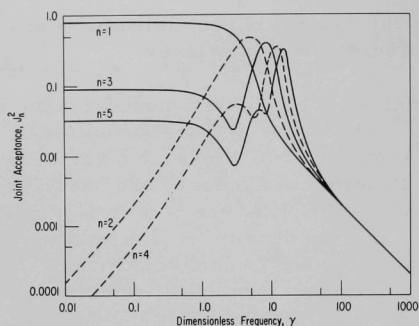


Fig. III.C.2. Joint Acceptance as a Function of Dimensionless Frequency

Four general conclusions are drawn from the mathematical model and numerical solutions:

(1) The damping of the system increases linearly with flow velocity; this agrees qualitatively with experiment (see Progress Report for April-May 1969, ANL-7577, p. 166).

(2) The rms rod displacement is proportional to the flow velocity to the 1.5 to 3.0 power. The higher value is associated with a high Strouhal number; for the lower

Strouhal numbers, characteristic of coolant flow through reactor internals, rms displacement is proportional to the flow velocity raised to a power of 1.5 to 2.0. This result is in agreement with Reavis\* and Paidoussis\*\* (see also Progress Report for November 1968, ANL-7518, pp. 101-102).

(3) The first bending-mode response is dominant; the contributions from higher modes are less than 5%. This is consistent with experimental observations.\*\*†

(4) The rod response is relatively insensitive to the detailed characteristics of the pressure field. The most important feature of the pressure field required in the mathematical model is the power spectrum of the wall pressure at lower values of Strouhal number. Dependable data are not available in this range. Clinch reported the existence of "extraneous noise" at lower Strouhal numbers. Willmarth and Wooldridge found that the power spectrum of the pressure fluctuations contained a large energy density at low frequencies. Figure III.C.1 shows that at lower Strouhal numbers the data obtained by different experimenters have differences of an order of magnitude. It is precisely the lower range of Strouhal number that is important in reactor applications. This emphasizes the need for making wall-pressure measurements on the surface of the rod in the lower range of Strouhal numbers.

This mathematical model is successful in predicting the essential features and basic trends of parallel-flow-induced vibration. However, further experimental data for the vibration of a cylindrical rod in axial flow are needed in order to quantitatively predict rms-displacement response and thus to evaluate the mathematical model; in particular, the

\*Reavis, J. R., *Ibid*, see previous page.

\*\*Paidoussis, M. P., *An Experimental Study of Vibration of Flexible Cylinders Induced by Nominally Axial Flow*, Nucl. Sci. and Eng. **35**, 127-138 (1969).

†Wambgsans, M. W., Jr., and Boers, B. L., *Parallel-flow-induced Vibration of a Cylindrical Rod*, Mechanical Engineering Abstract **91**, 4, 64 (April 1969).

power spectral density of wall pressure at lower Strouhal numbers is needed. The experimental effort to obtain this information is continuing.

(ii) Preparation of Two Structural Dynamics Test Loops  
(P. L. Zaleski)

Last Reported: ANL-7632, p. 122 (Oct 1969).

Sufficient data have been accumulated from tests with an experimental acoustic filter to initiate construction of a filter for the small test loop. The final design calls for filters upstream and downstream of the test section. Each consists of three chambers (representing semi-infinite cavities) connected to the flow channel by a short pipe located near the bottom of each chamber. These cavities are mounted axially along the channel and are essentially air-filled during operation. The response of the system is that of a high-pass filter; the calculated cutoff frequencies are greater than 400 Hz.

During tests on the acoustic-filter systems, it was difficult to obtain meaningful pressure measurements because of structural vibrations of the test apparatus. This prompted a study of acceleration effects on the pressure transducers caused by the inertial loading of the fluid in contact with them. Results of the simplified analysis that was performed agreed well with results from a series of tests performed on a shaker table. Now that a source of extraneous pressure has been identified, steps are being taken to improve the vibration isolation of the test section; the test section is being installed in the loop for the purpose of measuring induced acceleration levels.

D. Chemistry and Chemical Separations

1. Fuel Cycle Technology--Research and Development

a. Molten Metal Decladding (R. D. Pierce)

(i) Behavior of Volatile Fission Products

Last Reported: ANL-7632, pp. 122-124 (Oct 1969).

(a) Laboratory Process Development. A large portion of the fission-product iodine is expected to be present as elemental iodine in the annular and plenum regions of irradiated reactor fuel. In the present concept of decladding by use of a liquid metal this iodine will be liberated when the cladding (stainless steel or Zircaloy) is dissolved in liquid zinc at 800°C. The distribution of iodine between the zinc, a cover salt, and the gas phases is being investigated. Apparatus fabricated for measuring the degree of reaction of iodine with zinc and the cover salt consists of a reaction

vessel, a reflux condenser, and a gas analyzer in a train. The operating procedure for the first scouting experiments, which are now under way, is as follows: a steel capsule containing a known amount of iodine is dropped into a pool of zinc at 800°C, releasing the iodine to bubble through the zinc and a LiF-NaF cover salt into a stream of argon that passes through the equipment train. The quantity of unreacted iodine is measured with the gas analyzer downstream from the zinc melt.

## 2. General Chemistry and Chemical Engineering--Research and Development

### a. Thermophysical Properties

- (i) Oxygen Gradients, Total Vapor Pressures, and Oxygen Potentials in Reactor Fuels (P. E. Blackburn and A. J. Becker)

Last Reported: ANL-7606, p. 117 (Aug 1969).

The transpiration apparatus that will be used to measure oxygen potentials and total pressures over U-Pu-O has been successfully tested. The volume of the apparatus was calculated to be 29.3 liters. The calibration of the on-line oxygen meter, by successive dilutions of air with argon, indicated that it functioned correctly down to 100 ppm O<sub>2</sub> (the lowest oxygen pressure tested).

Oxygen pressures measured over U<sub>3</sub>O<sub>8</sub>-U<sub>4</sub>O<sub>9</sub> at 1725 and 1775°K were  $5.0 \times 10^{-2}$  and  $9.2 \times 10^{-2}$  atm, respectively. The length of time expended in each experiment was too short to obtain accurately condensable species pressures from the weight data displayed by the balance incorporated into the apparatus. However, a comparison between the sample weights before and after equilibrium indicated pressures of uranium-bearing species were very much less than that of oxygen.

Oxygen pressures over U<sub>3</sub>O<sub>8</sub>-U<sub>4</sub>O<sub>9</sub>, calculated from the equation determined experimentally by Roberts and Walter,\* compared favorably with our data.

Attention has also been focused on measuring partial pressures over UO<sub>2+x</sub>. To date, little quantitative data has been published on total pressures of uranium-bearing species over single-phase UO<sub>2+x</sub>. The oxygen and UO<sub>3</sub> pressures in this region are relevant to the U-Pu-O system we will be studying shortly.

---

\*Roberts, L. E. J., and Walter, A. J., J. Inorg. Nucl. Chem. 22, 222 (1961).



(ii) Total Effusion of Pu-O and U-Pu-O System  
(P. E. Blackburn and R. K. Edwards)

Last Reported: ANL-7606, p. 117 (Aug 1969).

The effusion apparatus, previously used to determine the congruently vaporizing composition of urania as a function of temperature, has been installed in a glovebox so that effusion studies of plutonium-bearing materials may be carried out. The new apparatus, which incorporates a quadrupole mass spectrometer and a vacuum microbalance, allows studies of the Pu-X and U-Pu-X systems where X is either carbon or oxygen. The carbide studies were last reported in ANL-7632, pp. 108-109, Oct 1969, at which time the current status of apparatus development was detailed.

The performance of the effusion apparatus is being tested on nonplutonium (uranium) materials prior to closing up the glovebox, since the testing can be carried out more efficiently in this manner. These tests have shown that the temperature of the effusion cell can be held constant to better than our most sensitive detection limits. Because of this constancy, the effusing system becomes truly invariant in a practical way at the congruently effusing composition; optimum conditions are consequently provided for determining the ionization-efficiency curves needed as part of the calibration information for our instrument. The preliminary curve for the UO species looks very satisfactory, and similar curves for the other species are being determined. Further work in calibration and assessment of the capabilities of the apparatus will precede the planned plutonium studies.

From theoretical studies, it was also established in ANL-7632 that compositions of the condensed phase can probably be determined from a mathematical analysis of the mass-spectrometric ion-current data more accurately than from time-consuming chemical analyses. Continuing theoretical analyses are directed toward simplifying the determination of ionization cross sections needed for converting ion-current observations to partial-pressure values.

b. Preparation of Nuclear Materials (A. A. Jonke)

Last Reported: ANL-7618, p. 118 (Sept 1969).

Studies of the use of a plasma-torch reactor for the conversion of FBR oxide fuel to reactor-grade carbide fuel in high yield have been initiated. The current work is devoted to the conversion of uranium oxide to uranium monocarbide, but the process is expected to be applicable to the production of (U-Pu)C in equipment installed in an alpha-tight enclosure. The method involves making composite particles of uranium oxide and graphite, and reacting the small (~100 mesh) composite particles by passing



them through and cocurrently with the plasma flame of an inductively coupled plasma torch (25 kW) pointed downward. The product, in the form of small, free-flowing spheres of carbide and unreacted oxide and carbon, is collected in a product receiver at the bottom of the reactor.

The preliminary runs made previously indicated that the carbon content of the effluent material was lower than that of the feed, but that the oxygen content of this material was near that of the feed, suggesting that the hot particles emanating from the torch might have reacted with atmospheric oxygen in the reaction chamber. The objectives of the current work are (1) to test the effect of filling the reaction chamber with argon instead of air and (2) to make a number of minor changes in the experimental system to improve operability.

Most of the equipment modifications have been completed, and brief trial runs have been made with argon gas in the reaction chamber. Some operating difficulties were encountered with the electrical supply to the plasma torch, and after the most recent trial run a quartz plate that supports the torch and insulates it from the reaction chamber was found to be cracked. Despite these difficulties, the product from this run (No. 14) had a significantly lower oxygen content than did products of the preliminary runs, indicating that replacement of air in the reaction chamber with argon is helpful.

Analysis of samples of the products from recent runs indicated the presence of  $\alpha$ -UC<sub>2</sub>, which is not a desirable constituent of a reactor fuel. If  $\alpha$ -UC<sub>2</sub> is found in the products of future runs, methods for its elimination will be sought. The plasma-torch equipment is being modified to correct component failures and is being readied for additional runs to establish equipment reliability.

## PUBLICATIONS

Fluidized-Bed Fluorination of  $\text{UO}_2$ - $\text{PuO}_2$ -Fission Product Pellets with  $\text{BrF}_5$  and Fluorine. Part I. The Fluorination of Uranium, Neptunium, and Plutonium

L. J. Anastasia, P. G. Alfredson, and M. J. Steindler

Nucl. Appl. Technol. 7, 425-432 (Nov 1969)

Fluidized-Bed Fluorination of  $\text{UO}_2$ - $\text{PuO}_2$ -Fission Product Pellets with  $\text{BrF}_5$  and Fluorine. Part II. Process Considerations

L. J. Anastasia, P. G. Alfredson, and M. J. Steindler

Nucl. Appl. Technol. 7, 433-442 (Nov 1969)

Neutron Radiography in the Biomedical Field--An Introduction

J. P. Barton

Biomedical Sciences Instrumentation, Proc. 7th Ann. Symp. on Imagery in Medicine, Ann Arbor, Michigan, May 19-22, 1969,

Ed. F. D. Thomas and E. E. Sellers. Instr. Soc. Am., Pittsburgh, 1969, Vol. 6, pp. 83-92.

Neutron Radiography Using Nonreactor Sources

J. P. Barton

Isotopes Radiat. Technol. 6(2), 149-153 (Winter 1968-1969)

A Design for Modular Ultrahigh Vacuum Feedthroughs

P. M. Danielson

Vacuum 19, 412 (Sept 1969) Letter

A Possible Non-destructive Test for Hydrogen Content of Metals

Nils Fernelius

Brit. J. Nondestructive Testing 11(1), 22-23 (March 1969)

Glove Box Facility for Pyrochemical Research and Development Work with  $^{238}\text{Pu}$

Jack Fischer

Proc. 17th Conf. on Remote Systems Technology, Am. Nucl. Soc., San Francisco, November 1969, pp. 63-73

BEMOD, A Code for the Lifetime of Metallic Fuel Elements

V. Z. Jankus

ANL-7586 (July 1969)

Neutron Exposure to Lunar Astronauts

J. Kastner, B. G. Oltman, Y. Feige, and R. Gold

Health Phys. 17, 732 (Nov 1969) Note

#### IV. NUCLEAR SAFETY RESEARCH AND DEVELOPMENT

##### A. LMFBR Safety--Research and Development

##### 1. Reactor Control and Stability

- a. Reactor Stability and Stability Design Criteria for Spatially Dependent Systems (C. Hsu)

Last Reported: ANL-7618, p. 122 (Sept 1969).

(i) Nonlinear Model. Quasilinearization techniques are being applied to the multigroup space-time neutron-diffusion equation. These techniques are being incorporated into the LARK3\* computer code, which solves the linear two-group space-time-dependent neutron-diffusion equation. To obtain a better model for the reactor system, it often is necessary to include nonlinear terms in the neutron-diffusion equation. Inclusion of nonlinear terms requires an iterative solution coupled with smaller spatial and temporal grid values in the finite-difference equations of the system. These changes will increase the computational time substantially.

Using quasilinearization techniques, one obtains an iterative method to solve the nonlinear equations; however, the convergence is quadratic in nature. Thus, computational time is reduced in the iterative calculations. Also, the quasilinear approach allows one to maintain the linear form of the LARK3 code.

- b. Transfer-function Techniques to Measure Large Fast Reactor Stability (L. Habegger)

Last Reported: ANL-7548, pp. 116-117 (Jan 1969).

A study of linear homogeneous LMFBR system stability has been made using the root-loci method.\*\* The objectives of this study were: (1) to determine the linear stability at operating conditions for an LMFBR system currently under study, and (2) to determine the sensitivity of the stability condition (system relative stability) with respect to the variation of system-feedback parameters.

The reactor model considered is a one-energy-group, one-delayed-group model with two temperature feedbacks. The homogeneous parameters used in the analyses are based on the typical design parameters

---

\*Rhyné, W. R., and Lapsley, A. C., Numerical Solution of the Time- and Space-dependent Multigroup Neutron Diffusion Equations (to be published in Nuclear Science and Engineering).

\*\*Hsu, C., and Habegger, L., Root-Loci Approach in the Study of Stability of Linear Homogeneous Space-Time Reactors, IEEE Nuclear Science Symposium, (Oct 1969).

of an LMFBR system. Parametric studies have been made for cases in which all the parameters are fixed except the magnitude and signs of the temperature-feedback coefficients under the condition that the total feedback reactivity is always negative. The results of these studies showed that the system will be asymptotically stable if there is no anomaly, but might become unstable if anomalies, such as partial reduction of coolant flow, occur. However, for this model, no higher-mode oscillation can develop if the fundamental spatial mode is stable.

The study of the relative stability (obtaining the eigenvalues of the various spatial modes) has indicated that the system relative stability is sensitive with respect to the respective sign of the two reactivity feedbacks rather than the combined magnitude. The results have also shown that the dominant eigenvalue does not always correspond to the fundamental spatial shape. It is concluded that it is important to study the detailed spatial feedback model and, in particular, to include cases where the various feedbacks are space-dependent (for example, nonuniform feedback due to fuel-element bowing).

## 2. Coolant Dynamics (J. F. Marchaterre)

### a. Sodium Expulsion (R. M. Singer and R. E. Holtz)

Last Reported: ANL-7632, pp. 129-130 (Oct 1969).

#### (i) Static Expulsion Tests

##### (a) Collection and Analysis of Data from Initial System.

Much data have been obtained on the vapor-growth rate of initially static nonuniformly superheated sodium, including the incipient-boiling superheat and transient pressures associated with vapor growth and collapse. These data are being reduced and analyzed to determine if sufficient information is available from this specific test series.

Some steady-state boiling data are being obtained for comparison with published data. A series of tests designed to examine the theoretical prediction of the heat-flux effect on the incipient-boiling superheat are being planned.

#### (ii) Forced-convection Expulsion Tests

##### (a) Preparation of Transient Test Loop.

Work is continuing on the installation of general loop instrumentation. The test section has been fabricated, and is being instrumented with pressure taps, thermocouples, voltage taps, and flowmeter connectors. Initial circulation of sodium in the loop is expected to commence within 6-8 weeks; loop debugging will follow.

### 3. Fuel Meltdown Studies with TREAT

#### a. Experimental Support (C. E. Dickerman)

Last Reported: ANL-7632, p. 137 (Oct 1969).

(i) Safety Aspects of the Elevated Temperature Behavior of DC-200 Silicone Cooling Oil Used with the Mark-II TREAT Sodium Loop. DC-200 dimethylpolysiloxane (silicone) oil is used as an auxiliary coolant for the Mark-II TREAT sodium loop, to cool the Annular Linear Induction Pump (ALIP) and the loop freeze plugs. As part of the loop development, an analysis was made of the chemical stability of the silicone oil under "operating accident" conditions of (1) rupture of silicone lines with dispersal of silicone on hot loop parts, and (2) silicone flow stoppage in the ALIP. After review of the available chemical data, it was concluded that the oil presented no hazards of overpressure or overheating of loop parts due to silicone decomposition and combustion for the following reasons:

(1) The decomposition of the oil is endothermic, requiring a heat source to sustain it.

(2) External heat must also be supplied to sustain combustion of these compounds or their decomposition products.

(3) The surface of the loop can, at a nominal 200°C, represent the coldest portion of the system, and as such affords a condensation surface for the decomposition or distillation products of the higher-temperature oil. Consequently, this condensation reduces the pressure of the loop system.

It was concluded under these assumptions that the pressure from the decomposition of the coolant oil would be less than 15 psi.

These conclusions were supported by results of a test performed during the testing period prior to the high-pressure proof test of the prototype loop (see Progress Report for January 1969, ANL-7548, pp. 124-127). In that test, the oil was heated to 950°F in the ALIP shell by valving off flow to the ALIP from the unit for cooling the silicone. During the time the oil was stagnant, heat was supplied for the loop and for the ALIP operating at 1.5 kW. No damaging overpressures resulted, but an epoxy seal (not used on pumps other than the prototype) developed a leak which allowed silicone to spill on the hot loop. While the oil was observed to smoke, no ignition, explosion, or significant damage was found.

During the safety review of the Checkout-1 Mark-II loop experiment, the experimenters were requested to supply additional information on silicone behavior under these conditions. Accordingly, a simple but quantitative survey experiment has been performed on pressure

generation of silicone oil in a closed system. A given quantity of silicone was heated in a closed copper tube with argon cover gas above the silicone surface. The nominal room-temperature volume of the silicone for each run was 36.9 cc, and the nominal room-temperature value of argon was 73.9 cc. The silicone occupied a cylindrical volume about 15 cm long, with a thermocouple well extending down from the top surface half way (i.e., to 8 cm from the bottom of the cylinder). In order to effect good contact between the thermocouple and well, some silicone oil was added to the well. The thermocouple was always wet after removal from its well after each run, even though some smoking of the oil in the well was noted at temperatures above 650-750°F. Pressures were measured as a function of oil temperature during each run. The pressure of the compressed, heated cover gas was computed and subtracted from the total in order to obtain the partial pressure of the hot silicone. Pressures were measured after post-test cooling. After the last run (maximum temperature of 883°F) the post-test pressures were measured to be in excess of the original argon pressure of one atm by only 1.2, 1.0, and 0.6 psi at cooling times of 1.5, 2, and 18 hr, respectively.

These tests showed that the pressure due to the vapor or decomposition products from the ALIP coolant was about 25 psi at a temperature below 800 to 880°F. Consequently, the total pressure which could be attributed to the vapor and decomposition products from the pump-cooling oil was moderate for the temperatures studied.

(ii) Shipping Cask. The vendor shop drawings of the TREAT Mark-II-loop shipping cask were reviewed, and comments were forwarded to the vendor. The revisions of the drawings required to comply with the comments are in progress and are expected to be completed during the week of December 1, 1969. The design analysis of the cask is being reviewed and updated to reflect minor design changes. This review is expected to be completed during the next reporting period, so that the entire package (drawings and analysis) can be forwarded to the AEC for approval.

Shop work on modifications to the special form containers necessary to comply with the regulations has been completed. The special form containers now can be used as DOT Spec. 7A containers for shipments of Type A quantities of nonfissile radioactive material, or as containers for encapsulation of fissile or nonfissile material for shipment as "special form" material.

(iii) Proof-test of the Mark-IIB-3 Integral Sodium TREAT Loop. Prior to experimental use in the meltdown studies of fast reactor fuels in the TREAT facility, each of the Mark-II integral sodium loops is subjected to a proof-test, as prescribed by the ASME code.\* For this test, the loop

---

\*Sect. III, Nuclear Pressure Vessels, Boiler and Pressure Vessel Code.



must be fully outfitted with external heaters, ALIP sodium driver, cooling lines, insulation, and sensor circuits, to permit pressure testing of the loop to 125% of its rated pressure, while operational at the device's rated temperature.

On November 8, 1969, the second Mark-II integral sodium loop (the "B-3") was proof-tested to 5000 psig (340 atm) while at 1000°F (538°C). The test was pneumatic, using high-purity argon, since the required normal fill of 1300 cc of sodium results in a gas-filled volume of about 600 cc. The contained sodium is pumped through the loop proper at a low flow rate, sufficient to ensure the establishment and maintenance of the distribution of temperature to be realized during experimental operation of the facility.

For the test, the Mark-IIB-3 loop was suspended from the jib-crane outside the west door of Cell 6, the high-bay of Building 316, inside a split hinged can with the bottom of the hinged test can resting on the ground, against the loading dock. All control, power, cooling, and pressurization equipment was located just inside the partially raised loading door.

The sequence of the test was essentially uneventful. During the heatup phase of the test, as the loop temperatures exceeded 500°F, wisps of white vapor or "smoke" began to appear above the top plate and around the unsealed through-connector hole for the test-section thermocouples, and continued to be emitted as the loop neared and attained test temperatures. This vapor emission was noted to have the color and magnitude typical of normal bake-out of the organic binders and adhesives present in the glass-tape sections used to hold leads and lines in place for permanent anchoring. A small leak of silicone coolant could also have contributed to the smoke. After the proof test, the can was opened, and residual silicone fluid was found on some of the Swagelock connectors, with some visible deposits of thin, finely divided siliceous powder on the interior walls of the can. The fluid leak was traced to one of the hose connections outside of the loop can, above the top plate; all connections within the loop can were tight. No damage of any kind was found, in good agreement with the developmental test results from the prototype loop.

During the pressurization of the loop, the argon pressure was raised from the full-bottle value by means of the DYNAIR gas-pressure intensifier. The full pressure of a bottle of argon gas was applied to the dump tank, to prevent pressuring the burst disc when the test pressure exceeded the disc-rupture rating. The differential pressure across the burst disc between the loop and the dump tank was held to a maximum of 3000 psig.



Following the test, extensive examination of the loop revealed no evidence of any distortion or deformation. Throughout the proof-test operation of the loop, all control and instrument components functioned properly.

(iv) Pressure Transducers for the Mark-II Integral Sodium TREAT Loops. Very little developmental work has been done on transient-pressure instrumentation for high-temperature liquid-metal systems, either by the manufacturers of pressure transducers or by research organizations. Such instrumentation as exists for liquid-metal-filled systems has required adaptation of conventional, commercially available transducers developed for steam, process liquids, or rocketry; for remote-reading, slow-response demands, this has presented no problem, even in the extreme environments of operating nuclear reactors. However, the requirement of transient instrumentation for close-coupling of the sensors to liquid-metal-filled facilities at elevated temperatures and in high-level radiation fields renders the adaptations extremely difficult.

At ANL, some success has been realized in the application of readily available pressure transducers to sodium loops,\* with the result that useful experimental pressure data has been obtained from the meltdown studies of fast reactor fuels in the TREAT facility.

At the time of the preparation of the Mark-I Integral Sodium TREAT loops, the pressure transducers considered to offer the best overall characteristics for adaptation to the sodium-filled flow system were unbonded strain-gage bridge sensors. There were several competitive transducers, essentially of the same type, and differing only in the method of strain-gage support within the transducer body.\* The 1/2- to 5/8-in.-diameter transducers selected were attached to the system by means of a tubular MaK-filled stand-off technique, to provide physical isolation of the sensor diaphragm, and a thermal isolation of the transducer as a whole from the high-temperature environment of the loop.

The sensors used for the Mark-I loop had been successfully used in steady-state nuclear radiation fields at LASL. They consist of unbonded strain wires, wound on insulating posts between opposing double star-springs which are mechanically coupled to the actuating diaphragm, as the active arms of a resistance bridge, with the inactive arms made of the same strain wire and wound on fixed supports anchored to the transducer-housing base.

During meltdown experiments in the TREAT facility using the Mark-I loops, these transducers furnished usable pressure-pulse data, but exhibited spurious electrical imbalance as a result of the extreme

---

\*Robinson, L. E., and Purviance, R. T., Pressure Transducers for TREAT Sodium Loops, ANL-7107 (June 1969).

radiation levels, as high as 40% of full scale. Pressure pulses having rise-times of 1 to 5 msec, and amplitudes to greater than 200% full range (with 150-psig sensors) were recorded. Permanent deformations of the transducer diaphragm, which resulted in post-transient unbalance equivalent to negative pressures of 60 psig, were experienced, without destroying the function of the transducer.

The high radiation sensitivity of these unbonded strain-gage transducers resulting in large, smooth, relatively consistent spurious output, with well-defined characteristic shapes\* prompted a continuing search for a pressure transducer better suited to the environment of high-power-density sodium-cooled reactors.

Thus, for the Mark-II integral sodium loop, a variable-impedance transducer, developed for blast instrumentation, seemed to offer the desired properties, including

- |                              |                             |
|------------------------------|-----------------------------|
| 1) low radiation sensitivity | (~3% at $10^{16}$ nvt)      |
| 2) high-frequency response   | (>40 kc, natural frequency) |
| 3) high-temperature rating   | (600°F, operational)        |
| 4) high electrical output    | (~40 mv FS)                 |
| 5) sodium compatibility      | (no mechanical coupling)    |

The variable-impedance model chosen was a standard unit, modified with the inlet nozzle jacketed with a copper radiator, for use with the NaK-filled loop stand-off.

Calibrations of the transducers with NaK eddy-current coupling, and subsequent bench tests, indicated the devices to perform as specified and predicted. However, on the actual application of the sensors to the Mark-II loops during outfitting, defects were found to have developed in 62% of the transducers purchased. The sensing-coil leads were broken at the point of connection of the coil wire to the lead wire. This connection has been silver-soldered, the flux not removed, and breakage occurred as a result of flux corrosion, enhanced by mechanical stresses introduced by assembly techniques.

In addition to the coil-lead breakage, the 0.062-in.-diameter, MgO-insulated, stainless steel-sheathed Nichrome wire used as the coaxial cable connection to the pressure transducer proved to be extremely difficult to seal against moisture, under the best of conditions. Normal handling of the cable after sealing effectively destroyed the integrity of the seal. The 1-Mc excitation of the transducer, tuned for phase-shift detection of minute changes of impedance stemming from variation in the magnetic-coupling feedback between diaphragm and sensing coil, was found in practical use to

---

\*Each transducer had to be "calibrated" for its radiation response separately.

be incredibly sensitive to even picofarad changes in circuit capacitance, and to drift erratically in a static setup. Large, erratic, zero shifts and extreme sensitivity to temperature gradients were encountered routinely with all units. Other problems of the variable-impedance transducer included additional deterioration in storage, sensitivity to necessary shipping shocks, and frequent failures of the oscillator-demodulator excitation-output module.

During a preliminary transducer test in TREAT, a variable-impedance pressure transducer exhibited ~30% full-scale radiation spurious signal.

Following the problems with the variable-impedance pressure transducer, a used, obsolete transducer was obtained; this unit was originally designed to resist radiation effects. It is an unbonded strain-gage bridge transducer, similar to the ones used earlier on the Mark-I loops, but fabricated wholly with radiation-resistant inorganic materials.

For the two checkout tests with the Prototype Mark-II integral loop\* the variable-impedance transducer was used at the test-section outlet, and the obsolete strain-gage transducer was used at the test section inlet. The latter sensor showed ~10% full-scale radiation sensitivity (improvement by a factor of 4 over the units used on the Mark-I loop, for similar exposure). This strain-gage sensor has proven to be uncomplicated in use, with low sensitivity to thermal gradients.

Since the inlet transducer on the prototype loop had been replaced in the manufacturer's line by a more "advanced" device, one of the "improved" transducers was subjected to a TREAT power transient. Although this sensor (according to manufacturer's data) had surpassed, in all respects, the earlier model in performance in a number of power-generating, steady-state nuclear reactors, the new device with its thin-film strain bridge responded to the short-time, very high radiation of TREAT with a wildly erratic electrical output signal of extreme amplitudes.

Apparently, the extreme burst radiation of the transient caused the thin ceramic substrate of the thin-film strain element to act as a semiconductor, producing successive avalanches of charge between input and output.

Arrangements have been made for procurement of 10 transducers of the same model used at the inlet of the Prototype loop. Unlike the transducers used on the Mark-I loop (or the variable-impedance transducers), these do not always require auxiliary cooling. Auxiliary cooling

---

\*See Reactor Development Progress Reports for July, September, and October, 1969 ANL-7595, p. 116; ANL-7618, p. 128; and ANL-7632, pp. 131-134.

had been required routinely on both Mark-I and Mark-II loops to eliminate electrical unbalance due to temperature gradients in the transducer. The inlet transducer on the prototype loop was run without cooling.

b. TREAT Operations (J. F. Boland)

(i) Reactor Operations. The final transient tests were run on ORNL experiments TR-1 and TR-2 containing stainless steel-clad sphere-pac and pelleted  $\text{PuO}_2\text{-UO}_2$  fuel. Post-transient neutron radiographs were made of the experimental capsules, and the capsules were shipped to ORNL for disassembly.

A group of experimental capsules was neutron radiographed for INC.

The reactor has been shut down since Nov. 4 to permit TREAT personnel to assist the EBR-II Project during their shutdown. Concurrently, modifications are being made to the TREAT instrument room for installation of equipment for the automatic control system, and some of the existing TREAT control-rod-drive mechanisms are being overhauled.

(ii) Development of Automatic Power-level-control System. The contractor has finally received acceptable cylinders for the hydraulic actuators, and delivery of the hydraulic control-rod-drive system is scheduled for mid-January.

4. Violent Boiling (R. O. Ivins)

a. Particle Heat-transfer Studies (D. R. Armstrong)

Last Reported: ANL-7595, p. 120 (July 1969).

The first draft of the work plan for this work has been completed.

b. Violent Boiling with Molten Fuel and Sodium (D. R. Armstrong)

(i) Pressure-generation Experiments by Dropping Molten Material into Coolant

Last Reported: ANL-7606, pp. 132-133 (Aug 1969).

An operable induction-coil design has been developed for use in melting  $\text{UO}_2$  for studies of the sodium- $\text{UO}_2$  interaction. Several trial experiments used a tungsten crucible equipped with a plug valve at the bottom. In these tests, the crucible was filled with 40 gm of  $\text{UO}_2$  and heated to  $\sim 200^\circ\text{C}$  above the melting point of  $\text{UO}_2$ . In the most recent

experiment the plug could not be pulled from the crucible to release the liquid  $\text{UO}_2$ . This malfunction might be due either to sintering together of the valve components at high temperatures, or to a high viscosity of liquid  $\text{UO}_2$ . The crucible will be sectioned and examined to determine which effect predominated.

The drop-experiment apparatus is being removed from the furnace chamber in preparation for the installation of equipment to be used for injecting liquid sodium into  $\text{UO}_2$ . A second work station for the 100-kW induction generator has been installed in a helium-atmosphere module Cenham glovebox, and a  $\text{UO}_2$  drop experiment is being set up in this glovebox. An open-top tungsten crucible will be heated inductively, then rotated  $180^\circ$ , to drop the contents into a pool of sodium.

## 5. Post-accident Heat Removal (R. O. Ivins)

### a. Engineering Analysis (J. C. Hesson)

Last Reported: ANL-7618, p. 135 (Sept 1969).

#### (i) Thermally Stable Fuel-debris Configurations in Sodium.

Analyses of heat removal from collapsed or molten cores under liquid sodium are continuing, and include studies of sizes and geometries of "thermally stable" configurations, i.e., configurations that are in thermal equilibrium with surroundings and do not erupt because of internal boiling or undergo significant geometry changes.

In the cases of spheres, cylinders, and slabs where there is no internal convection due to circulation (heat transfer by conduction only), the maximum diameters or thickness of these shapes to avoid internal boiling are:

$$\text{Sphere } d = \sqrt{\frac{24 k(T_b - T_s)}{q}};$$

$$\text{Cylinder } d = \sqrt{\frac{16 k(T_b - T_s)}{q}};$$

$$\text{Slab } d = \sqrt{\frac{8 k(T_b - T_s)}{q}};$$

where  $d$  = diameter or thickness (cm),  $k$  = thermal conductivity of fuel material (assumed equal for liquid and solid) (cal/sec-cm- $^\circ\text{C}$ ),  $T_b$  = boiling temperature ( $^\circ\text{C}$ ),  $T_s$  = surface temperature ( $^\circ\text{C}$ ), and  $q$  = decay heat rate (cal/sec-cm $^3$ ). Computed values of  $d$  as a function of  $q$  for  $k = 0.005$  cal/sec-cm- $^\circ\text{C}$ ,  $T_b = 3179^\circ\text{C}$ , and  $T_s = 900^\circ\text{C}$  are shown in Fig. IV.A.1.

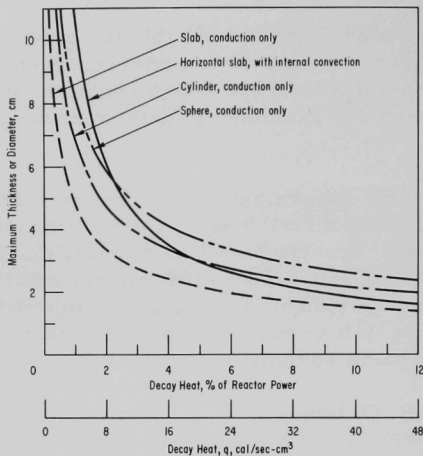


Fig. IV.A.1

Calculated Maximum Thickness or Diameter of a Slab, Cylinder, or Sphere for No Fuel Boiling, where  $T_s = 900^\circ\text{C}$ ,  $T_b = 3179^\circ\text{C}$ , and  $k = 0.005 \text{ cal/sec-cm}^\circ\text{C}$

In the case of a horizontal slab, calculations of the effect due to internal circulation of the molten fuel material were made. These calculations used the following values for molten fuel material:  $T_f$  = freezing temperature,  $2842^\circ\text{C}$ ,  $\rho$  = density,  $8.7 \text{ gm/cm}^3$ ,  $C_p$  = specific heat,  $0.114 \text{ cal/gm-}^\circ\text{C}$ ,  $\mu$  = viscosity,  $0.01 \text{ poise}$ , and  $\beta$  = coefficient of thermal expansion,  $10^{-4} \text{ cm}^3/\text{cm}^3\text{-}^\circ\text{C}$ .

Calculations were made by using a modification of correlations for heat transfer by convection between horizontal plates.

Values of the calculated thickness  $d$  for the slab are shown in Fig. IV.A.1 and illustrate the effects of convection in the horizontal slab. Note that the effects become more pronounced at lower rates of decay-heat generation.

Analytical work is being continued.

## B. Engineered Safety Features--Safety Features Technology--Research and Development--Containment

### 1. Hydrodynamic Response to High-Energy Excursion (Y. W. Chang)

Last Reported: ANL-7618, pp. 135-138 (Sept 1969).

#### a. Automatic Rezoning of Code to Extend Excursion Treatment into Sodium-momentum Domain

Not previously reported.

The REXCO-H Code works well in the shock-wave domain and in the early part of the liquid-momentum domain. However, as meshes



become severely distorted, the computer results become inaccurate. Re-zoning of the Lagrangian meshes was considered a possible remedy for these difficulties. It was decided to develop a rezoning method and a computer code so that the rezoning can be accomplished automatically by the computer.

The rezoning code will be written entirely independently of the hydrodynamics code. The hydrodynamics code would be run with the pure Lagrangian code; when the mesh begins to get somewhat distorted, it would be stopped, and the rezoning code would take over and smooth out the mesh; there would be no time change during the rezoning operation. The smoothed mesh would be passed back to the hydrodynamics code for more calculations. By this process of infrequent use of the rezoning, it is hoped that the mesh distortions can be alleviated sufficiently to permit the problem to run satisfactorily.

There are disadvantages in the rezoning process. For example, after rezoning, the original outlines of the interfaces are destroyed, and the displacements of the Lagrangian grids are no longer the actual movements of the particles. Moreover, the transport of material from one zone to another as a result of rezoning often creates difficulties in the formulation of the equation of state if two zones are made of two different materials. After careful study of the patterns of zone deformation, it was found that the zones at the interfaces of two media having different physical properties were usually deformed first. Thus, if the distortions at such interfaces can be eliminated or slowed down, the hydrodynamics computation can be extended to a much longer time without the use of the rezoning process. Therefore, as an intermediate step to extend the computation time, two methods have been developed: (1) a single-line-vessel method, which permits a reactor vessel to be represented by a single line and which permits sodium to slide freely along the vessel wall and thus eliminate zone distortions, and (2) a nearest-neighbor-hydrodynamics method, which permits the pressure gradients to be calculated from the nearest neighbor mesh points and thus to reduce the inaccuracy of the finite-difference expression introduced from zone distortions. Both methods have been programmed in FORTRAN and are being studied.

#### b. Selection of Temperature-dependent Equation of State

Not previously reported.

The objective is to select a suitable equation of state for reactor materials that not only relates the thermodynamic variables [pressure, temperature (or energy), and volume], but also contains temperature-dependent parameters. A study of available types of equations of state indicates that, for pressures below several hundreds of kilobars, the most suitable equation of state for steel and sodium is the Murnaghan\* equation of state:

\*Murnaghan, F. D., The Compressibility of Media under Extreme Pressures, Proc. Nat. Acad. Sci., 30, 244-247 (1944).



$$P = \frac{B_0}{B'_0} \left[ \left( \frac{V_0}{V} \right)^{B'_0} - 1 \right], \quad (1)$$

where  $P$  is the pressure,  $V$  and  $V_0$  are the deformed and undeformed volumes, respectively, and  $B_0$  and  $B'_0$  are the bulk modulus and its pressure derivative, respectively. This equation was first derived by Murnaghan in a different form. In Murnaghan's original derivation,  $B_0$  and  $B'_0$  are two constants corresponding to a fixed temperature, usually room temperature. Here, this equation has been generalized to arbitrary temperature by assuming  $B_0$  and  $B'_0$  to be temperature-dependent parameters.

The advantage of using this type of equation of state is that the  $P$ - $V$  curve can be determined easily from  $B_0$  and  $B'_0$ , which are generally available. Also, the temperature dependence of  $B'_0$  is very small. Where the temperature dependence of  $B'_0$  is not known,  $B'_0$  can be taken to be constant and estimated from the Mie-Gruneisen coefficient  $\gamma$ . Thus,  $P$ - $V$  curves at various temperatures can always be evaluated if the values of  $B_0$  and  $\gamma$  are known. The analytic expression of  $B_0$  for Type 304 stainless steel is

$$B_0 = 507.773192 + 4.29589426T - 5.53011636 \times 10^{-3}T^2 + 1.72803701 \times 10^{-6}T^3 \quad \text{for } 366 < T < 1530, \quad (2)$$

and for liquid sodium is

$$B_0 = 74.7680242 - 5.0457584 \times 10^{-2}T + 9.70732025 \times 10^{-6}T^2 \quad \text{for } 372 < T < 1650, \quad (3)$$

where  $B_0$  is in kilobars and  $T$  is in  $^{\circ}\text{K}$ . The values\* of  $B_0$  are least-squares fitted by use of the computer. The temperature dependence of  $B'_0$  for Type 304 stainless steel and liquid sodium is not known. For the present investigation, they are taken to be 5.0 and 3.59, respectively. Figure IV.B.1 shows two  $P$ - $V$  curves for sodium, one at  $372^{\circ}\text{K}$  and the other at  $1650^{\circ}\text{K}$ , plotted from Eq. (1) using values of  $B_0$  and  $B'_0$  as given by Eq. (3). At high temperature, sodium becomes extremely compressible.

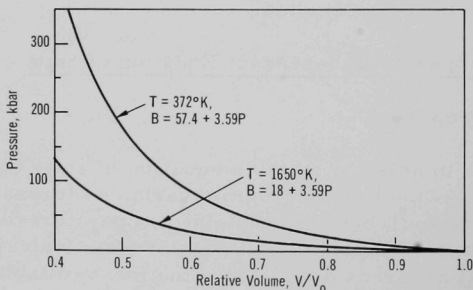


Fig. IV.B.1  
P-V Curves for Sodium at  
 $T = 372$  and  $1650^{\circ}\text{K}$

\*Garofala, F., Temperature Dependence of the Elastic Moduli of Several Stainless Steels, Proc. ASTM, 60, 738 (1960); Golden, G. H., and Tokar, J. V., Thermophysical Properties of Sodium, ANL-7323, (Aug 1967) pp. 95-100.

## PUBLICATIONS

The Dynamic Plastic Response of a Tube to an Impulsive Ring Load of  
Arbitrary Pulse Shape

Carl K. Youngdahl

ANL-7562 (April 1969)

Pressure Transducers for TREAT Sodium Loops

L. E. Robinson and R. T. Purviance

ANL-7107 (June 1969)



ARGONNE NATIONAL LAB WEST



3 4444 00024357 6

